ECOLE DES PONTS PARISTECH

ÉCOLE DOCTORALE : SCIENCES, INGÉNIERIE ET ENVIRONNEMENT

Thèse de doctorat

Sciences et Techniques de l'environnement

Najwa SHARAF

TÉLÉDÉTECTION ET MODÉLISATION POUR LA SURVEILLANCE
ET LA COMPRÉHENSION DE LA DYNAMIQUE DES CYANOBACTERIES
DANS LES LACS DE BARRAGE
APPLICATION A LA RETENUE DE KARAOUN (LIBAN)

Thèse dirigée par Brigitte VINÇON-LEITE
Co-dirigée par Kamal SLIM

Soutenue le 22 Avril 2021

Jury :

Mme Brigitte VINÇON-LEITE	Directrice de thèse	Directrice de recherche, ENPC
M. Kamal SLIM	Co-Directeur de thèse	Professeur, CNRS-L
Mme Claudia GIARDINO	Rapportrice	Directrice de recherche, CNR-IREA
Mme Clelia MARTI	Rapportrice	Directrice de recherche, Université de Curtin
Mme Céline CASENAVE	Examinatrice	Chargée de recherche, INRAE
Mme Alexandrine PANNARD	Examinatrice	Maitre de conférences, Université de Rennes1
M. Ali FADEL	Encadrant	Chargé de recherche, CNRS-L
M. Bruno LEMAIRE	Encadrant	IPEF, AgroParisTech
M. Pierre-Alain Danis	Invité	Ingénieur de recherche, OFB

ECOLE DES PONTS PARISTECH

DOCTORAL SCHOOL: SCIENCES, ENGINEERING AND ENVIRONMENT

Doctoral thesis

Sciences and Techniques of Environment

Najwa SHARAF

USING REMOTE SENSING AND MODELING TO MONITOR AND UNDERSTAND
HARMFUL ALGAL BLOOMS
APPLICATION TO KARAOUN RESERVOIR (LEBANON)

Thesis directed by Brigitte VINÇON-LEITE
Co-directed by Kamal SLIM

Defended on the 22th of April 2021

Jury:

Mrs Brigitte VINÇON-LEITE	Thesis Director	Research Director, ENPC
Mr Kamal SLIM	Thesis Co-Director	Professor, CNRS-L
Mrs Claudia GIARDINO	Reviewer	Research Director, CNR-IREA
Mrs Clelia MARTI	Reviewer	Research Director, Curtin University
Mrs Céline CASENAVE	Examiner	Researcher, INRAE
Mrs Alexandrine PANNARD	Examiner	Lecturer, Rennes1 University
Mr Ali FADEL	Supervisor	Researcher, CNRS-L
Mr Bruno LEMAIRE	Supervisor	Lecturer, AgroParisTech
Mr Pierre-Alain Danis	Invited Member	Researcher Engineer, OFB

Résumé

Les retenues sont des ressources d'eau stratégiques en particulier pour la production d'eau potable et d'énergie électrique. Un suivi régulier de la qualité de l'eau des retenues dans le contexte actuel du changement climatique, de l'eutrophisation et d'une demande en eau plus élevée est nécessaire pour optimiser les stratégies de gestion. Les progrès dans le domaine de la télédétection permettent l'acquisition de données sur une échelle synoptique et la réalisation d'études rétrospectives. Les données satellitaires sont complémentaires des mesures *in situ* mais ne portent que sur une profondeur limitée de la colonne d'eau. En revanche, les modèles numériques tridimensionnels (3D) qui intègrent les processus physiques, chimiques et biologiques peuvent simuler le fonctionnement de l'écosystème sur des périodes continues et sur toute la colonne d'eau.

Dans ce contexte, cette thèse s'intéresse à l'utilisation combinée des données fournies par des campagnes de mesures *in situ*, de la télédétection et de la modélisation 3D en utilisant le modèle Delft3D. L'objectif principal de ce travail est de proposer une approche combinée pour la surveillance de la qualité de l'eau des retenues de taille moyenne (~ 14 km^2).

Le site d'étude est la retenue de Karaoun au Liban (climat semi-aride, surface 12 km^2, capacité 110 hm^3). Cette retenue, actuellement utilisée pour la production d'énergie électrique, pourrait dans le futur servir pour la production d'eau potable. Eutrophe, elle connait des épisodes récurrents de proliférations de cyanobactéries toxiques. L'approche méthodologique suivante a été adoptée:

i) Les mesures *in situ* ont été collectées régulièrement du printemps à l'automne pour le calage et la validation des algorithmes de télédétection et des paramètres du modèle.

ii) Afin de caler et valider les algorithmes de télédétection, une correction atmosphérique des images satellitaires de Landsat 8 et Sentinel-2 a été appliquée en utilisant respectivement un algorithme à bande unique et le code 6SV.

    a. Quatre algorithmes de la littérature pour estimer la température de surface ont été validés en utilisant des données thermiques de Landsat 8.

    b. Un algorithme de Sentinel-2 déjà calé et validé a été utilisé pour estimer les concentrations en chlorophylle-a.

    c. Un algorithme empirique a été calé et validé afin d'estimer la transparence à partir des données de Sentinel-2.

iii) Afin de mener une analyse rétrospective de la température de surface, l'algorithme validé a été appliqué sur une série d'images Landsat de 1984 à 2018.

iv) Afin de reproduire les processus hydrodynamiques et écologiques, en incluant la biomasse des cyanobactéries dans le temps et l'espace, le modèle Delft3D a été configuré, calé et validé pour l'été et l'automne. La distribution spatiale de température de surface et des concentrations de chlorophylle-a provenant du satellite et du modèle a été investiguée.

Les résultats de ce travail ont montré que, parmi les quatre algorithmes testés, l'algorithme qui dépend du contenu atmosphérique en vapeur d'eau et de l'émissivité de l'eau a abouti aux meilleures estimations de la température de surface. En utilisant cet algorithme validé, l'analyse

rétrospective de la température de surface, de 1984 à 2018, n'a pas révélé de tendance de réchauffement au site d'étude. Le modèle Delft3D a bien représenté l'évolution de la fluctuation de niveau d'eau, la distribution temporelle et verticale de la température et la biomasse du phytoplancton. Les données satellitaires et les simulations du modèle ont montré une faible hétérogénéité spatiale pour la température de surface (< 2 °C) et considérable pour les concentrations en chlorophylle-a (~ 50 mg.m^{-3}). La comparaison des résultats du modèle avec les données satellitaires a indiqué, en général, une bonne corrélation dans le temps et l'espace.

Le modèle Delft3D a montré une bonne capacité à simuler la structure thermique et la biomasse du phytoplancton dans une retenue. Ce travail met en évidence la valeur des images satellitaires comme source de données complémentaires aux mesures *in situ*, permettant la validation des modèles et la surveillance des retenues. L'approche proposée est transférable à d'autres écosystèmes lacustres et très adaptée pour les écosystèmes où un suivi régulier de la qualité de l'eau n'est pas possible.

Mots clés : *Retenue, Télédétection, Modélisation, Hydrodynamique, Cyanobactéries*

Abstract

Reservoirs are strategic water resources in particular for drinking water and hydropower production. Nevertheless, their physical and biogeochemical processes have been long influenced by anthropogenic pressures. A complete and regular monitoring of reservoir water quality in the context of current climate change, eutrophication and higher water demand, has become crucial for optimal management strategies. Recent progress in the satellite remote sensing field made it possible to enhance data acquisition on a synoptic scale and to perform retrospective studies. Satellite data can complement measurements however over a limited depth of the water column. In addition, three-dimensional (3D) numerical models which integrate physical, chemical and biological processes can fill temporal gaps and extend the information into the vertical domain.

In this context, this PhD thesis focuses on the combined use of techniques and data derived from field monitoring, satellite remote sensing and 3D modeling using Delft3D. The overreaching objective of this work is to propose a combined approach for surveying the water quality of medium-sized reservoirs (~ 14 km^2).

The study site is Karaoun Reservoir, Lebanon (semi-arid climate, surface 12 km^2, capacity 110 hm^3). It mainly serves for hydropower however with possibly a future drinking water production. It is eutrophic and has been experiencing regular events of toxic cyanobacterial blooms. The following methodological approach was adopted:

v) *In situ* measurements were regularly collected from spring to fall for the calibration and the validation of remote sensing algorithms and of the model.

vi) In order to calibrate and validate remote sensing algorithms, Landsat 8 and Sentinel-2 imagery were atmospherically corrected using a single-channel algorithm and the 6SV code respectively.

  a. Four algorithms from literature for deriving surface temperature were validated using Landsat 8 thermal data.

  b. A previously calibrated and validated Sentinel-2 algorithm was applied to retrieve chlorophyll-a concentrations.

  c. An empirical algorithm was calibrated and validated in order to retrieve transparency from Sentinel-2 data.

vii) In order to conduct a retrospective analysis of surface temperature, the validated single channel algorithm was applied to a series of Landsat images from 1984 to 2018.

viii) In order to reproduce the hydrodynamics and ecological processes, including cyanobacterial biomass in space and time, the Delft3D model was configured, calibrated and validated for summer and fall. The spatial distribution of surface temperature and chlorophyll-a concentrations from the satellite and the model were investigated.

The results of this study revealed that, among the four tested algorithms, the single channel algorithm dependent on atmospheric water vapor content and lake water emissivity yielded the best estimations of surface temperature. Using this validated algorithm, the retrospective analysis

of surface temperature did not reveal any warming trend over the 1984-2018 period at the study site. Compared to *in situ* profiles, the Delft3D model represented well the evolution of the water level fluctuations, and the time and vertical distribution of temperature and phytoplankton biomass. Satellite data and model simulations showed minor spatial heterogeneities of surface temperature (< 2 °C) and considerable ones for chlorophyll-a concentrations (~ 50 mg.m^{-3}). Their comparison revealed an overall good correlation in space and time.

This work showed the good performance of the Delft3D model for simulating the thermal structure and phytoplankton biomass in a reservoir. It highlighted the value of satellite images as complementary to *in situ* measurements for validating 3D models and for the survey of reservoirs. The proposed approach is transferrable to other freshwater ecosystems and is particularly beneficial for poorly monitored ecosystems.

Keywords: *Reservoir, remote sensing, Modeling, Hydrodynamics, Cyanobacteria*

Acknowledgements

Table of contents

List of Figures

13

List of Tables

General Introduction

Lakes and reservoirs provide a diversity of ecosystem services. Yet, their water quality and hence suitability to sustain various uses have long been influenced by anthropogenic pressures impacting their chemical, physical and biological processes.

In the last several decades, cultural eutrophication, wherein the rate of nutrient inputs is accelerated due to human activities, has become the most prevailing problem facing freshwater ecosystems (Downing, 2014; Le Moal et al., 2019). In particular, the accompanying development of harmful algal blooms especially blooms of nuisance cyanobacteria genera, an event that has been rising in freshwater ecosystems worldwide leading to a bad ecological status (Huisman et al., 2018).

Cyanobacterial blooms are a major problem in lakes and reservoirs negatively impacting water quality. Cyanobacteria possess unique traits allowing them to dominate over other phytoplankton groups and are notoriously known for producing toxic compounds (toxins or cyanotoxins). Toxins produced by cyanobacteria can threaten human health through waters used for agricultural, recreational and drinking water purposes. The associated human risks include neurological disorders, intestinal problems, fevers and skin irritations (He et al., 2016).

In recognition of these risks, the World Health Organization (WHO) has established advisory guidance levels for cyanobacterial toxins in recreational waters. These guidelines provide an estimate of the risk of adverse health outcomes in case of exposure (Bartram & Chorus, 1999).

Owing to these problems and in order to reach a good ecological status it is important to understand the ecological and hydrodynamic functioning of lakes and reservoirs in response to environmental factors. Mainly, the dynamics of phytoplankton including cyanobacteria, commonly represented by the concentration of chlorophyll-a (*Chl-a*) which in turn is used as an indicator of water quality. On the other hand, in the light of climate change, the rise in temperature has gained attention for its contributive impact over cyanobacterial blooms expansion (Moss et al., 2011; Paerl & Huisman, 2008).

Phytoplankton communities are highly diverse in freshwater ecosystems. They exhibit temporal and spatial horizontal and vertical heterogeneities along the water column (Hunter et al., 2008). These distributions are influenced by physical (light availability, hydrodynamics and wind-driven mechanisms) and biological (grazing by zooplankton, competition between species) processes (Pinardi et al., 2015). Moreover, the magnitude, frequency, and duration of Harmful Algal Blooms (HABs) in inland waters are poorly documented (Brooks et al., 2016).

In this context, there is a need for understanding ecosystem ecological processes, in particular the impact of environmental variables on phytoplankton dynamics with an emphasize on cyanobacteria. This requires a complete and continuous monitoring of lake and reservoir water quality. Monitoring water quality parameters can be achieved by conventional *in situ* monitoring methods, satellite remote sensing techniques.

Conventional water quality monitoring methods depending on *in situ* sampling and laboratory measurements are accurate however they present important drawbacks. These methods do not take into account spatial variability of water quality parameters. They typically consist of sampling at a few dates over a reference point in the waterbody. They are therefore not representative especially since *Chl-a* concentration might vary on the scale of days (Hunter et al., 2008; Stumpf et al., 2016). Moreover, synoptic *in situ* data acquisition and the examination of its horizontal variability within a short period of time through traditional field monitoring is difficult and expensive.

Current advances in the satellite remote sensing field, made it possible to enhance data acquisition (e.g. water surface temperature, *Chl-a* concentration), spatially and temporally. For example, the recent launch of Sentinel-2 satellites provides a greater coverage of water constituents with an increased spatial (10 m) and temporal resolution (5 days) suitable for the monitoring of small to medium size lakes and reservoirs. Further, the thermal infrared sensors onboard of Landsat satellites (since 1984) are adequate tools for monitoring surface temperature of small to medium size lakes and reservoirs with a bi-weekly frequency, as well as for performing retrospective analysis.

Still, remote sensing tools do not offer an explanation for the spatial distribution of water constituents shown in remotely sensed images. Further, they provide depth-information limited to the surface water layer, very thin for water temperature, the top 100 µm or a few meters (Secchi depth) for *Chl-a*. On the other hand, the temporal domain of satellites suitable for monitoring small to medium size waterbodies (e.g. Landsat and Sentinel-2) is not covered adequately.

In this case, numerical models which cover the entire spatial (vertical and horizontal) and temporal domains can provide means to interpret these images and interpolate temporal gaps. Several ecological models, coupled to one (1D) or three-dimensional (3D) hydrodynamic models, have been developed to study lake and reservoir ecological processes (Vinçon-Leite et al., 2019). These models integrate chemical, physical and biological processes. However, for a comprehensive overview of phytoplankton dynamics the application of 3D models is more appropriate.

Such models play a role in enhancing the ecological understanding of lakes and reservoirs. They enable studying eutrophication processes and support water management decisions to control phytoplankton blooms. Hydrodynamic-ecological models are aimed to predict cyanobacterial biomass and occurrence in relation to changes in environmental variables. This applies to total cyanobacterial occurrence or abundance and the occurrence of specific taxa. Results obtained from *in situ* observations, remote sensing and modeling could serve as basis for building a warning system for the prediction of cyanobacterial blooms occurrence and intensity.

Most studies regarding freshwater harmful algal blooms handled the issue by applying either remote sensing or modeling techniques. The combination of *in situ* data remote sensing techniques and modeling presents a new perspective for monitoring and assessing water quality of lakes and

reservoirs. This integration in studies regarding harmful algal blooms is very seldom in medium-size lakes with a surface area below 100 km^2, while most studies deal with coastal and ocean algal dynamics at larger space and time scales (Allan, 2014; Wynne et al., 2011).

Karaoun Reservoir is the largest freshwater body in Lebanon. Having to serve many purposes such as irrigation, hydropower, recreational activities, fisheries and future drinking water production; there is a great interest in monitoring the water quality of this reservoir. Especially that it has been suffering from severe cyanobacterial blooms events (Fadel et al., 2015). The application of coupled field observations, modeling and remote sensing techniques represents a new survey approach for Karaoun Reservoir.

Major objectives
The overreaching objective of this work is to propose and highlight the benefits of a new survey approach for monitoring the water quality of medium-sized reservoirs by combining *in situ* measurements, satellite remote sensing and modeling. Lakes and reservoirs in the Middle East including Karaoun Reservoir are poorly monitored which usually hinders appropriate management strategies. On the one hand, 3D modeling provides means to understand and explain the ecological and hydrodynamic processes taking place over long periods of time and in the whole lake. This includes the dynamics of cyanobacterial blooms. On the other hand, satellite imagery constitutes a complementary and valuable source of data for both modeling and *in situ* measurements. The following intermediate objectives were drawn:

• To develop and/or validate satellite remote sensing algorithms for the monitoring of water surface temperature, Secchi disk depth and *Chl-a* concentration.

• To conduct a retrospective analysis of water surface temperature using validated satellite data.

• To reproduce the hydrodynamics and ecological processes including cyanobacterial dynamics in space and time using a 3D numerical model.

General approach

One of the main objectives of this PhD is to apply modeling as a tool to reproduce the dynamics of cyanobacteria blooms in space and time. Modelling the fluxes of nutrients and phytoplankton requires an understanding of the evolving physical state. Thus, a 3D hydrodynamic-ecological model, the Delft3D suite (version 4.01.01.rc.03.) was used. 3D modelling allowed the estimation of harmful algal blooms transport, growth and decay at Karaoun Reservoir and to understand the factors leading to a heterogeneous distribution. From a management point of view, this will aid in taking appropriate management decisions and regulating future drinking water intake and recreational activities. The model was configured to simulate water temperature and water level fluctuations.

Satellite remote sensing is an effective tool for capturing the spatial distribution of water quality parameters on a synoptic scale including water surface temperature and *Chl-a* as an indicator of algal blooms. Thus, it can confirm spatial heterogeneity and the need for models with horizontal dimensions. At Karaoun Reservoir, surface heterogeneities can be expected due to the input from the Litani River inflow into the Reservoir and also the transport by wind.

Water surface temperature derived from remote sensing is an additional source of data that complements *in situ* measurements on a larger spatial scale. Remote sensing estimations of surface temperature and *Chl-a*, once validated, can be used to validate model simulations as well as to initialize the model when no measurements are available. Although this could be to a certain extent challenging under thermal stratification conditions. Remote sensing estimations can be also used to assess the ability of 3D models to reproduce spatial heterogeneities. In return the model can be used to explain the horizontal distribution of surface temperature and *Chl-a* shown in remote sensing images.

Satellite images from the Landsat 8 Thermal InfraRed Sensor (TIRS) were used to derive water surface temperature at Karaoun Reservoir. Landsat 8 has a suitable spatial resolution for monitoring medium to small size reservoirs. Images were atmospherically corrected using calibrated algorithms. An evaluation of the most commonly used algorithms was conducted in order to select the most appropriate approach for deriving accurate water surface temperature from Landsat 8 thermal data. New generation satellites, Sentinel-2 A and B, with a high spatial resolution and a 5-day revisit cycle were used to estimate *Chl-a* concentrations at Karaoun Reservoir. These images were atmospherically corrected.

Field measurements (water level, transparency, water temperature, *Chl-a*, phycocyanin, nutrients) will serve for calibration and validation of the Delft 3D modules (Flow for temperature and hydrodynamics and BLOOM for biogeochemical processes) as well as for remote sensing algorithms. Additional data were collected, including meteorology and inflow and outflow rates, required as input to the model.

A representation of the methodological approach is shown in Figure 1.
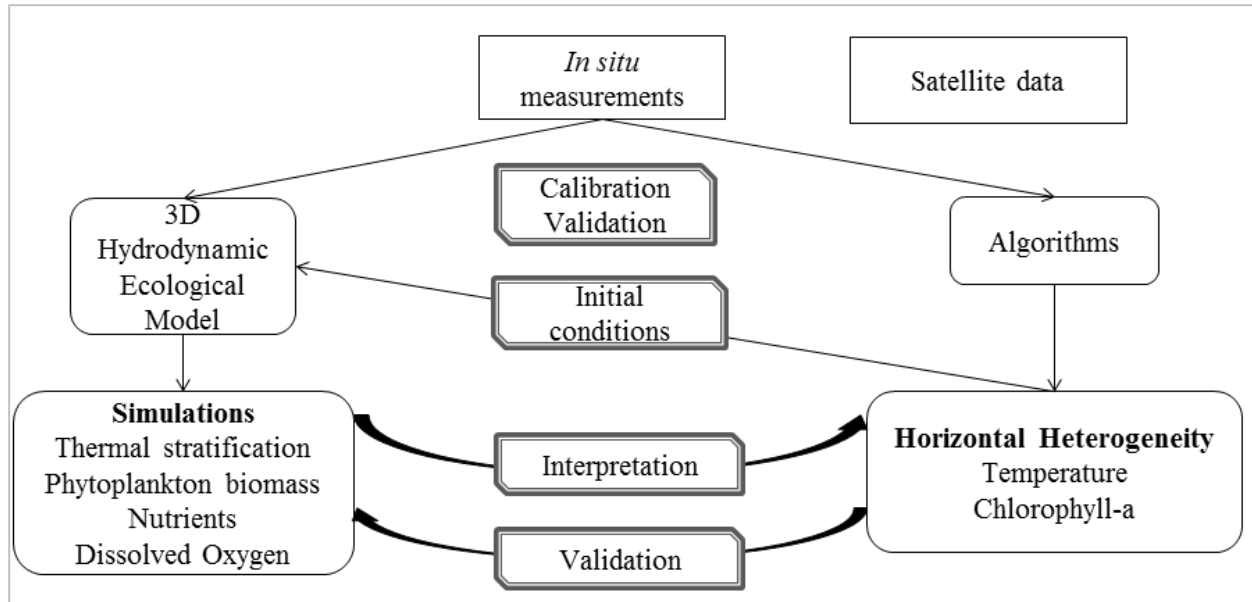
Figure 1: Representation of the general approach for combining *in situ* measurements, remote sensing data and modeling techniques.

Thesis overview

This thesis consists of seven chapters. **Chapter 1** is a bibliographic review highlighting the problems associated with cyanobacterial blooms in lakes and reservoirs and the corresponding monitoring strategies such as satellite remote sensing and hydrodynamic-ecological modeling. It also focuses on the coupling between measurements, satellite remote sensing and 3D modeling. **Chapter 2** describes the study site, Karaoun Reservoir and the methods used in field sampling, pre-processing of remote sensing images and algorithms development for deriving surface temperature and *Chl-a* concentrations. A description of the applied 3D hydrodynamic-ecological model with its configuration, calibration and validation approaches are presented at the end of this chapter which is followed by the results chapters. **Chapter 3** consists of the definition of the modeling objectives and an analysis of the data previously collected in 2012 and 2013 and those collected at the time of this work in 2017 and 2018. **Chapter 4** presents the results of water surface temperature retrieval from Landsat thermal sensors after validation and the evaluation of several atmospheric correction algorithms. A historical trend analysis of water surface temperature is also presented. The results of the 3D hydrodynamic modeling and a comparison with thermal satellite remote sensing data are presented in **Chapter 5**. The model was used to simulate water level variations and temperature at different depths which were compared to measurements. Maps of simulated water surface temperature were then compared to those retrieved from validated Landsat 8 data. **Chapter 6** presents the results of 3D ecological modeling of which the spatial distribution of *Chl-a* concentrations is further compared to that retrieved from satellite data. Finally, in **Chapter 7**, conclusions are drawn based on the results obtained from Chapters 4-6.

1. Chapter 1: State of the art

This chapter highlights the current problems facing lakes and reservoirs in terms of toxic cyanobacterial blooms, their traits, their anticipated expansion in the light of climate change, the need for continuous monitoring and for a better understanding of ecosystem processes, and the current approaches adopted for monitoring the water quality of affected ecosystems. The latter includes the limitations associated with conventional field monitoring methods, satellite remote sensing techniques and numerical modeling. This chapter also calls attention to: remote sensing data as a valuable source of data when *in situ* measurements are lacking and for modeling studies, the need to develop and /or validate remote sensing algorithms to derive water quality parameters from new generation sensors (Landsat 8 and Sentinel-2) in particular for medium to small size lakes and reservoirs. 3D hydrodynamic-ecological modeling is also stated for its contribution to the understanding of lake and reservoir hydrodynamic and ecological processes. Finally, the approach of coupling *in situ* measurements, satellite remote sensing and modeling techniques is highlighted for its importance as a more efficient survey approach which could serve for better management strategies.

1.1. Cyanobacterial blooms in inland waters: traits and environmental drivers

The water quality of inland waters and therefore the suitability of water to sustain various uses have been long influenced by anthropogenic activities. These include discharges of sewage, agricultural, industrial and urban wastewater. These activities cause increasing rates of nutrient inputs to freshwaters that would consequently become eutrophic.

Several problems arise from the eutrophication of inland waters, the most obvious being the rapid growth and accumulation of harmful algal blooms. Among the latter, cyanobacteria blooms have increased in intensity and frequency globally as well as disproportionally in comparison to other phytoplankton species (Huisman et al., 2018).

Cyanobacteria are traditionally known for harboring nuisance species (e.g. *Microcystis*, *Anabaena*, *Chrysosporum*), causing water quality deterioration and possible human health risks (Figure 2). The latter are mainly due to their ability to produce toxic compounds (cyanotoxins). When they are ingested by humans, they cause health risks which can vary from skin irritations to fever, intestinal problems, and neurological disorders (He et al., 2016). Moreover, these toxins can kill birds, mammals or fish that either ingest toxin-producing cells or absorb the toxin from water. Other negative effects causing ecosystem alteration include the decline in water transparency, oxygen concentration and biodiversity as well as economic losses. Such problems can severely limit the use of lakes and reservoirs as drinking water supplies, as well as for recreational activities, fisheries and aquatic habitats.
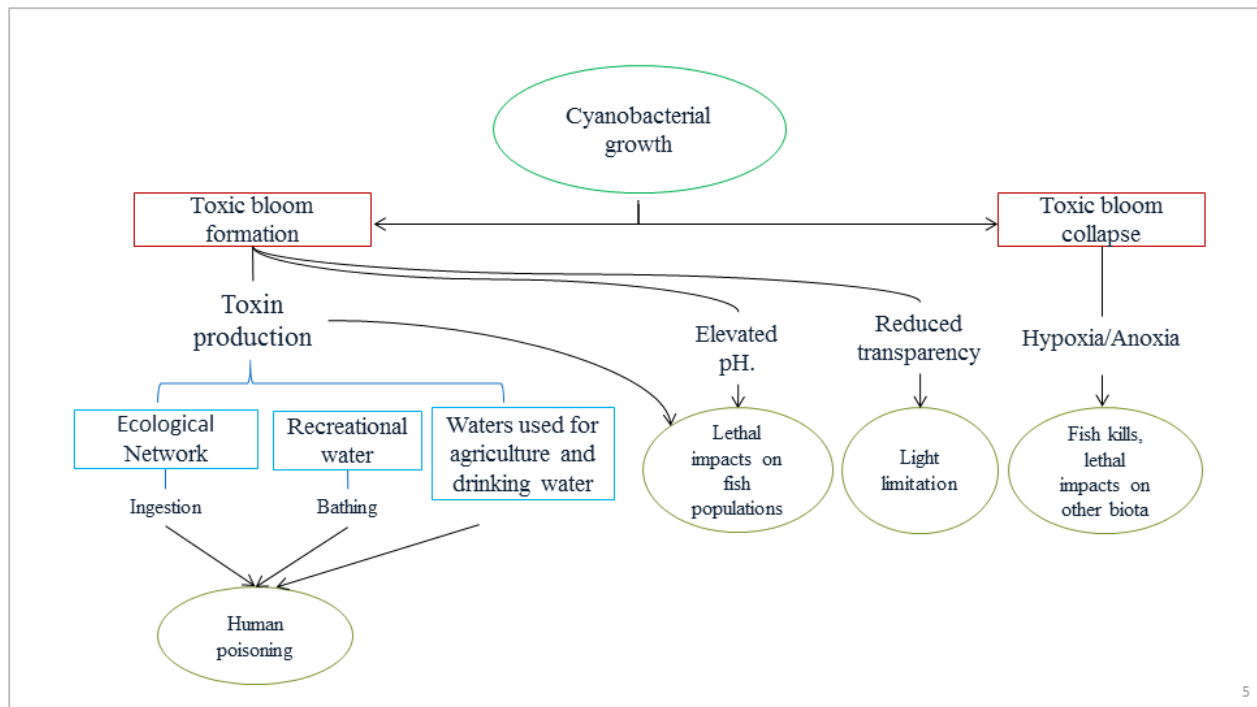
Figure 2: Negative impacts of cyanobacterial blooms.

Several traits have provided cyanobacteria with a competitive advantage over other eukaryotic phytoplankton and allowed them to dominate and form blooms. These include the fixation of atmospheric nitrogen, carbon dioxide (CO_2) concentration and buoyancy in addition to the production of cyanotoxins.

Some cyanobacteria genera (e.g. *Chrysosporum* or *Aphanizomenon, Nodularia* and *Cylindrospermopsis*, also known as diazotrophic cyanobacteria), unlike other eukaryotic phytoplankton, have the ability to fix atmospheric Nitrogen by means of specialized cells called heterocysts (Kumar et al., 2010). This gives them the advantage of developing blooms in environments where dissolved Nitrogen is limited and outcompete non-diazotrophic cyanobacteria. The process of Nitrogen fixation increases with temperature and thus at high temperatures and if nitrogen is the limiting factor, diazotrophic cyanobacteria are expected to thrive.

Cyanobacteria can fix Carbon for photosynthesis and growth through CO_2–concentrating mechanisms allowing them to increase CO_2 concentrations in their cells (Visser et al., 2016). Blooms of cyanobacteria usually deplete dissolved CO_2 (and thereby raise the pH) however; these mechanisms will provide them sustainability. It is thus considered that cyanobacteria are competitive at low dissolved CO_2 concentrations.

Several cyanobacteria species possess gas vesicles which allow them to regulate their buoyancy and float. Buoyant cyanobacteria are therefore able to adjust their position in the water column for optimal irradiance and nutrient uptake (Reynolds, 2006). Under low wind velocities, blooms of buoyant cyanobacteria can accumulate at the water surface, shade other phytoplankton species and take advantage of the influx of atmospheric CO_2.

The increasing trend of cyanobacterial blooms occurrence is likely to continue in a context of eutrophication, rising CO_2 concentrations and temperatures. All have been recognized to promote the persistence and development of cyanobacterial blooms in lakes and reservoirs (Figure 3).

As mentioned before, the eutrophication of inland waters, resulting from anthropogenic inputs of mainly nitrogen and phosphorus, has been an essential driver of cyanobacterial blooms. Thus, reducing nutrient inputs into freshwaters has become of primary concern in order to control the development of cyanobacterial blooms (Paerl, 2017). Still, most efforts concentrated on reducing the Phosphorus (P) input rather than Nitrogen (N). Although P has been long considered the limiting nutrient for phytoplankton growth, recent research has proven that high N loading can promote non-diazotrophic cyanobacteria such as *Microcystis* strains and increase the amount of the toxins they are able to synthetize (e.g. microcystins) (Gobler et al., 2016).

Higher future CO_2 concentrations are also likely to favor the development of cyanobacterial blooms. While most studies focused on increasing temperatures, fewer addressed the effect of increasing atmospheric CO_2 concentrations on cyanobacteria, mainly because freshwater lakes are considered to be super-saturated with CO_2 and to cyanobacteria ability to utilize bicarbonate as a source of Carbon (Visser et al., 2016).

Blooms often deplete dissolved CO_2 in surface freshwaters, thereby inducing high pH values. Rising concentrations of atmospheric CO_2 due to human activities will improve the influx of dissolved CO_2 into the water surface which in turn will be used by cyanobacterial blooms. Hence, dense cyanobacterial blooms are expected to intensify with rising CO_2 in eutrophic waters (Sandrini et al., 2016).

While the connection between eutrophication and cyanobacterial blooms expansion is well-established, recently climate change has been widely implicated (Moss et al., 2011). It can promote cyanobacterial blooms in three ways: higher temperatures, stronger and longer stratification and more intermittent nutrient input.

The growth rate of cyanobacteria highly depends on temperature and often reaches its maximum at relatively high temperatures between 20 and 30 °C (Konopka & Brock, 1978). This will provide a competitive advantage of cyanobacteria over eukaryotic phytoplankton in freshwaters, since eukaryotic phytoplankton growth rate stabilizes or decreases at high temperatures.
The warming of surface waters also strengthens and lengthens the period of the vertical stratification in freshwater ecosystems, hence reducing vertical mixing. On the one hand, since

many cyanobacteria species are able to regulate their buoyancy, they can exploit stratified conditions by forming dense surface blooms and take advantage of high levels of irradiance to optimize photosynthesis. On the other hand, stratified conditions will preferentially promote the sinking of phytoplankton with weak buoyancy regulation mechanisms.

Finally, climate change can influence the hydrology by affecting the duration and intensity of precipitation and drought events (Paerl & Huisman, 2009). Under increased precipitation events, waterbodies can be enriched with nutrients from runoffs. This will also favor cyanobacterial blooms during the summer period that follows owing to longer residence time of nutrient-rich waters. For all of these reasons and with future warming, cyanobacterial blooms are expected to increase in distribution, duration and intensity.
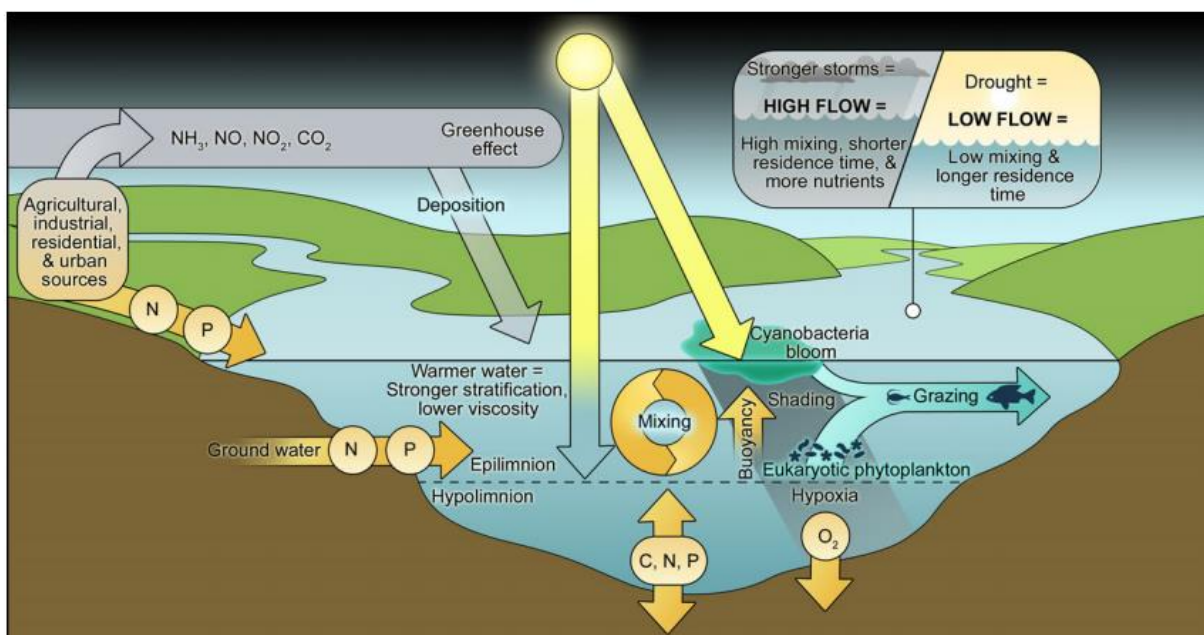
Figure 3: Environmental factors controlling harmful cyanobacterial blooms. Adapted from (Paerl, 2017).

The impact of water level fluctuations (WLF) on cyanobacterial blooms has not been often addressed particularly in reservoirs where, unlike in natural lakes, the magnitude of fluctuations is significant. WLF have been shown to influence cyanobacteria biomass and occurrence by impacting nutrient dynamics and thermal stability (Bakker & Hilt, 2016).

In summer, when thermal stratification is established, the drawdown in the water level due to reduced inflows and withdrawals leads to the decrease in water volume and the thickness of the hypolimnion in which nutrient concentrations is higher. This leads to an alteration of thermal stratification, an elimination of the thermocline and to full mixing (Soares et al., 2019). As a result, an upward flux of nutrients into the water column is triggered, which promotes the abundance of cyanobacteria (Naselli-Flores & Barone, 2003).

Because of the problems and health risks associated with cyanobacterial blooms, there is a strong need to conduct regular monitoring and assessment of physical, chemical, hydrological and biological components of freshwater ecosystems in order to understand their functioning, the dynamics of cyanobacteria and to ensure optimal management strategies.

Lake and reservoir ecosystems have important functions in the environment as they provide multiple ecosystem services. Nevertheless, they are among the most extensively altered ecosystems on earth mainly due to anthropogenic activities and their vulnerability to climate change (Adrian et al., 2009). In order to address these problems, several water directives in the world aim to enhance the water quality of these ecosystems through regular monitoring of water constituents (Federal Water Pollution Control Act., 2002; Wernersson et al., 2015; European Union, 2000). Based on the latter, this should ultimately lead to a better understanding of ecosystem functioning including hydrodynamic and ecological processes and thus implementing appropriate management strategies.

1.2. Remote sensing of lakes and reservoirs

1.2.1. Overview

Current field based conventional monitoring is costly, time consuming and labor intensive. The resulting *in situ* measurements are limited in terms of spatial and temporal resolutions. They are restricted to unevenly distributed point based representations of dynamic systems which may not adequately reflect the water quality and its classification. This sampling is hence insufficient for capturing spatial variations in water quality. For example, *Chl-a* concentration, an estimate of phytoplankton biomass, can vary during short periods of time and exhibit heterogeneous distributions in lakes and reservoirs (Bowling et al., 2015; Guan et al., 2018). In this context, the inability of *in situ* samples to capture the spatial pattern of *Chl-a* distribution may lead to uncertainties in estimations.

In order to overcome such limitations and broaden the knowledge about ecosystem processes, remote sensing techniques have been integrated in water quality monitoring as a complementary source of data for an effective monitoring strategy (Politi et al., 2012; Hestir et al., 2015). In contrast to traditional methods, remote sensing is an effective approach at a low cost offering high frequency data and operating on a large synoptic scale.

For decades, remote sensing has been used for freshwater ecosystem surveys (Strong, 1974). However, the use of remote sensing to monitor open oceans and terrestrial ecosystems (Gomez et al., 2016; Werdell et al., 2018) has been far more successful in comparison to inland waters and more specifically small to medium size lakes and reservoirs. This is mainly due to the coarse spatial resolution of sensors onboard satellites which were only suitable for monitoring large water bodies. Moreover, the complex interactions between several constituents in inland waterbodies (e.g. phytoplankton, detritus, colored dissolved organic matter (CDOM) and non-algal particles) are challenging for developing accurate remote sensing models (Ogashawara et al., 2017).

Because of the different water composition between open oceans and inland waters, the classification of water types as Case 1 and Case 2 waters was proposed (Gordon & Morel, 2012) and is mostly adopted. Based on this classification, inland waters mostly belong to Case 2 waters whose optical properties are majorly influenced by mineral particles, CDOM which concentrations do not vary with phytoplankton. On the other hand, the optical properties of Case 1 waters are mainly driven by phytoplankton.

With the improvement in sensor spatial and spectral resolution, the application of remote sensing techniques to smaller freshwater ecosystems has increased. For instance, sensors onboard new generation multispectral satellites, Landsat-8 and Sentinel-2, offer finer radiometric and higher spatial resolutions, and are adequate for applications over small lakes and reservoirs. With these recent advances the importance of remote sensing monitoring of inland waters has increased (Palmer et al., 2015).

From the water leaving radiance in the visible and near-infrared (NIR) wavelengths, remote sensors are capable of providing information about lake properties such as hydrology, biota and transparency each with their corresponding constituents (Figure 4) (Dörnhöfer & Oppelt, 2016). The most commonly measured water constituents by means of remote sensing include: *Chl-a*, transparency expressed as Secchi disk depth (SDD), the light attenuation coefficient (K_d), surface temperature, CDOM, turbidity, suspended particulate matter (SPM) and recently the phycocyanin pigment (*PC*).
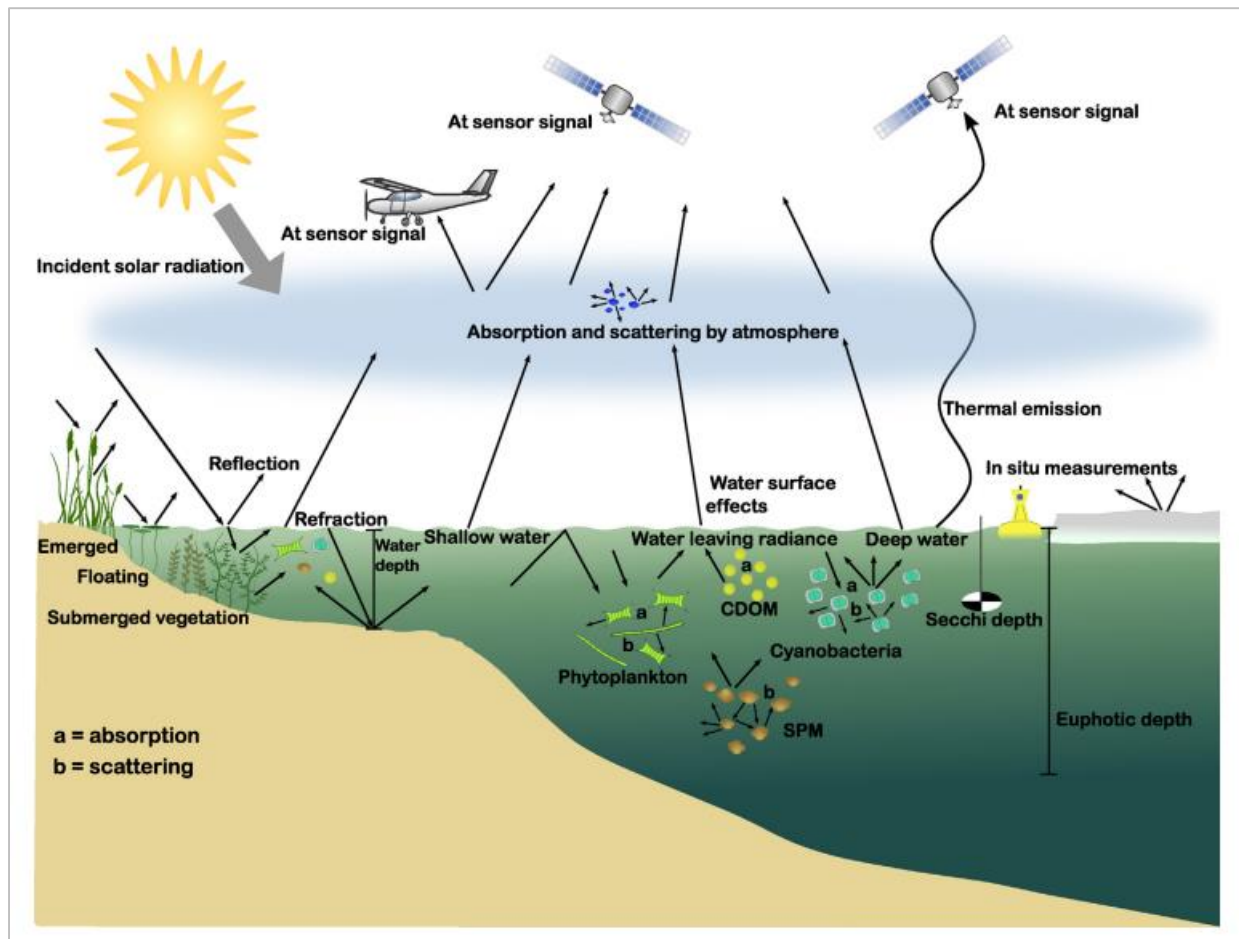
Figure 4: Interaction between radiation, remote sensing indicators and lake ecology and sensors. Adapted from (Dörnhöfer & Oppelt, 2016).

Several remote sensing algorithms or approaches exist for quantifying water constituents or parameters in the visible and NIR spectrum including empirical, semi-empirical and analytical approaches.

The simplest category is the empirical approach which is based on establishing a statistical relationship (regressions, least squares and neural networks) between *in situ* observations and remote sensing data measured in multiple bands or band combinations. The focus of this method is to obtain the best correlation between remote sensing reflectance and the concentration of the constituent of interest. However, its application is often site-dependent. A review of empirical approaches for inland and near-coastal transitional waters can be found in Matthews (2011).

The semi-empirical approach is more advanced but also based on statistical relationships between *in situ* measurements and radiometric data. The difference between empirical and semi-empirical models is that the latter include specific spectral features of the constituent governing reflectance in the statistical analysis. Thus the selection of bands depends on the physical principle behind the

characteristics of the spectral features (Giardino et al., 2007; Ogashawara et al., 2017). Similar to the empirical approach, semi-empirical algorithms are limited in transferability.

The analytical or model-based approach is a physics-based approach which renders it broadly applicable. It depends on the inversion of the radiative transfer equation through which it establishes relationships among the inherent and apparent optical properties. An example of this can be found in Dekker et al. (2001).

Deriving surface water temperature in lakes and reservoirs requires remote sensing data recorded in the thermal infrared. Several algorithms were developed to retrieve surface temperature (Cristóbal et al., 2018; Wang et al., 2015). Depending on the number of thermal bands in sensors, algorithms making use of only one thermal band (mono-window or single channel algorithms) were mostly developed and suited for application to Landsat data (Jiménez-Muñoz & Sobrino, 2003). They are based on approximations of the radiative transfer equation (RTE) and atmospheric parameters as input (e.g. water vapor data). Algorithms requiring two thermal bands also known as split-window algorithms were also developed to increase the accuracy of estimations (García-Santos et al., 2018).

With the ongoing progress in space sciences, remote sensing has become an effective tool for the monitoring and management of inland water quality in conjunction with traditional field surveying. A large number of spaceborne and airborne sensors is used to detect different water quality parameters in lakes and reservoirs (Pu et al., 2017). For the objective of water quality studies, selecting an appropriate sensor among many others available, requires an understanding of its unique attributes.

1.2.2. *Spaceborne sensors*
Spaceborne sensors in general have a frequent revisit period, a coarse spatial resolution and, based on their spectral resolution, they can be classified as multispectral and hyperspectral. The majority of spaceborne sensors is multispectral, providing images in a few spectral bands compared to hyperspectral sensors (Gholizadeh et al., 2016).

In a recent review about spaceborne and airborne sensors, Gholizadeh et al. (2016) detailed the most commonly used spaceborne sensors in water quality assessment. These include WorldView-2 and WorldView-3, Landsat 8, MODIS (Moderate Resolution Imaging Spectroradiometer) and MERIS (Medium Resolution Imaging Spectrometer). The spatial resolution of these sensors is primarily what determines their utilization in inland water quality studies depending on the size of the ecosystem. Based on their spatial resolution, spaceborne sensors can be grouped under high, medium and coarse spatial resolution (Giardino et al., 2014).

High spatial resolution sensors such as Quickbird, IKONOS and WorldView 1 and 3 provide images with different spectral resolutions for different spectral bands respectively at 2.62 - 0.65, 3.2 - 0.82, 0.5 and 1.85 - 0.46 m with the following daily periods, 2.5, 3, 1.7 and 1.1 days. However, the acquisition of images is expensive and available on demand.

Coarse spatial resolution sensors including the ocean color MERIS and MODIS have high acquisition frequencies (daily and every 1 to 2 days respectively) and a finer spectral resolution than multispectral sensors, which makes them suitable for accurately detecting water constituents. These sensors have been extensively applied to derive water quality parameters in inland waters (Table 1). However, their different coarse spatial resolutions attributed to different spectral bands (MERIS 300 - 1200 m and MODIS 250 - 500 – 1000 m) made their application mostly suitable to lakes and reservoirs with a large surface area, usually greater than 14 km^2 (Table 1). Moreover, Philipson et al. (2014) demonstrated the limitation of MERIS spatial resolution (300 m) for monitoring small lakes in the frame of the Water Framework Directive (European Union, 2000).

Table 1: A list of MERIS and MODIS applications to large lakes and reservoirs for the retrieval of water constituents.

	Lake/Reservoir	Surface area (km^2)	Sensor	Reference
Chl-a **SPM**	Lake Trasimeno, Italy	124	MERIS	Giardino et al., 2010
Chl-a	Lake Como, Italy	145	MERIS	Bresciani et al., 2011
	Lake Constance, Germany	536	MERIS	
	Lake Garda, Italy	370	MERIS	
	Lake Geneva (Switzerland/France)	580	MERIS	
	Lake Interlaken, Switzerland	48.3	MERIS	
	Lake Iseo, Italy	65.3	MERIS	
	Lake Lucerne, Switzerland	113.6	MERIS	
	Lake Varese, Italy	14.5	MERIS	
	Lake Zug, Switzerland	38.3	MERIS	
	Lake Zurich, Switzerland	88.66	MERIS	
Chl-a **CDOM**	Lake Maggiore	212	MERIS	Bresciani et al., 2011 Giardino et al., 2014
	Alqueva Reservoir, Portugal	250	MERIS	Potes et al., 2011
Chl-a **PC**	23 reservoirs, Spain	73 max	MERIS	Medina-Cobo et al., 2014
Chl-a	Lake Geneva (Switzerland/France)	580	MERIS	Kiefer et al., 2015
	Lake Dongting, China	2691	MERIS	Lyu et al., 2015
	Lake Dianchi, China	306	MERIS	
	Three Gorges Reservoir, China	1084	MERIS	
	Lake Chaohu, China	~760	MERIS MODIS	Lyu et al., 2015 Duan et al., 2017
Chl-a **SPM**	Lake Taihu, China	2238	MERIS MODIS	Lyu et al., 2015 Wang et al., 2011 Zhang et al., 2010
Chl-a **SDD** **SPM**	Lake Erie, USA	25,700	MERIS MODIS	Zolfaghari & Duguay, 2016 Binding et al., 2010
Chl-a **K$_d$**	Lake Tanganyika, Africa	32,900	MODIS	Horion et al., 2010
Chl-a	Itumbiara Reservoir, Brazil	814	MODIS	Ogashawara et al., 2014
	Passo Real Reservoir, Brazil	233.39	MODIS	Breunig et al., 2016
	Porto Primavera Reservoir, Brazil	2250	MODIS	Eraso et al., 2018

Currently, there are not many hyperspectral sensors in space with the spatial resolution required for the monitoring of small inland waterbodies. Due to their high spatial resolution, multispectral medium spatial resolution sensors onboard Landsat and the new generation Sentinel-2 satellites are suitable for this type of monitoring.

The joint NASA/USGS Landsat program represents the longest archive of satellite imagery since 1984 and an important source of data for historical water quality studies. Landsat imagery has been used extensively in water quality studies. This program is equipped with the MSS (Multispectral Scanner) onboard Landsat 1, 2 and 3, the TM (Thematic Mapper) onboard Landsat 4 and 5 and the ETM+ (Enhanced Thematic Mapper Plus) onboard Landsat 7 (Table 2). Landsat 8 (launched in 2013), the latest satellite in the Landsat Data Continuity Mission (LDCM) project, holds two sensors, the Operational Land Imager (OLI), and the Thermal Infrared Sensor (TIRS) (Table 2). It has improved better radiometric resolution (12 bit) than previous Landsat series and has a revisit period of 16 days.

Table 2: Landsat TM, ETM+, OLI and TIRS band designations.

	Bands	**Wavelength (µm)**	**Resolution (m)**
Landsat 4-5 (TM)	Band 1	0.45 - 0.52	30
	Band 2	0.52 - 0.60	30
	Band 3	0.63 - 0.69	30
	Band 4	0.76 - 0.90	30
	Band 5	1.55 - 1.75	30
	Band 6	10.40 - 12.50	120 (30)
	Band 7	2.09 - 2.35	30
	Band 8 (ETM+ only)	0.52 – 0.9	15
Landsat 8 (OLI & TIRS)	Band 1 – Coastal aerosol	0.43 - 0.45	30
	Band 2 – Blue	0.45 - 0.51	30
	Band 3 – Green	0.53 - 0.59	30
	Band 4 – Red	0.64 - 0.67	30
	Band 5 – NIR	0.85 - 0.88	30
	Band 6 – SWIR 1	1.57 - 1.65	30
	Band 7 – SWIR 2	2.11 - 2.29	30
	Band 8 – Panchromatic	0.50 - 0.68	30
	Band 9 – Cirrus	1.36 - 1.38	30
	Band 10 (TIRS) 1	10.6 - 11.19	100
	Band 11 (TIRS) 2	11.50 - 12.51	100

The high frequency revisit time (5 days) of new generation satellites launched by the European Space Agency (ESA), Sentinel-2 A (launched in 2015) and Sentinel-2 B (launched in 2017) provides new opportunities for regular monitoring of inland waters. In addition to four visible channels, the MultiSpectral Instrument (MSI) onboard Sentinel-2 satellites, holds three near-infrared bands (Table 3) that allow for the retrieval of water quality parameters such as *Chl-a* in a more effective way.

Table 3: Sentinel – 2A and Sentinel – 2B Multi-Spectral Instrument (MSI) band designations.

	Sentinel – 2A (MSI)		Sentinel – 2B (MSI)	
	Central wavelength (nm)	Resolution (m)	Central wavelength (nm)	Resolution (m)
Band 1	442.7	60	442.2	60
Band 2	492.4	10	492.1	10
Band 3	559.8	10	559.0	10
Band 4	664.6	10	664.9	10
Band 5	704.1	20	703.8	20
Band 6	740.5	20	739.1	20
Band 7	782.8	20	779.7	20
Band 8	832.8	10	832.9	10
Band 8a	864.7	20	864.0	20
Band 9	945.1	60	943.2	60
Band 10	1373.5	60	1376.9	60
Band 11	1613.7	20	1610.4	20
Band 12	2202.4	20	2185.7	20

The potential of Landsat 8 OLI and Sentinel-2 MSI for water quality monitoring has not been fully exploited yet in comparison to previous sensors. Recent attempts have focused on developing or validating algorithms for detecting water constituents in inland waters. More validation over optically complex inland waters and appropriate atmospheric correction algorithms are necessary (Ansper & Alikas, 2019).

Individually, the utility of OLI and MSI for monitoring inland water quality has been demonstrated in a few publications (Lavrova et al., 2016; Watanabe et al., 2018; Zhou et al., 2019). However, not many efforts have been made to evaluate the combined use of OLI and MSI data which should provide high temporal coverage (Wang et al., 2017).

The sensors OLI and MSI have similar spectral bands: the visible bands, the short wave infrared bands and a near infrared NIR band (865 nm) and recently they have been shown to provide similar reflectance values in water (Pahlevan et al., 2019). The fusion of both OLI and MSI imagery will provide an average global revisit interval of ~ 2.9 days (Li & Roy, 2017). Considering cloud coverage, such frequent revisits will enable to capture the dynamics of inland waters at unprecedented rates and in a more operational way (Page et al., 2019).

 Concentrations of *Chl-a* and water surface temperature are important parameters to detect in lakes and reservoirs as they provide insights about the ecological status and functioning of these ecosystems. The characteristics of the OLI and MSI sensors render it possible to acquire information about these parameters on broader spatial and temporal scales using appropriate algorithms (OLI: *Chl-a* and temperature; MSI: *Chl-a*).

1.2.3. *Water surface temperature*

Lake water temperature is a key parameter influencing the functioning of freshwater ecosystems. Gaining insight about the distribution of water surface temperature is crucial for understanding the hydrodynamic functioning and biological processes in lakes and reservoirs (Schmidt et al., 2018; Yang et al., 2018).

Conventional methods for water surface temperature measurements, which make use of thermistors on buoys and radiometry, might benefit from additional data from remote sensing, providing a larger spatial coverage of water characteristics over time. Coarse-spatial high frequency satellite sensors (e.g. the Advanced Very High Resolution Radiometer AVHRR, the Moderate Resolution Imaging Spectroradiometer MODIS) have been commonly used to map medium to large lakes worldwide (Giardino et al., 2010; Oesch et al., 2005; Reinart et al., 2008), as well as to develop time-series to assess the lake sensitivity to global change (O'Reilly et al., 2015; Pareeth et al., 2017).

As the spatial resolution of these sensors might be too coarse for mapping water surface temperature in smaller lakes or reservoirs, sharpening techniques or higher spatial resolution sensors have been alternatively used. For example, Teggi (2012) developed an algorithm for improving the spatial resolution of ASTER from 90 to 30 m to map water surface temperature in coastal waters and of watercourses, while other studies made use of Landsat imagery (Giardino et al., 2001; Huang et al., 2017; Wloczyk et al., 2006).

In particular, although with a roughly bi-weekly revisiting time, Landsat 4 and 5 TM (Thematic Mapper, 1984-2013, spatial resolution of the thermal band 120 m), Landsat 7 ETM+ (Enhanced Thematic Mapper, since 1999, spatial resolution of the thermal band 60 m) and the most recent Landsat 8 TIRS (Thermal Infrared Sensor, since 2013, spatial resolution of the thermal band 100 m) have the appropriate spatial resolution for mapping medium to small size waterbodies. Since the Landsat Data Continuity Mission program holds an impressive continuous record of 45 years of imagery data at an approximately bi-weekly revisiting time, Landsat is a prime platform for retrospective studies on thermal properties of inland waters.

Yet, studies attempting to use time series of Landsat images to determine the temporal changes in surface water temperature in lakes and reservoirs are scarce. Simon et al. (2014) recommended the use of a single channel algorithm for correcting archives of Landsat single-band thermal infrared data. Rodríguez et al. (2014) used the Landsat TM archive and showed its potential to describe periodic behaviors such as surface water temperature in wetlands.

Owing to the trade-off between spatial and temporal resolutions, several techniques (data fusion or disaggregation) have been developed to derive surface temperature at high spatial and temporal resolutions from existing remote sensing data (Zhan et al., 2013). These approaches generate data with fine spatial resolution and temporal frequency by combining multi-sensor spatial and temporal characteristics. Most of them were used for land surface temperature retrieval (Bindhu et

al., 2013), while their application to inland waters is very scarce. Examples of these techniques include the fusion of Landsat 8 panchromatic and thermal infrared images to enhance the spatial resolution of the latter (Jung & Park, 2014) and disaggregating surface temperature from MODIS images to the Landsat spatial resolution using Landsat visible-near-infrared data (Bisquert et al., 2016). Yet, the models or algorithms implicated in these techniques require additional validation and improvement (Chen et al., 2015).

In order to obtain accurate and comparable measurements of water surface temperature from spaceborne observations, atmospheric corrections accounting for atmospheric attenuation and emission must be performed for each image.

1.2.3.1. *Atmospheric correction*
Several approaches have been proposed to correct for atmospheric contributions. One way is to apply directly the radiative transfer equation (RTE) which requires atmospheric parameters including transmissivity and downwelling and upwelling radiances (Barsi et al., 2014, 2005). The method has been successfully applied to characterize the impact of river plumes in marine waters during a significant flood event (Brando et al., 2015).

Another way is to use its approximation, the generalized single-channel algorithm (SC1) developed by Jiménez-Muñoz & Sobrino (2003) and further improved (SC2) in Cristóbal et al. (2018) or the mono-window algorithm (MW) by Qin et al. (2001) and Wang et al. (2015). The SC1 algorithm reduces the need for local data to atmospheric water vapor content and emissivity. However, an error in water vapor content or values outside its validity range (> 3 g cm-2) might increase the errors in retrieving surface temperature. The SC1 algorithm can be applied to any thermal infrared sensor. It was mostly used for surface temperature retrieval over land (Isaya Ndossi et al., 2016) while few studies dealt with direct applications to inland waters (Lamaro et al., 2013; Prats et al., 2018). Furthermore, it was more often validated for Landsat 4, 5 and 7 than for Landsat 8 which is the most recent.

Because the SC1 algorithm only depends on water vapor content and emissivity, Cristóbal et al. (2018) proposed an improved version of the SC1 algorithm (hereafter denoted the SC2 algorithm) in order to minimize the errors associated with the amount of water vapor content. The SC2 algorithm has a supplementary input, near-surface air temperature. It operates on a wider range of water vapor content and air temperature and was evaluated for Landsat 8 TIRS.

The MW algorithm has been used for retrieving surface temperature from the thermal bands of Landsat sensors (TM, ETM+ and TIRS). Similarly to the RTE and the SC1 and SC2 algorithms, the MW algorithm requires atmospheric parameters including emissivity, atmospheric transmissivity and effective mean atmospheric temperature.

The launch of Landsat 8 with two thermal bands (Band 10: 10.6 – 11.19 μm and Band 11: 11.5 – 12.51 μm) allowed the application of split-window algorithms that have been developed since decades (Kerr et al., 1992) for correcting satellite data acquired with multiple bands in the thermal

infrared wavelengths. Unfortunately, due to the calibration uncertainties in Band 11, it is not recommended that Band 11 be used for the split-window technique (USGS-Landsat Mission 2017 [1]) which is why single-channel algorithms (also called mono-window algorithms) using Band 10 are more appropriate for surface temperature estimation (Reuter et al., 2015).

Despite current advances in Thermal InfraRed sensors, currently, sensors with both high spatial resolution and revisit periods are needed. In this context, recent French-Indian research efforts are in progress of defining a new satellite combining a high temporal resolution of about 3 days, a high spatial resolution of 50 m and providing global coverage in the TIR as well as in the visible-SWIR region of the spectrum. The launch of the TRISHNA mission (Thermal infraRed Imaging Satellite for High-resolution Natural Resource Assessment) is planned in 2024 (Lagouarde et al., 2018).

The availability of several approaches for atmospherically correcting thermal infrared imagery and their insufficient application to inland waters calls for additional validation studies especially over small to medium size waterbodies. Owing to the size and the lack of thermal bands onboard Sentinel-2, such studies should be conducted using Landsat thermal sensors for accurate estimations of surface temperature.

1.2.4. *Chl-a a concentration*

In lakes and reservoirs, the concentration of *Chl-a*, a spectrally active compound in phytoplankton, is an important indicator of water quality. It is commonly used as a proxy for phytoplankton biomass including cyanobacteria and to determine the trophic state (Baban, 1996). In the last several decades, the intensity and occurrence of cyanobacterial blooms, mainly driven by eutrophication, has increased in lakes and reservoirs worldwide (Harke et al., 2016). In monitoring the impact of eutrophication and consequently that of harmful algal blooms and the associated health risks, *Chl-a* is considered an important indicator of the presence of algal blooms. Remote sensing offers the ability to monitor and decrease the traditional field-uncertainty of the horizontal distribution of phytoplankton and cyanobacteria. As a result, the development and application of remote sensing algorithms for the detection of *Chl-a* concentration has increased (Palmer et al., 2015).

Unlike phycocynanin (*PC*), a pigment which is specific to cyanobacteria, *Chl-a* does not allow to differentiate between cyanobacteria and other phytoplankton groups. Although the focus of recent research has been on the development of *PC* algorithms (Sharaf et al., 2019a), the existing spectral characteristics of satellite sensors are more suited to *Chl-a* retrieval rather than *PC*. When a bloom consists of cyanobacteria and other eukaryotic algae, detection by *PC* is preferred; and when the bloom is dominated by cyanobacteria, *Chl-a* is a better choice because it offers greater remote sensing sensitivity than *PC* (Stumpf et al., 2016).

---

[1] https://www.usgs.gov/land-resources/nli/landsat/landsat-8-oli-and-tirs-calibration-notices

The specific spectral signature of *Chl-a* makes it possible to estimate it from remote sensing reflectance (Figure 5). It absorbs most energy at wavelengths in the blue (~ 440 nm) and red (~ 670 – 678 nm) regions of the electromagnetic spectrum and exhibits a reflectance peak near 700 nm in turbid waters (Matthews, 2017).
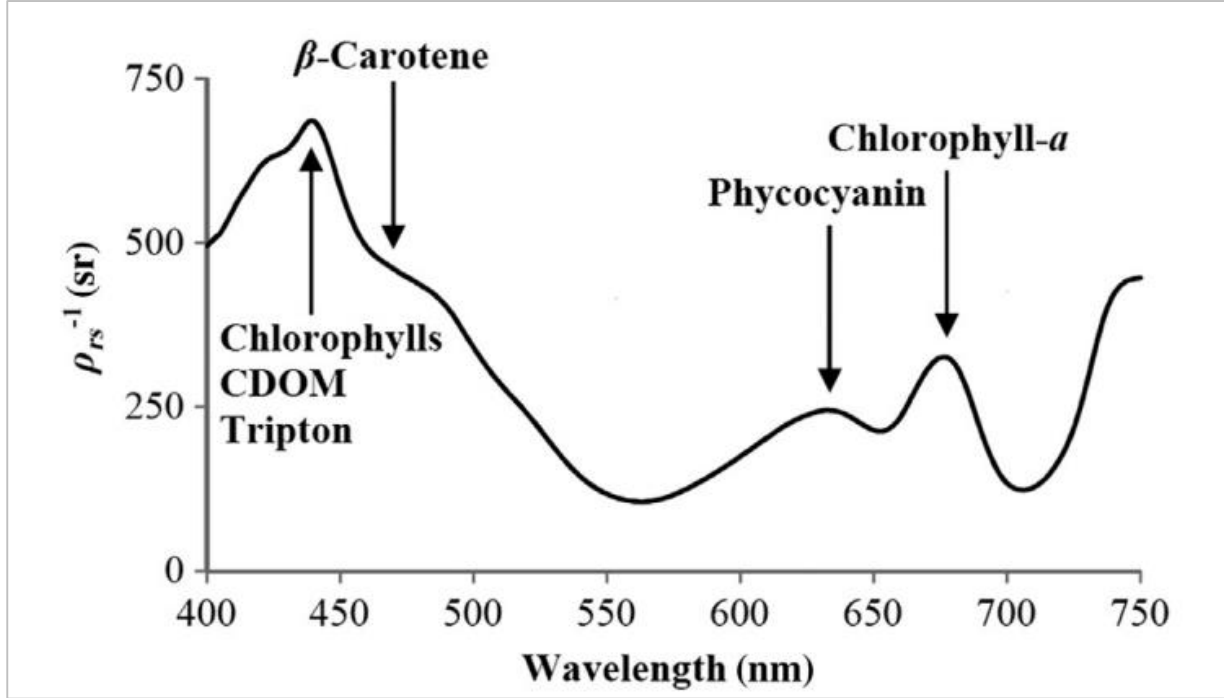
Figure 5: Typical inland waters inverse remote sensing reflectance (R_{rs}) spectrum. From Ogashawara et al. (2017).

Progress in the marine environment has been made in retrieving the concentration of *Chl-a* from remote sensing data using blue to green ratios (440 – 550 nm) because *Chl-a* exhibits a first absorption peak of around 440 nm and minimal absorption around 550 nm. In Case 1 oceanic waters where the optical properties are mainly due to phytoplankton, *Chl-a* can be accurately retrieved from standard calibrated and validated algorithms of ocean color sensors such as MERIS, MODIS and SeaWiFS (Sea-viewing Wide Field-of-view Sensor) (El hourany et al., 2017; Gregg et al., 2005).

In contrast, in inland waters, most of which are turbid and productive, *Chl-a* determination is challenging due to the complexity of optical properties. These optical properties are influenced by CDOM, detritus and suspended particles which vary independently from phytoplankton pigments. The absorption of CDOM can overlap in the blue spectral region thus making reflectance unsuitable for *Chl-a* estimations (Yacobi et al., 2011). Therefore, a number of *Chl-a* retrieval algorithms, with two or more bands, has been developed based on data in the red and near-infrared (NIR) spectral regions where the effect of absorption by CDOM and the scattering by mineral particles decreases and is small (Yang et al., 2017).

These algorithms were developed using data from spaceborne or airborne sensors with multispectral or hyperspectral resolutions and through different approaches (e.g. empirical, semi-empirical and analytical).

A widely used algorithm in Case 2 waters is the two band NIR-red ratio model (Gitelson, 1992) which uses wavelengths in the NIR where reflectance is minimally sensitive to the absorption by *Chl-a* (near 700 nm) and wavelengths in the red where reflectance is located in the range of *Chl-a* absorption peak (near 670 nm). Menken et al. (2006) found that the ratio of reflectance at 700 nm to that at 670 nm collected in August of 2001, was the best predictor of *Chl-a* ($R^2 = 0.84$) in 15 lakes in east-central Minnesota over a wide range of conditions, including high turbidity and CDOM. At Lake Tai (Taihu), China, Jiao et al. (2006) collected water reflectance spectra between June and August of 2004 using a field spectroradiometer and achieved highest accuracy of *Chl-a* estimation with the ratio of reflectance at 719 nm to that at 670 nm ($R^2 = 0.868$).

Improved NIR-red algorithms include three bands rather than two. Dall'Olmo et al. (2003) tested the applicability of a three-band algorithm, initially developed for terrestrial applications (Gitelson et al., 2005; 2003), to retrieve *Chl-a* concentration from reflectance spectra of productive waters.

The three band algorithm uses three spectral regions; a first where reflectance is maximally sensitive to the absorption by *Chl-a*, a second where reflectance is minimally sensitive to *Chl-a*, and a third minimally affected by the absorption of *Chl-a*.

Dall'Olmo et al. (2003) accurately predicted *Chl-a* in five lakes and two reservoirs in Nebraska (USA) by using spectral reflectance measurements around 670, 720 and 750 nm which yielded a significant correlation ($R^2 = 0.94$) with *Chl-a* measurements. Gitelson et al. (2008) further evaluated the potential of this three band model for application to MERIS. Using the following MERIS spectral bands, 660 – 670 nm, 703.75 – 713.75 nm, and 750 − 757.5 nm, they calibrated and validated the algorithm with measurements from turbid waters and found a strong correlation between *Chl-a* measurements and estimations ($R^2 > 0.96$).

Moreover, reflectance ratios acquired in the following spectral regions; blue and green, green and red and blue and red, were also used to estimate *Chl-a* concentration in inland waters from various sensors. Rodríguez et al. (2014) used reflectance in bands 1 and 2 of the Landsat TM to study the temporal evolution of *Chl-a* concentration in Lake Arreo (Spain) between 2000 and 2012. Using these bands, they obtained a good correlation between measurements and estimations of *Chl-a* concentration with a Pearson correlation coefficient of 0.82. Mancino et al. (2009) used multiple regression to develop a model based on the reflectance in several TM band ratios. They selected a model with the ratios of reflectance at band 3 to that at band 2, band 1 to that at band 2 and band 2 to that at band 1 to detect *Chl-a* in the Monticchio lakes in Southern Italy on May of 2001. A strong relationship was found between spectral data in TM bands and *Chl-a* concentration ($R^2 \sim 0.72$). In a study over 15 Minnesota lakes, Brezonik et al. (2005) found that the best

relationship for *Chl-a* retrieval from Landsat 5 TM in September of 2000 was a combination of bands 1, 2 or 4 with the ratio of band 1 to that of band 3 ($R^2 = 0.88$).

Global monitoring of algal blooms in lakes using high resolution satellites (MERIS, MODIS) has been successful (Wynne & Stumpf, 2015). However, the monitoring of small to medium size lakes requires systems with better spatial resolutions. Recent efforts in remote sensing of *Chl-a* in inland waters has been focused on testing or developing algorithms for the high spatial resolution sensors onboard Landsat 8 (OLI) and the most recent Sentinel-2 (MSI).

Recent publications have attempted algorithm development for Landsat 8 or they demonstrated its applicability for monitoring *Chl-a* concentration in lakes and reservoirs. Ha et al. (2017) found that the GrB_2 empirical algorithm consisting of the ratio of OLI band 3 versus band 4 was the most accurate for *Chl-a* estimation at West Lake and nine other hypertrophic lakes in Hanoi (Vietnam) ($R^2 = 0.82$). Fadel et al. (2016), aimed at examining the accuracy of Landsat 8 OLI for estimating *Chl-a* with a wide range of concentrations at eutrophic Karaoun Reservoir in Lebanon. After testing several single bands and band combinations, the best correlation with *in situ* measurements was found when using the ratio of OLI band 2 to band 4 multiplied by band 5 ($R^2 = 0.72$). Li et al. (2018) used OLI data between 2013 and 2015 to calibrate and validate an empirical algorithm to investigate the spatial and temporal patterns and the affecting factors of *Chl-a* concentration at the Xin'anjiang Reservoir in China. The selected algorithm yielding the lowest discrepancies (*RMSE* $= 1.10\ \mu g\ L^{-1}$; *MAPE* $= 14.05\%$) between estimations and *in situ* measurements included the ratio of OLI (band 3 + band 5) over band 2.

Phytoplankton communities are dynamic and therefore *Chl-a* concentration might vary on the scale of days due to wind and hydrodynamics among other variables (Hunter et al., 2008; Stumpf et al., 2016). Hence, with a 16-day temporal resolution, Landsat 8 OLI can be less useful for monitoring frequent changes in *Chl-a* concentration and spatial distribution. However, the Landsat program remains the most important for developing long-term time series of *Chl-a* concentration.

The Sentinel-2 MSI has an advantage over OLI due to its short revisit period of 5 days and a finer spectral resolution, in particular in the NIR, thus allowing a regular monitoring of *Chl-a*. Although initially developed for terrestrial applications, the potential of MSI bands for *Chl-a* estimation in inland waters has been tested in a few studies. Molkov et al. (2019) evaluated the performance of the three-band algorithm, the two-band algorithm, the peak height algorithm and the Normalized Difference Chlorophyll Index for retrieving *Chl-a* concentration in the eutrophic Gorky Reservoir. Grendaitė et al. (2018) developed an empirical algorithm and tested several algorithms for *Chl-a* retrieval over four lakes in Lithuania of which empirical and semi-empirical. Toming et al. (2016) detected *Chl-a* in 11 lakes in Estonia with well-established band ratio algorithms that have performed well with other sensors. Chen et al. (2017) developed an empirical *Chl-a* algorithm using the ratio of MSI band 5 over band 4. The Sentinel-2 MSI holds a great potential for inland water quality monitoring yet more validation studies are needed.

Currently, the spectral, spatial and temporal characteristics of the Sentinel-2 MSI make it the most suitable for detecting *Chl-a* concentrations in small to medium size lakes and reservoirs. Thus the need to develop algorithms or validate previously published algorithms is required for an accurate retrieval of *Chl-a* concentrations. However, despite recent advances in the remote sensing field, collecting data on a wider depth scale is still a limitation. In this case, complementary approaches are used in synergy with remote sensing tools. Such approaches include the use of modeling techniques over different dimensions. Numerical hydrodynamic and ecological models require a considerable amount of *in situ* data and are used for studying lake or reservoir processes spatially and temporally on a highly detailed level (e.g. 3D). Which is why combining both remote sensing and modeling tools has been the focus of recent efforts (*e.g.* Nouchi et al., 2019).

1.3.   Hydrodynamic-ecological modeling of lakes and reservoirs
1.3.1.   *Hydrodynamic modeling*
Numerical models have been applied as an effective tool to understand physical, biological and chemical processes in surface freshwaters (Fenocchi et al., 2019; Leon et al., 2011; Toffolon et al., 2014). Models are valuable for lake and reservoir water quality studies. On one hand they can be used to understand ecosystem physical and ecological processes in response to environmental factors. On the other hand, they can serve as a management tool and to forecast water quality in view of possible future climate change scenarios.

Several 1D and 3D hydrodynamic models, coupled to ecological models, have been developed for the study of lake ecosystems. The choice of the spatial dimension of the model should usually depend on the objectives of the study or the questions being addressed and the characteristics of the ecosystem. 1D vertical models with a horizontally averaged output have been frequently used in lake ecosystem studies (Hodges 2009). They require a small computational effort and less input data and are thus considered for long term applications or future projections. However, the need for 3D hydrodynamic models has been recognized in order to accurately capture the physical processes (e.g. vertical and horizontal mixing) (Soulignac et al., 2018).

The application of hydrodynamic models to inland water bodies has been widely used to understand their ecological status (Fadel et al., 2017; Pinardi et al., 2015; Soulignac et al., 2018). Reservoirs exhibit different physical and water quality characteristics from natural lakes (Doubek & Carey, 2017). The river can influence the reservoir water level but also the circulation pattern, and hence strongly impacts the ecosystem responses, while for natural lakes the impact of a stream flow is generally limited (Tufford & McKellar, 1999).

Compared to large lakes and reservoirs, the application of 3D hydrodynamic models to medium and small-size reservoirs with considerable water level fluctuations is seldom seen, especially in semi-arid climates. Reservoir physical dynamics drives the distribution and transport of water quality variables in particular physical mixing or wind induced circulation (Falconer et al., 1991).

The latter can influence chemical and biological properties in particular the distribution of harmful algal blooms and their shoreline accumulation. Water quality is also influenced by thermal stratification acting as a barrier in the warm season and controlling the distribution of nutrients, heat and dissolved substances in the water column.

Prior knowledge about water temperature and currents is crucial for assessing the water quality of reservoir. Several 3D hydrodynamic modeling studies were undertaken in order to understand the hydrodynamics and the thermal regime of reservoirs (*e.g.* Chanudet et al., 2012). In the tropical Itumbiara reservoir in Brazil (814 km^2), an investigation of surface circulation and thermal structure was conducted using the 3D Estuary and Lake Computer Model ELCOM (Curtarelli et al., 2014). The results showed that the surface circulation was mainly wind-driven and that the thermal structure was influenced by several meteorological variables and the river inflow.

In other studies, 3D hydrodynamic and water quality or ecological models were jointly applied for identifying key factors affecting the water quality of reservoirs. They highlighted the importance of 3D hydrodynamic models for capturing temporal and spatial distributions of biogeochemical variables (Romero et al., 2004). For example, describing the transport and dynamics of algal blooms (Mao et al., 2015) and contaminants (Xu et al., 2017) under the influence of hydrodynamics.

1.3.2. Ecological modeling

In the last several decades, the rise in the number of eutrophic lakes and reservoirs affected by harmful algal blooms has led to the use of ecological models for research purposes such as understanding ecological processes in response to hydrodynamics and climate change as well as a predictive tool to support lake management. Most recently, modeling cyanobacteria in aquatic ecosystems has become the subject of several studies due to their negative impacts on water quality and their ability to induce human health risks.

Several ecological models, most of which are mechanistic and dynamic, have been developed to study lake and reservoir eutrophication in combination with 3D hydrodynamic models (Anagnostou et al., 2017). These models usually integrate chemical, physical and biological processes. In a recent review by Vinçon-Leite & Casenave (2019), the application of ecological models has been shown to often prevail across lakes in the United States and Asia with a large surface area. Reservoirs on the other hand received less attention.

In the largest reservoir in Western Europe, the Alqueva (250 km^2), located in a semi-arid region of Portugal, a coupled hydrodynamic-eutrophication modeling approach was used to simulate flow, temperature and water quality in order to explain the existence of distinct ecological regions in the reservoir. This spatial and temporal variability was attributed to particular hydrological and geomorphological characteristics in addition to local climate features (Lindim et al., 2011).

Deus et al. (2013) applied a coupled 3D hydrodynamic water quality model to the Tucuruí reservoir in Brazil (2430 km^2) to understand the interactions between hydrodynamics, internal nutrient loads

and phytoplankton growth. The results indicated that phytoplankton growth was limited by hydrodynamics due to different nutrient loading along the year in low and high rainfall periods.

According to the same review, owing to the extensive and accurate description of physical processes, hydrodynamic models generally provide rather accurate outcomes. They do not require much calibration and can be transferred between different study sites. The parameterization of ecological models on the other hand is challenging. Most of the complex biological processes are simplified, a large number of model parameters usually require site-specific calibration, the computational time is long and the demand of *in situ* data is usually high. Thus, in case of limited data sets available for the parameter calibration, the uncertainties can be large. However, they remain the most appropriate for representing ecosystem processes on a spatial and temporal scale especially for phytoplankton growth.

For a comprehensive overview of phytoplankton dynamics, 3D models are required to simulate the transport and behavior of phytoplankton in response to several factors such as temperature, nutrients and irradiance. Several coupled 3D hydrodynamic-ecological models have been used to simulate thermal stratification, phytoplankton biomass including cyanobacteria, nutrients and dissolved oxygen (DO) in lakes. However, in comparison to 1D models, the application of 3D hydrodynamic-ecological models to lake ecosystems have been recently increasing and is still limited for reservoirs with large water level fluctuations. Hence, more validation studies of 3D hydrodynamic-ecological modeling are needed.

1.4. Coupling *in situ* measurements, satellite remote sensing and modeling techniques

The coupling of hydrodynamic-ecological models and satellite remote sensing data is advancing in the field of limnology (Nouchi et al., 2019). Synoptic *in situ* data acquisition and the examination of its horizontal variability within a short period of time through traditional field monitoring is difficult and expensive. With current research in the remote sensing field, it has become possible to enhance data acquisition. The recent launch of Sentinel-2 satellites provides a greater coverage of water constituents with an increased spatial (10 m) and temporal resolution (5 days) suitable for the calibration/validation of models and the monitoring of small lakes and reservoirs (section 1.2). However, the development and validation of remote sensing algorithms of Sentinel-2 is still required for accurate data assimilation to model applications. Owing to the lack of thermal channels in Sentinel-2 satellites, the TIRS onboard Landsat 8, with an appropriate atmospheric correction algorithm, is a valuable tool for small lakes and reservoirs, providing regular thermal data each 16 days.

Because of the difficulties in conventional monitoring methods, most model validation efforts are restricted to a few observation points. Remote sensing can overcome limitations imposed by this type of monitoring and thus provide synoptic data suitable for a thorough calibration or validation

of models. For instance, Allan et al. (2016) used surface temperature data acquired from Landsat thermal imagery to validate a 3D hydrodynamic model of Lake Rotoehu. Yet, using remote sensing data for model calibration or validation is still uncommon for lakes and reservoirs.

Furthermore, remote sensing data can be used as initial data for 3D models. For example, Curtarelli et al. (2015) used remote sensing and 3D hydrodynamic modeling to represent phytoplankton dynamics at the Itumbiara Hydroelectric Reservoir in Brazil. They used remote sensing data to force the hydrodynamic model (generate time series of river inflow temperature) and to investigate the horizontal distribution of phytoplankton.

However, remote sensing does not provide information over the entire vertical domain of the ecosystem. For instance, remote sensing estimations such as water surface temperature and *Chl-a* concentration are limited to the top 100 μm and to the Secchi depth respectively. Therefore, an assimilation of both *in situ* and remote sensing data is required into modeling applications.

Further, remote sensing tools do not offer an explanation for the spatial distribution of water constituents shown in remotely sensed images. In this case, numerical models which cover the entire spatial (vertical and horizontal) and temporal domains can provide means to interpret these images. For example, in a study by Hedger et al. (2002), a coupled 3D computational fluid dynamics-ecological model was used to explain the spatial distribution of *Chl-a* concentration in the remote sensing image of Loch Leven Lake, Scotland. Further, in order to identify the circulation pattern responsible for algal patchiness at Mantua Superior Lake, Italy, Pinardi et al. (2015) used a 3D hydrodynamic model to analyze the distribution of phytoplankton from remote sensing images of *Chl-a*. Soulignac et al. (2018) showed the capability of 3D modeling and remote sensing for understanding the spatio-temporal heterogeneities of phytoplankton in Lake Geneva.

Although the approach of combining *in situ*, remote sensing and model data has been often applied in oceanography, it is still less adopted for lakes and reservoirs. Moreover, even when this approach is applied to lakes and reservoirs, the comparison between model simulations and remote sensing data is still qualitative and not quantitative.

1.5. Previous modeling and remote sensing studies in Karaoun reservoir

Until recently, Karaoun Reservoir was never the subject of modeling and remote sensing studies. With the consistent rise of cyanobacterial bloom events, one dimensional hydrodynamic-ecological modeling studies were conducted on the reservoir. This required the collection of *in situ* data (water temperature, water samples, transparency, etc.) which was mainly and regularly conducted in 2012 and 2013. Fadel et al. (2017) configured the one dimensional DYRESM-CAEDYM model which was also calibrated and validated. The model was used to simulate the thermal regime and phytoplankton succession (green algae, cyanobacteria and diatoms) at Karaoun Reservoir in 2012 and 2013 with an emphasize on cyanobacteria species (*Chrysosporum ovalisporum* and *Microcystis aeruginosa*; the most dominant at Karaoun Reservoir). Their ultimate

goal was to understand the environmental factors driving cyanobacterial blooms. Karaoun Reservoir was found to be strongly stratified between May and August. Further, an interplay between thermal stratification, water temperature, irradiance, water level fluctuations and nutrients availability was responsible for the changes in the phytoplankton community. The main factor on which the dominance of *Chrysosporum ovalisporum* or *Microcystis aeruginosa* blooms was mostly water temperature. During stratified conditions, *Microcystis aeruginosa* thrives on high temperatures (25 °C) while *Chrysosporum ovalisporum* dominates at temperatures lower than 23 °C (Fadel et al., 2015).

This work provided new insight about the succession of phytoplankton species and their drivers on a one dimensional level. Yet, a complete understanding of the reservoir functioning and ultimately optimal management strategies would benefit from the use of 3D models. Recent studies by Fadel et al (2016) and Sharaf et al (2019a) were conducted to derive *PC* and *Chl-a* concentrations at Karaoun Reservoir using satellite data from Landsat images. In this case, *Chl-a* and *PC* are considered indicators of phytoplankton biomass with *PC* being specific to cyanobacteria. The images revealed a heterogeneous spatial distribution of these pigments over different periods of times. This spatial distribution and its drivers cannot be explained using one dimensional models thus the need for 3D models. To our knowledge, 3D hydrodynamic-ecological modeling approaches are not yet applied to study the ecological functioning of the reservoir.

2. Chapter 2: Materials and Methods

In this chapter the study site is firstly described, Karaoun Reservoir in Lebanon (section 2.1). Then the methods used in collecting *in situ* measurements and the laboratory analysis are presented. Data in 2012 and 2013 were available from previous efforts whereas data in 2017 and 2018 were collected in the context of the PhD (section 2.2). Further, the methodology adopted for the calibration and/or validation of remote sensing algorithms for estimating water surface temperature (section 2.3), *Chl-a* concentration (section 2.4) and transparency (section 2.5) is described. Finally, the coupled 3D hydrodynamic-ecological model is presented. It was used to simulate the thermal regime and ecological processes at the study site including its configuration and calibration.

2.1. Study site

The largest freshwater body in Lebanon, Karaoun Reservoir (Figure 6-8, 33°34'N, 35°41'E), is relatively deep, monomictic, eutrophic and belongs to the few regularly monitored lakes and reservoirs of the Middle East. It has a surface area of 12 km^2 at full capacity (859 m above sea level, 224 10^6 m^3), maximum and mean depths of 60 and 19 m, respectively, and an average residence time of 0.77 months. Karaoun Reservoir is refilled annually by inflow from the Litani River, both managed by the Litani River Authority (LRA). Inflows can also be caused by spring discharges. The climate is semi-arid with cold winters and hot summers. Karaoun Reservoir serves different purposes such as recreation, fishing, power generation and irrigation leading to large fluctuations in its water level, ~ 25 m in a year (Fadel et al., 2017) (chapter 3) also influenced by the hydrological cycle. These cause considerable variations in the water surface temperature and in the stratification pattern. During the dry season, the reservoir stratifies between May and August. The thermal stratification is then broken down usually from late September and onwards as a result of vertical mixing due to air cooling and higher inflows. Since 2012, regular *in situ* monitoring revealed the breakdown of the water quality of Karaoun Reservoir including high nutrient concentrations and persistent events of toxic cyanobacterial blooms including *Microcystis aeruginosa* and *Chrysosporum ovalisporum* which were first reported in 2009. The sources of these high nutrient concentrations along the Litani River and its tributaries include industrial, agricultural and domestic sewage discharges with very deficient sanitation and sewage treatment (Fadel et al., 2015; 2014). Currently, the reservoir is only being used for hydropower production which causes large decrease in the water level during the dry season. Regular monitoring of the physical and ecological state of the reservoir is crucial for establishing optimal management strategies especially that it might be designated to ensure drinking water to Beirut, the capital of Lebanon.
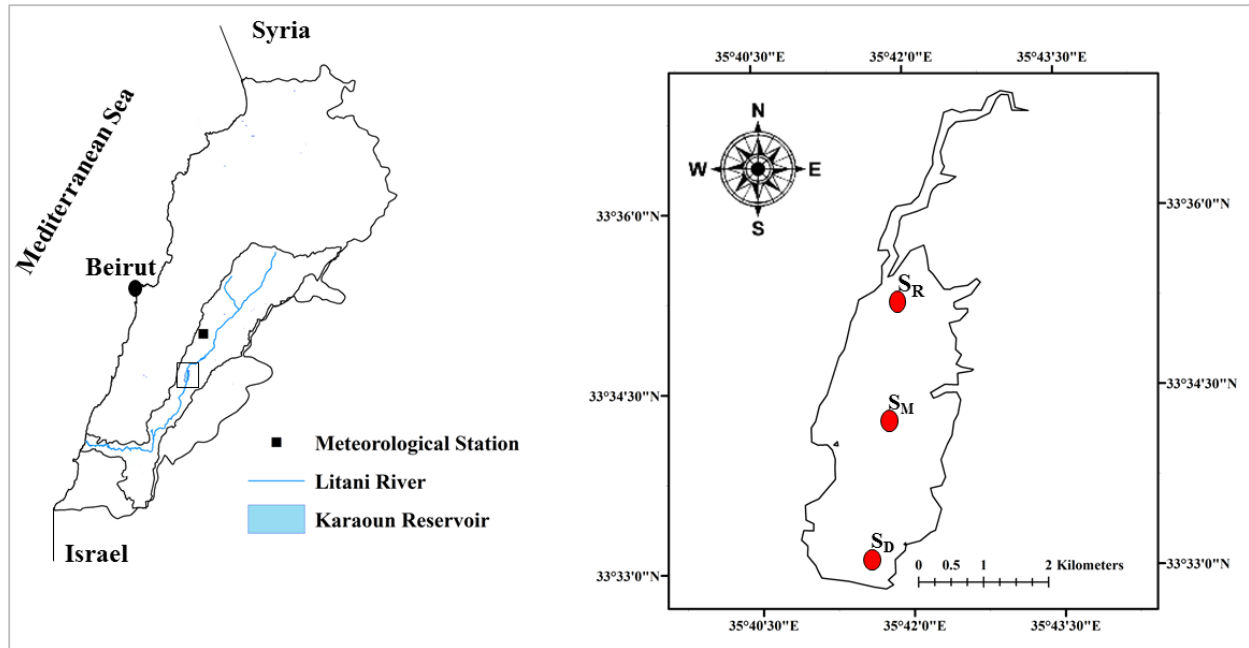
Figure 6: Study site: Karaoun Reservoir, Lebanon. The red dots represent the sampling sites.

Figure 7: Study site: Karaoun Reservoir, Lebanon (Credit: Litani River Authority).

Figure 8: Spillway at Karaoun Reservoir, Lebanon (www.litani.gov.lb).

2.2. Data collection

Field campaigns had been organized in 2012, 2013 (Fadel et al., 2017). New campaigns were undertaken in 2017 and 2018. *In situ* biological, physical and chemical data were collected on a monthly basis, mostly between late spring and early autumn, a period where Karaoun Reservoir experiences blooms of cyanobacteria. The periods during which field campaigns were conducted are shown in Table 4. Sampling sites consisted of a point near the Litani River inlet (S_R), a point at the center of the reservoir (S_M) and a point near the dam (S_D) with additional points occasionally (Figure 6).

Table 4: Start and end dates for the period of data collection at Karaoun Reservoir in 2012, 2013, 2017 and 2018.

Year	Start Date	End Date
2012	01 July	20 November
2013	14 May	21 August
2017	12 May	18 September
2018	29 May	03 October

Table 5: Dates of field campaigns in 2012, 2013, 2017 and 2018.

Year			
2012	**2013**	**2017**	**2018**
	14 May	12 May	29 May
	30 May	31 May	
	20 June	30 June	20 June
01 July	08 July	27 July	20 July
	30 July		
14 August	21 August		14 August
28 August			
12 September		18 September	
01 October			
16 October			
07 November			
20 November			

2.2.1. Meteorological and hydrological data

Daily hydrological data consisting of inflow and outflow rates and water level measurements were collected from the Litani River Authority in 2012 and 2017. In 2018, the outflow rate was calculated from water level measurements and monthly inflow rates were available. The water level is measured visually on a scale on the side of the cylindrical spillway (S_D). The outflow rates are measured in the hydropower plant and in the pumping station of the irrigation canal (the overflow through the spillway is not monitored but it does not occur during the study periods between spring and fall). Inflows are reconstructed from the water level and outflow rates, neglecting evaporation.

Meteorological data (shortwave solar radiation, wind speed and direction, relative humidity, air temperature and rainfall) were available from the Tal Amara station located in the Bekaa valley 40 km north of Karaoun Reservoir (Figure 6) and provided by the Lebanese Agricultural Research Institute (LARI). Data were available and used on a daily time step in 2012 and at an hourly time step in 2017 and 2018. The cloud cover, very low during the summer season in Karaoun catchment, was neglected. Meteorological and hydrological data (water level, inflow and outflow rates) were used as input to the hydrodynamic model. Water level measurements were used as initial conditions.

2.2.2. In situ measurements

2.2.2.1. Sampling

Water samples were collected at the three monitoring sites S_R, S_M and S_D (Figure 6) under the surface (~0.5 m) and at 5 and 10 m depths for further nutrients and *Chl-a* analysis and phytoplankton identification. The samples were collected using a sampling bottle (Niskin, 2.2 L).

2.2.2.2. Temperature

Water temperature measurements were performed hourly in 2012, 2013, 2017 and 2018 using thermistor chains (Starmon sensors in 2012, lost and replaced by HOBO sensors in 2017 and 2018, with 0.05 and 0.53°C accuracy respectively) at monitoring sites S_R, S_M and S_D. Measurements were recorded at different depths (0.2, 1, 4, 5, 7, 10, 13, 15 and 16 m) between the subsurface and 16 m. In 2016, water temperature was only recorded at the subsurface (0.5 m depth).

2.2.2.3. Water transparency

Transparency or Secchi depth measurements were recorded using a black and white Secchi disk in 2012, 2013, 2017 and 2018. Measurements were recorded at monitoring sites S_R, S_M and S_D as well as additional locations around the reservoir.

2.2.2.4. PC

In 2012, 2013, 2017 and 2018, *PC*, a characteristic pigment of cyanobacteria, was measured at different depths using the micoFlu-blue probe (Trios optical sensors) making use of fluorescent excitation. It has an excitation peak at 620 nm and reads the fluorescence emitted between 650 and 660 nm. It provides *PC* concentration with a measuring range between 0 and 200 μg/L and an accuracy of 0.02 μg/L. The probe has been used in several published studies, in which the obtained *PC* concentrations correlated strongly against the number of cyanobacterial cells (Brient et al., 2008) and biovolumes (Bastien et al., 2011).

Concentrations of *PC* were converted into *Chl-a* by establishing a correlation between available measurements of *PC* and *Chl-a*. A factor of 1.33 was used for the 2012 data (Fadel et al., 2017) and a factor of 1.09 for the 2017 data.

2.2.3. Laboratory analysis

2.2.3.1. Phytoplankton microscopic identification

Phytoplankton species were determined according to taxonomic keys based on cell structure and dimensions, colony morphology, and mucilage characteristics (Komárek and Anagnostidis, 1999, 2005). Microscopic identification and enumeration were carried out under a phase contrast microscope (Nikon TE200, Nikon, Melville, NY, USA) under a ×40 objective and using Nageotte chamber that accepts 100 μL on 40 bands. Each sample was counted on triplicate. The mean biovolume of each phytoplankton species was calculated in mm^3 based on its cell shape according to Sun & Liu (2003). This work was conducted by Doctor Ali Fadel in 2012 and 2013 and by Professor Kamal Slim in 2017 and 2018.

2.2.3.2. Chl-a

Chlorophyll-a concentrations were quantified in 2018. Water samples were filtered using GF/C filters (2 to 3 hours after sampling), frozen at -20 °C, vortexed with 100% ethanol (Yéprémian et al., 2016) and then centrifuged. Concentration was finally determined by spectrophotometry (Appendix B: *Chl-a* extraction and determination protocol).

2.2.3.3.   Nutrients

Samples used for the analysis of nutrients; total nitrogen, total phosphorus, nitrate (NO_3^-) and orthophosphate (PO_4^{3-}) were collected in 2013 and 2018.

Samples of NO_3^- and PO_4^{3-} were filtered through a 0.45 µm cellulose acetate filter. The concentrations of NO_3^- were then estimated by colorimetry with a photometer (Palintest Photometer 7000se, Gateshead, England).

The concentrations of PO_4^{3-} were determined at 880 nm on a UV/visible spectrophotometer using the colorimetric ascorbic acid method.

The protocols for NO_3^- and PO_4^{3-} analysis can be found in Appendix C: Nitrate and phosphate analysis

2.3.   Remote sensing of water surface temperature

In this section, a description is presented for the algorithms and their application for retrieving water surface temperature, the acquisition of data and the statistical indicators used for the evaluation of algorithms performance.

2.3.1.   The radiative transfer equation

For a single infrared thermal band, the at-sensor radiance can be approximated based on the radiative transfer equation (RTE) according to the following expression (Barsi et al., 2003):

$$L_{Sen} = \tau \left[\varepsilon L_\lambda(T_{RTE}) + (1 - \varepsilon)L_d \right] + L_u \qquad 1$$

where L_{Sen} (in W m^{-2} sr^{-1} µm^1) is the radiance measured by the TIRS (or Top Of Atmosphere radiance), τ is the atmospheric transmissivity, ε is the emissivity of water, $L_\lambda(T_{RTE})$ represents Planck's function of a blackbody at surface temperature T_{RTE}, L_d is the downwelling atmospheric radiance and L_u is the upwelling atmospheric radiance.

Surface temperature (T_{RTE}) can be then calculated from (2) as follows (Figure 9):

$$T_{RTE} = \frac{K_2}{ln\left(\frac{K_1}{L_\lambda(T_{RTE})}+1\right)} \qquad 2$$

where (T_{RTE}) is the surface temperature in Kelvin, K_1 and K_2 are calibration parameters for TIRS Band 10, their values are 774.8853 W m^{-2} sr^{-1} µm^{-1} and 1321.0789 K respectively. T_{RTE} hereafter designates surface temperature retrieved from the RTE.

Using the TIRS Band 10, García-Santos et al. (2018) found a *RMSE* of 2.3 K with the RTE. Furthermore, Yu et al. (2014) used the RTE for retrieving land surface temperature at four study sites in the United States and found that the *RMSE* between estimated and ground temperature

measurements was much higher with TIRS Band 11 (1.17 K, 1.19 K, 1.12 K and 0.75 K) than with TIRS Band 10 (0.87 K, 1.01 K, 0.93 K and 0.57 K).
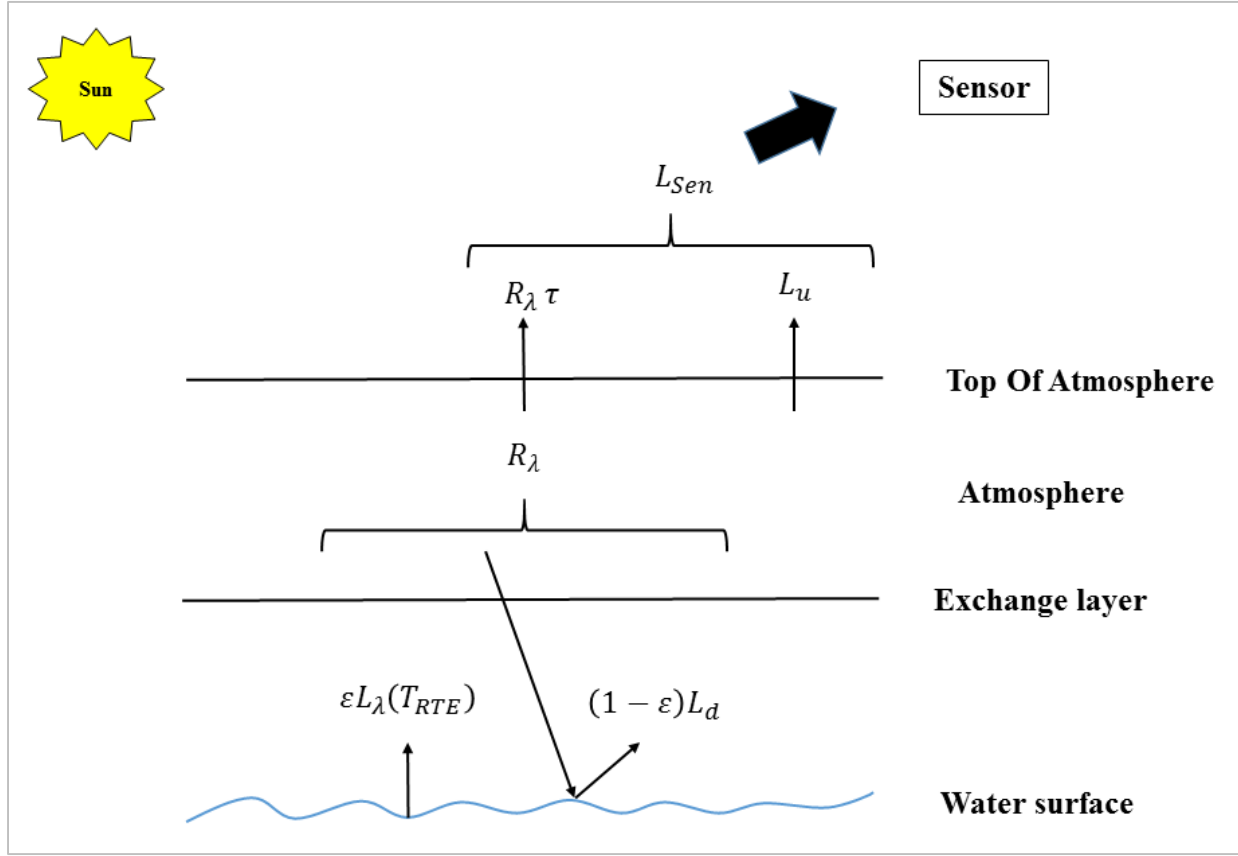
Figure 9: Surface temperature retrieval from the radiative transfer equation. R_λ is radiance observed at ground level.

2.3.2. *The general single channel algorithm*

The general SC1 algorithm for retrieving surface temperature was initially proposed in Jiménez Muñoz & Sobrino (2003). The algorithm aims at retrieving surface temperature in a more operational way than using the radiative transfer equation. It depends only on water vapor w and emissivity ε as input (Figure 10). Hence, it avoids dependence on atmospheric parameters such as atmospheric transmissivity τ and upwelling and downwelling atmospheric radiances L_u and L_d which are rarely available and somewhat difficult to measure.

The SC1 algorithm retrieves surface temperature (T_{SC1} in K) using the following general equation:

$$T_{SC1} = \gamma(\varepsilon^{-1}(\Psi_1 L_{Sen} + \Psi_2) + \Psi_3) + \delta \qquad 3$$

where γ and δ are expressed as:

$$\gamma \approx \frac{T_{Sen}^2}{b_\lambda \times L_{Sen}}; \quad \delta \approx T_{sen} - \frac{T_{Sen}^2}{b_\lambda} \qquad\qquad 4$$

where T_{Sen} is the at-sensor brightness temperature in K, b_λ is equal to 1324 K for Landsat 8 TIRS Band 10, 1290 K for Landsat 4 Band 6 and 1256 K for Landsat 5 Band 6 and Ψ_1, Ψ_2, Ψ_3 are the atmospheric functions.

The concept of the SC1 algorithm aims at the approximation of the atmospheric functions presented in (3) versus the water vapor content (w in g cm^{-2}) through a polynomial fit. In a matrix notation, this approximation can be expressed as follows, where the coefficients C_{ij} (Appendix A) are obtained by simulation from the sensor filter response:

$$\begin{bmatrix} \Psi_1 \\ \Psi_2 \\ \Psi_3 \end{bmatrix} = \begin{bmatrix} C_{11} & C_{12} & C_{13} \\ C_{21} & C_{22} & C_{23} \\ C_{31} & C_{32} & C_{33} \end{bmatrix} \begin{bmatrix} w^2 \\ w \\ 1 \end{bmatrix} \qquad\qquad 5$$

A particular set of coefficients linking transmissivity and radiances to the water vapor content was derived from the filter response of Landsat 5 TM. This algorithm was further revised by Jiménez-Muñoz et al. (2009) and sets of coefficients were proposed for Landsat 4 and 7. Eventually new sets of coefficients for Landsat 8 TIRS were provided by Jiménez-Muñoz et al. (2014). Ψ_1, Ψ_2, Ψ_3 are the atmospheric functions given by:

$$\Psi_1 = \frac{1}{\tau}; \quad \Psi_2 = -L_d - \frac{L_u}{\tau}; \quad \Psi_3 = L_d \qquad\qquad 6$$

Recently, Cristóbal et al. (2018) further introduced air temperature to the algorithm together with water vapor content (w) as it is supposed to improve to the algorithm performance (Figure 10). The atmospheric functions are then fitted with a second degree polynomial based on water vapor content (w) and near surface air temperature (T_0) in K as follows:

$$\Psi_n = iw^2 + hT_0^2 + gw + fT_0 + eT_0^2 w + dT_0 w + cT_0 w^2 + bT_0^2 w^2 + a \qquad\qquad 7$$

where $n = 1,2,3$ and $a, b, c, d, e, f, g, h, i$ are the numerical coefficients of the statistical fit (Appendix A). In this case surface temperature (T_{SC2}) is retrieved from (3).

Within the general SC1 algorithm, the approximations of the atmospheric functions differ for Landsat 4, 5 and 8 and each case is assigned a different set of coefficients (Appendix A). For a complete description, readers can refer to Jiménez-Muñoz et al. (2009, 2014). The SC1 algorithm was implemented as follow: γ and δ were calculated from (4), the atmospheric functions Ψ_1, Ψ_2 and Ψ_3 were obtained from (5) after selection of appropriate coefficients for the TM and the TIRS sensors and assigning the corresponding w values. Once all parameters were calculated, surface temperature (T_{SC1}) with atmospheric coefficients calculated from (5) was then retrieved

using (3) with a value of 0.995 for water emissivity. The SC2 algorithm was implemented in the same manner. The atmospheric functions were obtained from (7) after assigning specific coefficients for each. Surface temperature (T_{SC2}) was then retrieved from (3).

The most recent SC2 algorithm developed with water vapor content and air temperature has not been yet validated as extensively as the SC1 approach. It has been shown to yield a *RMSE* of the order of 1 K against *in situ* data (Cristóbal et al., 2018) recorded over an area containing a variety of vegetation and snow in Alaska.

Both the SC1 and SC2 approaches are expected to provide good results. The choice of the method depends on the range of water vapor content. The good performance of the former is still limited to values greater than 3 g cm^{-2}. Hence, errors are expected to increase with the amount and errors associated with the water vapor content. On the contrary, the SC2 approach shows a superior performance in a wide range of water vapor content and air temperature.
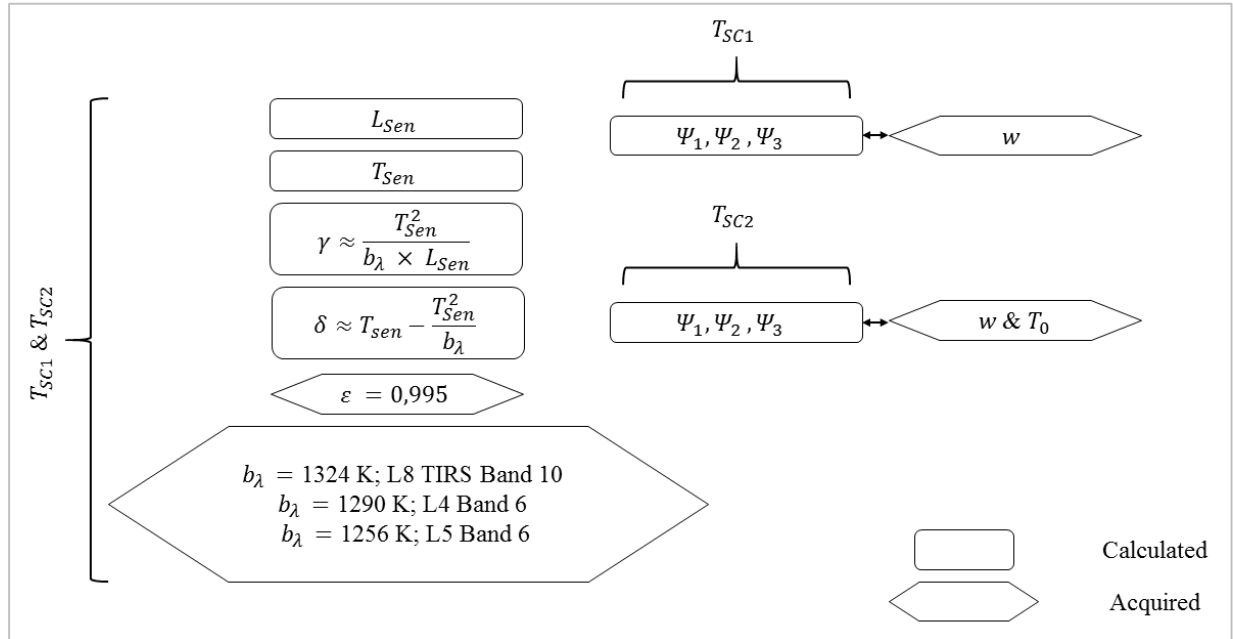
Figure 10: Flowchart of variables involved in the single channel algorithm (SC1) and its improved version (SC2).

2.3.3. *The mono-window algorithm*

The mono-window (MW) algorithm, initially developed by Qin et al. (2001) and widely used for surface temperature retrieval from Landsat TM and ETM^{+} single thermal bands, depends on emissivity, atmospheric transmissivity and effective mean atmospheric temperature (Figure 11). Wang et al. (2015) further improved the algorithm for surface temperature retrieval from Landsat 8 TIRS Band 10 by including local meteorological data for estimating the effective mean atmospheric temperature.

Surface temperature can be retrieved from the MW algorithm in the following form:

$$T_{MW} = [a_{10}(1 - C_{10} - D_{10}) + (b_{10}(1 - C_{10} - D_{10}) + C_{10} + D_{10})T_{Sen} - D_{10}T_a]/C_{10} \qquad 8$$

where T_{MW} is the surface temperature retrieved from Band 10 of the TIRS, a_{10} and b_{10} are constants used to approximate the derivative of the Planck radiance function for the TIRS Band 10 and depend on the range of T_{Sen} (here a_{10} = - 62.7182 and b_{10} = 0.4339), T_a is the effective mean atmospheric temperature in K and C_{10} and D_{10} are the internal parameters for the algorithm:

$$C_{10} = \tau\varepsilon \qquad 9$$

$$D_{10} = (1 - \tau)[1 + (1 - \varepsilon)\tau] \qquad 10$$

As before, τ and ε are respectively atmospheric transmissivity derived from the TIRS Band 10 spectral response curve and water emissivity.

The effective mean atmospheric temperature is approximated from the near surface air temperature T_0 (from a ground meteorological station) from the following linear relation for an atmosphere of mid-latitude summer (Wang et al., 2015):

$$T_a = 16.0110 + 0.9262\,T_0 \qquad 11$$

The MW algorithm was shown to provide lower discrepancies than the SC1 algorithm, with *RMSE*s of 0.84 K and 1.05 K respectively using TIRS Band 10 (Wang et al., 2015). Yet, Sobrino et al. (2004) compared the MW and SC1 approaches using thermal data from the TM Band 6 and found that the SC1 algorithm yielded less errors than the MW algorithm with root mean square deviations of 1 K and 2 K respectively.
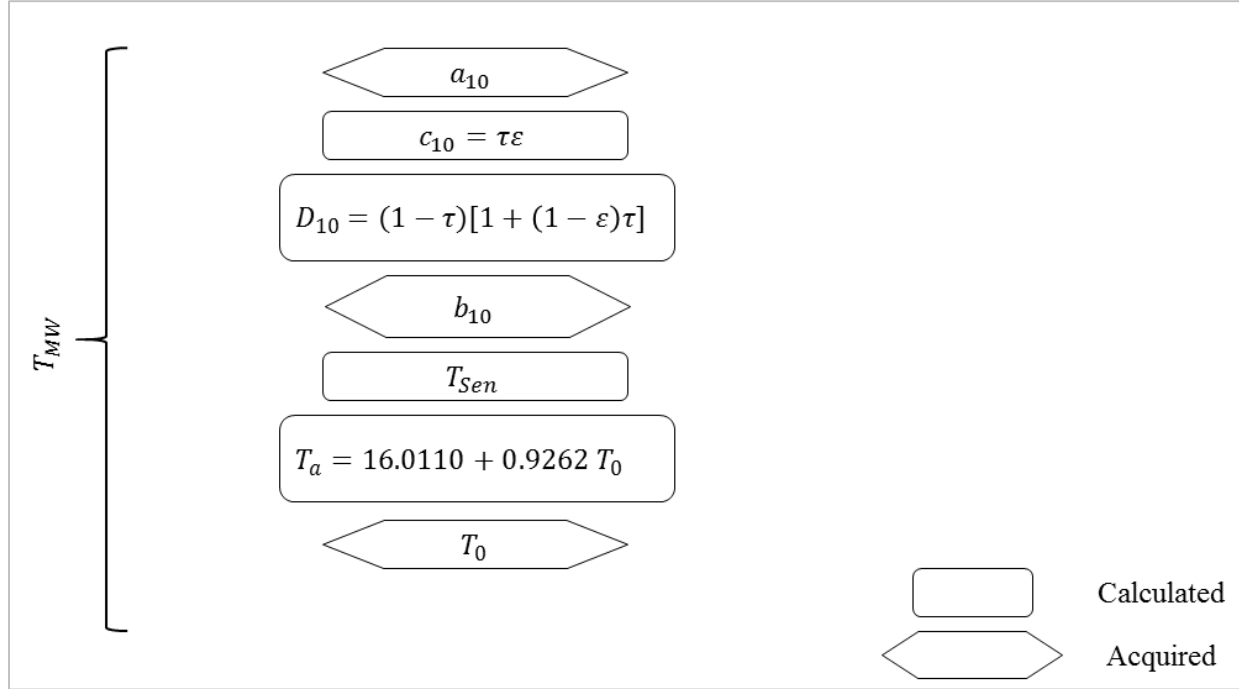
Figure 11: Flowchart of variables implicated in the mono-window algorithm.

2.3.4. Data collection and processing

Nineteen cloud free Landsat 8 scenes corresponding to a total of 31 water surface temperature observations ($T_{in\ situ}$) were acquired every 16 days (at 11:10 am local time) from May 15 to October 16, 2016 and from 26 April to September 1, 2017. Due to variations in the water level, the surface of the reservoir was extracted for each scene, using the normalized difference water index (McFeeters, 1996) which makes use of reflectance in the near-infrared and green parts of the spectrum. All pixels crossing the reservoir shoreline were not considered.

Continuous *in situ* water surface temperature data were available for both years at three monitoring sites and were extracted at the time of satellite overpasses. Details about the acquisition of measurements can be found in chapter 2 (section 2.2.2.2). In the literature, the bulk surface temperatures which are used to assess satellite inferred observations are usually measured over depths ranging from a few centimeters to several meters (Schmidt et al., 2018).

In addition to 2016-2017 images, 153 images from the Landsat 4 and 5 TM and Landsat 8 TIRS sensors were used to characterize the evolution of water surface temperature between 1984-2015 and 2018, whereas no *in situ* water temperature records were available for this period. Thermal infrared data were freely downloaded from the United States Geological Survey[2]. Images were converted from digital numbers to at-sensor radiance L_{sen} and at-sensor brightness temperature

---

[2] https://www.usgs.gov/

T_{sen} by means of the ENVI software (version 5.2) using calibration parameters from the metadata file. Maps of water surface temperature were generated using the ArcGIS software (version 10.3) .

For the RTE and the MW algorithms, atmospheric parameters (τ, L_u and L_d) were computed with the Atmospheric Correction Parameter Calculator of the National Center for Environmental Prediction (NCEP) (Barsi et al., 2005; 2003) using the Landsat 8 TIRS Band 10 spectral response curve. This atmospheric correction tool uses the NCEP modeled atmospheric global profiles and the MODTRAN (MODerate resolution atmospheric TRANsmission) radiative transfer code. Daily water vapor content was collected for the whole validation period and downloaded from the ERA interim dataset of the European Centre for Medium-Range Weather Forecasts (ECMWF[3]) at 12:00 (Dee et al., 2011). Near surface air temperature T_0 used for both the SC2 and MW algorithms was taken from a meteorological ground station (Tal-Amara meteorological station).

2.4. Remote sensing of *Chl-a*

In this section, Sentinel-2 data are presented and a description of the image pre-processing procedure is provided. Further the algorithm which was applied to derive *Chl-a* concentration at the study site is presented.

2.4.1. Satellite data and pre-processing

Sentinel-2 A and B data were used for the retrieval of *Chl-a* at Karaoun Reservoir. As described in section 1.2.2, Sentinel-2 satellites carry the MultiSpectral instrument (MSI) holding thirteen spectral bands at three different spatial resolutions (10, 20 and 60 m) and covering the visible to the shortwave infrared spectrum (Table 3).

Sentinel-2 level-1C MSI images, which include radiometric and geometric corrections and radiometric measurements in Top Of Atmosphere reflectance, were freely downloaded from the USGS website (https://earthexplorer.usgs.gov) for 2017 and 2018. Images with high cloud cover were not used. The bands of Sentinel-2 MSI have different spatial resolutions (Table 3). Therefore, the Sentinel Application Platform (SNAP) software[4] (version 7.0.3) was used to process the images and resample bands to a 10 m resolution. In order to remove the effect of atmospheric components, an atmospheric correction was performed with the 6S code, Second Simulation of the Satellite Signal in the Solar Spectrum (Vermote et al., 1997), a radiative transfer code for modeling atmospheric scattering effects. It requires several inputs such as sun zenith and azimuth, type of sensor, atmospheric profiles, date of image acquisition, values of the Aerosol Optical Depth (AOD) amongst others. Atmospheric profiles were set as "Midlatitude Summer" while the aerosol model was selected as "Continental". Daily Aerosol Optical Depth values were extracted from the European Centre for Medium-Range Weather Forecasts. The normalized difference water index

---

[3] https://www.ecmwf.int/
[4] http://step.esa.int/main/

(McFeeters, 1996) was used to delineate the surface of the reservoir on each image owing to the variation in the water level. The ArcGIS software was used for generating *Chl-a* maps.

2.4.2. *Chl-a algorithm*

Chl-a concentrations were derived from atmospherically corrected Sentinel-2 images based on a band ratio algorithm (Pinardi et al., 2018). The latter makes use of atmospherically corrected reflectance of Sentinel-2 band 5 over band 4. Band 4 is located in the red region of the spectrum around 665 nm where *Chl-a* absorbs energy. Band 5 is located in the NIR part of the spectrum near 705 nm where reflectance is minimally sensitive to the absorption by *Chl-a*. The algorithm was applied in this work to map *Chl-a* concentrations in 2017 and 2018 at Karaoun Reservoir.

2.5. Remote sensing of transparency

2.5.1. *Data collection and image processing*

Transparency measurements recorded in 2017 and 2018 on several monitoring sites were used to calibrate and validate the algorithm. Measurements (*n*=14) were taken on dates of Sentinel-2 overpasses (Table 6) using a Secchi disk. In 2017 and 2018, overall measurements spanned between 0.5 and 1.6 m. The calibration and validation subsets were divided into 7 points each. Sentinel-2 images were processed according to section 2.4.1. The ArcGIS software was used for generating transparency maps.

2.5.2. *Algorithm development*

An empirical band ratio algorithm was developed to derive transparency (or Secchi depth) at Karaoun Reservoir from Sentinel-2 remote sensing data. A regression approach was used to develop the algorithm based on band reflectance in the visible-NIR spectrum from single bands and band ratios. The coefficient of determination (R^2) and the Root Mean Squared Error (*RMS*E) were used to assess the performance of the predictors for the calibration procedure. The resulting regression equation was further used to retrieve transparency estimations during the validation period which were then compared to measurements.

The acquisition of the transparency from Sentinel-2 images will allow the determination of the depth at which *Chl-a* is being provided. This will serve for comparing *Chl-a* maps from both the 3D model and Sentinel-2 maps. For comparison purposes, 3D simulations of *Chl-a* should be also provided at the same depth as that given by remote sensing data.

Table 6 : Dates of Sentinel-2 overpasses and simultaneous field campaigns at Karaoun Reservoir with the corresponding number of monitoring sites where transparency measurements were recorded in 2017 and 2018.

	Date of Sentinel-2 overpass and field campaign	Number of monitoring sites
Calibration	30/06/2017	2
	29/08/2017	5
Validation	18/09/2017	4
	20/06/2018	2
	20/07/2018	1

2.6.   3D hydrodynamic modeling

In this section, the description and setup of the 3D hydrodynamic model (Delft3D-Flow) as well as the adjustment of corrected Landsat 8 thermal images for comparison with modeling results are presented.

2.6.1.   Model description and configuration

Delft3D-Flow, version 4.01.01.rc.03 (Deltares, 2013), was used to simulate the hydrodynamics of Karaoun Reservoir. Delft3D-Flow has been proven to simulate well the thermal regime, the hydrodynamics or the response to climate change of large lakes (Wahl & Peeters, 2014), shallow lakes (Soulignac et al., 2017) and reservoirs (Chanudet et al., 2012).

The model was configured to run in hydrostatic mode. The model solves the Reynolds-averaged Navier-Stokes equations for an incompressible fluid with the Boussinesq approximation. The unsteady shallow water equations include the continuity, horizontal momentum and heat transport equations.

In the absence of reliable echo sounder data, the bathymetry of Karaoun Reservoir was constructed with water contours derived from satellite images and the water level measurements provided by the reservoir manager. Water contours were extracted from several Landsat images at dates with different water levels (at the maximum level, and 13.5 m and 17.44 m below the maximum level) (Appendix D).

The horizontal surface of the Karaoun Reservoir was meshed with 3177 Cartesian grid cells of 50 m x 50 m using the Z-grid model. The initial water depth was divided into 65 horizontal layers. The thickness of the 50 higher layers was 0.2 m in order to cover the range of the water level variation during the simulation periods, and 3 m for the 15 lowest layers. Thus, a greater accuracy of the simulated temperature close to the surface was expected. Active mesh layers, especially the cells of the river inlet, changed with the water level according to the bathymetry of the reservoir. The model was forced with the solar radiation, wind speed and direction, rainfall, air temperature and humidity, and with the inflow and outflow rates described previously. The depth-averaged water temperature measured at S_R was used as inflow temperature.

The ocean heat flux model was used to calculate the surface heat budget and the evaporated volume; the latent and sensible heat fluxes due to forced and free convection are parameterized with the values of the Stanton and Dalton numbers recommended by the model authors (Deltares 2013).

The computational time step was set to 1 min and the Courant-Friedrichs-Lewy condition was respected. The vertical eddy viscosity and diffusivity were calculated using the k-ε turbulence model. In the horizontal and vertical directions, the eddy viscosities are defined by:

$$\nu_H = \nu_V + \nu_H^{back} \qquad\qquad 12$$
$$\nu_V = \nu_{mol} + \nu_{3D} \qquad\qquad 13$$

where ν_H is the horizontal eddy viscosity (m^2 s^{-1}), ν_V the vertical eddy viscosity, ν_H^{back} the background horizontal eddy viscosity, ν_{mol} the kinematic viscosity and ν_{3D} the eddy viscosity computed by the k-ε turbulence closure model. In the horizontal and vertical directions, the eddy diffusivities are respectively defined by:

$$D_H = D_V + D_H^{back} \qquad\qquad 14$$
$$D_V = \nu_{mol}/\sigma_{mol} + D_{3D} \qquad\qquad 15$$

with D_H the horizontal eddy diffusivity (m^2 s^{-1}), D_V the vertical eddy diffusivity, D_H^{back} the background horizontal eddy diffusivity, σ_{mol} the Prandtl-Schmidt number (0.7) and D_{3D} the eddy diffusivity computed by the turbulence model.

Horizontal eddy viscosity and diffusivity were computed by the 2D large eddy simulation module (HLES) embedded in Delft3D. Their averages over the whole simulation domain and over the duration of the calibration period, 0.1 m^2 s^{-1} for both, were used as constant and uniform background values ν_H^{back} and D_H^{back} for 3D simulations.

The wind drag coefficient which specifies the magnitude of the surface wind stress was assigned the value of 0.0015. This value is close to the constant values adopted in most modelling studies, e.g. 0.0013 and 0.0019 in 1D model Simstrat for Lake Zurich and Lake Constance (Peeters et al., 2002; Wahl & Peeters, 2014), 0.0018 in a 1D model for Lake Bourget (Vinçon-Leite et al., 2014), 0.0015 in Delft3D-Flow for shallow Lake Créteil (Soulignac et al., 2017) and is consistent with the values expected in the range 1-5 m s^{-1} (Wüest & Lorke, 2003). The bottom roughness was computed with the Chézy formulation, with the default parameter value of 65 m$^{0.5}$ s^{-1}; the vertical wall roughness was neglected.

Amongst the model parameters, only the transparency (Secchi depth) was calibrated by trial and error, focusing on epilimnion temperatures in the perspective of the comparison with satellite images. The calibrated values, 2.5 m in 2012 and 1.7 m in 2017 are within the range of measured values.

2.6.2. *Model simulations*

Simulations start on July 1 2012 and May 12 2017, the dates of the first measuring campaigns, and end on November 21 2012 and September 18 2017, dates of the last available measurements. On each start day, the model was run with the following initial conditions: the measured water level, water at rest, and the water temperature profiles measured at the three monitoring sites.

2.6.3. Correction of satellite thermal data

Landsat 8 TIRS images acquired in 2017 were corrected twice: the generalized single-channel algorithm (SC1) was used for the atmospheric correction of temperatures (Jiménez-Muñoz et al., 2014) as explained in section 2.3.2. These temperatures were then adjusted with bulk temperature measurements, since bulk water temperature and the skin temperature detected by the satellite can differ by several degrees (Schneider & Mauser, 1996; Huang et al., 2017). Thus, bulk, satellite and model temperatures were expected to be more comparable for a second validation of the model with satellite-retrieved temperatures.

The linear regression of bulk temperature measurements versus satellite skin temperatures was used for a further correction of satellite images acquired in 2017. Twenty-one water surface temperatures measured at 0.2 m depth at the three monitoring sites S_R, S_M and S_D were extracted at the time of satellite overpasses. The corresponding atmospherically-corrected satellite-retrieved temperatures were averaged over the four pixels around the monitoring site. The linear regression was used to generate water surface temperature maps. Each was compared with the map of modeled surface temperatures at the time of satellite overpass, basing on a visual interpretation, on the mean and standard deviation (SD) of the spatial distribution and on pixel by pixel differences.

2.7. 3D ecological modeling

In this section, the ecological model and its configuration including the selected processes and biogeochemical variables are described. Further, the model input data and initial conditions followed by the calibration and validation processes are presented.

2.7.1. Model description and configuration

The Delft3D D-Water Quality module (version 5.01.03), making use of the hydrodynamic conditions calculated in the Delft3D-Flow module, was used for ecological simulations at Karaoun Reservoir (Deltares, 2014a). D-Water Quality solves the equations for transport and physical, chemical and biological processes on the basis of the advection-diffusion equation. For each state variable and computational cell, a simplified representation of the advection-diffusion equation is as follows:

$$M_i^{t+\Delta t} = M_i^t + \Delta t . \left[\left(\frac{\Delta M}{\Delta t}\right)_{Tr} + \left(\frac{\Delta M}{\Delta t}\right)_{P} + \left(\frac{\Delta M}{\Delta t}\right)_{S} \right] \qquad\qquad 16$$

with:

M_i^t: The mass at the beginning of a time step.
$M_i^{t+\Delta t}$: The mass at the end of a time step.
$\left(\frac{\Delta M}{\Delta t}\right)_{Tr}$: Changes by transport.

$\left(\frac{\Delta M}{\Delta t}\right)_P$: Changes by physical, chemical or biological processes.

$\left(\frac{\Delta M}{\Delta t}\right)_S$: Changes by sources (e.g. river discharges or waste loads).

Δt : Time step in DELWAQ.

In D-Water Quality, water constituents are divided into several variables, each containing one or more substances with their corresponding processes. In this work the model configuration was selected from the Delft3D-ECO module, a eutrophication model consisting of a specific configuration of substances and processes. In the case of Karaoun Reservoir, the model was implemented for the following 5 variables: dissolved inorganic matter, particulate inorganic matter (IM1), organic matter (dissolved and particulate), phytoplankton and dissolved oxygen (DO). Grazers were not considered as they were not detected during the simulation periods.

The dissolved inorganic matter (Figure 12) variable contains the following substances; Ammonium (noted NH_4 in the software), Nitrate (NO_3^-), Ortho-phosphate (PO_4^{3-}), adsorbed Ortho-phosphate, dissolved Silica (Si) and Opal-Si. The organic matter group consist of Dissolved Organic Carbon (DOC), dissolved Organic Nitrogen (DON) and Dissolved Organic Phosphorus (DOP), each divided into four particulate fractions with different decomposing rates (POC1, POC2, POC3, POC4, PON1, PON2, PON3, PON4, POP1, POP2, POP3 and POP4). For instance, POC1 is the fast decomposing fraction, POC2 is the medium decomposing fraction, POC3 is the slow decomposing fraction and POC4 is the particulate refractory fraction. The same designations apply to the particulate fractions of Phosphorus and Nitrogen. The phytoplankton group was configured to include cyanobacteria, diatoms and green algae.

Water quality processes (Figure 12) include oxygen reaeration between the atmosphere and the water, consumption of oxygen, nitrification of ammonium, denitrification, extinction of light, sedimentation of organic matter and inorganic particulate phosphorus, decomposition and conversion of four fractions of organic matter (detritus) and adsorption and dissolution of phosphate.
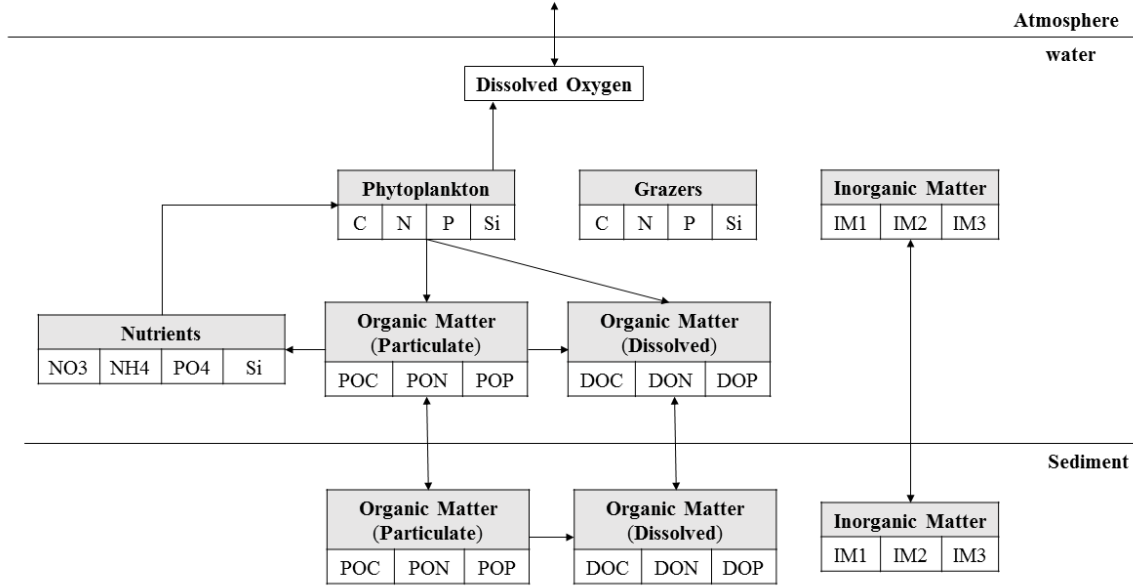
Figure 12: Representation of water quality processes selected in our model configuration (arrows, adapted from Deltares 2014 b).

2.7.2. Oxygen

The dynamics of DO are implicated in atmospheric exchange, nitrification of ammonium, mineralization of organic matter, photosynthetic production and sediment oxygen demand.

2.7.2.1. Reaeration of water

The reaeration rate is characterized by a transfer coefficient for which many formulations have been developed. The model includes 11 different options for the reaeration transfer coefficient from which several are valid for lakes. These options can be selected by the parameter $SWRear$ activated in the model and designated by numbers from 0 till 10 ($SWRear = 0 - 10$).

In this work, the reaeration rate is calculated as Fick's law with a transfer coefficient modulated by temperature ($SWRear = 0$):

$$Rrear = k^{O_2}_{atm_{20}} . \theta^{T-20}_{rear} . (Coxs - Cox) \hspace{2cm} 17$$

with:

$Rrear$: Reaeration rate (gO$_2$. m^{-3}. d^{-1}).
$Coxs:$ Saturation DO concentration (gO$_2$. m^{-3}).
Cox: DO concentration (gO$_2$. m^{-3}) in the surface layer.
$k^{O_2}_{atm_{20}}$: Reaeration transfer coefficient at reference temperature 20 ºC (d^{-1}).
θ_{rear}: Temperature coefficient of the transfer coefficient (-).
$T:$ Temperature (ºC).

2.7.2.2. Dissolved oxygen saturation concentration

In freshwaters, the saturation of dissolved oxygen is a function of temperature and is represented by process SATUROXY implemented in the model. The saturated dissolved oxygen concentration is calculated as follows:

$$Coxs = (a_{oxs} - b_{oxs} \times T + (c_{oxs} \times T)^2 - (d_{oxs} \times T)^3) \times (1) \qquad 18$$

with:

a_{oxs}, b_{oxs}, c_{oxs} and d_{oxs}: Coefficients with different values (-); 14.65, 0.41, 0.08, 0.04, respectively.
T: Water temperature (°C).

2.7.3. Nutrients

2.7.3.1. Nitrification

NITRIF_NH4 is the process implemented for nitrification of ammonium into nitrate. Nitrification removes ammonium and oxygen from the water and produces nitrate. Nitrification is modelled as the sum of a constant background rate (zeroth order process) and an ammonium and oxygen concentration dependent rate (first order process).

The nitrification rate is formulated as follows:

$$R_{Nitrif} = R_{0Nitrif} + fox_{Nitrif} \times (R_{1Nitrif}^{20} \times \theta_{Nitrif}^{(T-20)}) \times C_{ammonium} \qquad 19$$

with:

R_{Nitrif}: Nitrification rate (gN. m^{-3}. d^{-1}).
$R_{0Nitrif}$: Constant background nitrification rate (gN. m^{-3}. d^{-1}).
fox_{Nitrif}: Oxygen limitation function for nitrification (-).
$R_{1Nitrif}$: First order nitrification rate (d^{-1}).
$\theta_{Nitrif}^{(T-20)}$: Temperature coefficient for nitrification (-).
$C_{ammonium}$: Dissolved ammonium concentration (gN. m^{-3}).
T: Water temperature (°C).

The oxygen limitation function becomes equal to a user defined level (default zero) or to a value of 1 below a critical oxygen concentration and above an optimal oxygen concentration respectively. The oxygen limitation function is expressed as follows ($if\ Coxc \leq Cox \leq Coxo$):

$$fox_{Nitrif} = (1 - fox_{Nitrif\ min}) \times (\frac{Cox - Coxc}{Coxo - Coxc})^{10^a} + fox_{Nitrif\ min} \qquad 20$$

with:

$fox_{Nitrif\ min}$: Minimal value of the oxygen limitation function (-).
Cox: Actual dissolved oxygen concentration ≥ 0 (gO₂. m⁻³).
$Coxc$: Critical dissolved oxygen concentration (gO₂. m⁻³).
$Coxo$: Optimal dissolved oxygen concentration (gO₂. m⁻³).
a: Curvature coefficient (-).

2.7.3.2. Denitrification

Denitrification; the microbial reduction of nitrate into nitrogen (N₂) in the absence of oxygen is represented by the process DENWAT_NO₃. In a similar way to nitrification, denitrification is modelled as the sum of a zeroth order process and a first order process. The oxygen function for denitrification becomes equal to zero or to 1 below a critical oxygen concentration and above an optimal oxygen concentration respectively.

$$R_{Denit} = R_{0Denit} + fox_{Denit} \times (R_{1Denit}^{20} \times \theta_{Denit}^{(T-20)}) \times C_{nitrate} \qquad\qquad 21$$

with:

R_{Denit}: Denitrification rate (gN. m⁻³. d⁻¹).
R_{0Denit}: Constant background denitrification rate (gN. m⁻³. d⁻¹).
fox_{Denit}: Oxygen limitation function for denitrification (-).
R_{1Denit}: First order denitrification rate (d⁻¹).
$\theta_{Denit}^{(T-20)}$: Temperature coefficient for denitrification (-).
$C_{ammonium}$: Dissolved ammonium concentration (gN. m⁻³).

The oxygen limitation function is expressed as follows:

$$fox_{Denit} = \left(\frac{Coxc - Cox}{Coxc - Coxo} \right) \qquad if\ Coxo \leq Cox \leq Coxc \qquad\qquad 22$$

2.7.4. Description of the BLOOM model

The BLOOM module in the Delft3D-ECO is a phytoplankton model used to simulate primary production and phytoplankton species composition (Los, 2009) and includes specific formulations for these processes. The performance of this model, in comparison to other phytoplankton models, has not been extensively assessed over lakes and reservoirs. However, BLOOM potential for application over freshwater ecosystems has been highlighted in few studies (Li et al., 2015).

BLOOM mainly depends on the principle of competition for resources including light and nutrient requirements between phytoplankton species. It uses linear programming as an optimization technique of the phytoplankton biomass to select the optimum composition based on the net growth rate and the requirement for resources (nutrients and light) by means of solving a set of linear equations. The time step in BLOOM is of one day and all rates are daily averaged.

BLOOM considers several algal species or groups, each having its proper growth response to temperature, nutrients, light and its own stoichiometry in Carbon, Nitrogen, Phosphorus and *Chl-a*. Unlike other phytoplankton models, in BLOOM different phenotypes are distinguished for every species and they are modelled separately, each with a different set of parameters. These phenotypes include; a Nitrogen limited type (N), a Phosphorus limited type (P) and an energy limited type (E).

The BLOOM module includes the following processes which were taken into consideration in this work: sedimentation of phytoplankton species and determination of average light intensity for phytoplankton as resulting from vertical mixing.

In BLOOM, the specific rates of growth ($R_{growth_i}^{PHY}$), mortality ($R_{mort_i}^{PHY}$) and maintenance respiration ($R_{resp_i}^{PHY}$), formulated as functions of temperature in what follows. The growth rate $R_{growth_i}^{PHY}$ can be formulated according to the type of dependence upon temperature ($TFPM$) which can be linear or exponential.

$$R_{growth_i}^{PHY} = R_{growth_i}^{PHY^0} . \theta_{growth_i}^{PHY^T} \qquad\qquad for\ TFPMxAlg(i) = 1 \qquad\qquad 23$$

$$R_{growth_i}^{PHY} = R_{growth_i}^{PHY^0} . \left(T - \theta_{growth_i}^{PHY^T}\right) \qquad\qquad for\ TFPMxAlg(i) = 0 \qquad\qquad 24$$

$$R_{mort_i}^{PHY} = R_{mort_i}^{PHY^0} . \theta_{mort_i}^{PHY^T} \qquad\qquad\qquad\qquad\qquad\qquad\qquad 25$$

$$R_{resp_i}^{PHY} = R_{resp_i}^{PHY^0} . \theta_{resp_i}^{PHY^T} \qquad\qquad\qquad\qquad\qquad\qquad\qquad 26$$

where; $R_{growth}^{PHY^0}$ is the growth rate at 0 °C (d⁻¹), and not at 25°C as usual for freshwater phytoplankton, θ_{growth}^{PHY} is the temperature coefficient for growth (-), $R_{mort}^{PHY^0}$ is the mortality rate at 0 °C (d⁻¹), θ_{mort}^{PHY} is the temperature coefficient for mortality (-), $R_{resp}^{PHY^0}$ is the maintenance respiration rate at 0 °C (d⁻¹), θ_{resp}^{PHY} is the temperature coefficient for maintenance respiration and T is the water temperature (°C). For the present configuration of the model the default configuration was adopted for the growth rate, with a linear temperature dependence for cyanobacteria and green algae, and an exponential dependence for diatoms.

The optimization technique is met with several constraints in regards to the available amount of nutrients and energy (light), the growth rate and the mortality rate (Los, 2009).

2.7.4.1. Nutrients
The following equation represents the calculation of nutrient balances in the case of autotrophic algae.

$$Ctnut_k = Cnut_k + \sum_{i=1}^{n} anut_{k,i}.PHY_i - Cnutc_k \qquad\qquad\qquad 27$$

with:

$Ctnut_k$: Concentration of the total available nutrient k (g. m^{-3}).

$Cnut_k$: Concentration of the dissolved inorganic nutrient k (g. m^{-3}).

$anut_{k,i}$: Stoichiometric constant of nutrient k in phytoplankton biomass (g. gC^{-1}).

PHY_i: Phytoplankton biomass concentration (gC. m^{-3}).

$Cnutc_k$: Threshold concentration of dissolved inorganic nutrient k (g. m^{-3}). The dissolved nutrient concentration below which phytoplankton are no longer able to withdraw this nutrient from the ambient water.

i: Index for phytoplankton species type.

k: Index for nutrients; 1 for Nitrogen (N), 2 for Phosphorus (P), 3 for Silicon (Si) and 4 for Carbon (C).

n: Number of phytoplankton species types.

2.7.4.2. Light

Each species type is attributed a specific value of the total extinction coefficient which must satisfy the following condition when light becomes limiting in order to calculate phytoplankton biomasses. On the other hand, the total extinction coefficient cannot be smaller than the background extinction coefficient.

$$Kt = \sum_{i=1}^{n} K_i . PHY_i \qquad\qquad 28$$

with:

Kt: Total extinction coefficient for all algae (m^{-1}).

K_i: Specific extinction coefficient of a phytoplankton species type (m^2. gC^{-1}).

2.7.4.3. Growth

It is possible that in a single time step of the model neither light or nutrients become limiting when resources or environmental conditions are improving at a large rate. Thus under such conditions, constraints are set to limit the biomass increase while neglecting mortality. The maximum biomass is thus calculated as:

$$PHYmax_i(t + \Delta tb) = PHY_i(t) . e^{\left(R_{growth_i}^{PHY} . Ef_i - R_{resp_i}^{PHY}\right). \Delta tb} \qquad\qquad 29$$

$$PHYmax_j = \sum_{i=l}^{m} PHYmax_i$$

If $PHYmax_j \geq PHY_{c_j}$ then $PHYmax_j = PHYmax_j$

If $PHYmax_j \geq PHY_{c_j}$ then $PHYmax_j = 0$

with:

$PHYmax_i$: Maximum concentration of phytoplankton species or type at time t2, the end of a time step (gC. m^{-3}).

PHY_{1_i}: Concentration of phytoplankton species or type at time t1, the beginning of a time step (gC. m^{-3}).

Ef: Light efficiency factor. This factor is a function of the light intensity, the amount of available light ($0 \leq Ef \leq 1$).

Δtb: Time step in BLOOM (d).

j : Index for phytoplankton species.

l : Index of the first phytoplankton type for species.

m : Index of the last algae type for species j.

PHY_c: Threshold biomass concentration of a phytoplankton species at time t1, the beginning of a time step.

2.7.4.4. Mortality

Under unfavorable conditions, in order to prevent the total disappearance of phytoplankton within a single time step, the mortality rate is constrained in such a way that the minimum biomass of algae is obtained assuming no production and only mortality. This minimum biomass depends on the initial biomass and the mortality rate. It is computed for each algae species type and it is the result of the summation of all species types.

$$PHYmin_i = PHY_i(t). \; e^{-R^{PHY}_{mort_i} \; . \; \Delta tb} \qquad\qquad 30$$

with $PHYmin_i$ being the minimum concentration of phytoplankton species type (gC. m^{-3}).

2.7.5. Model parameters

The parameters configured in the model including stoichiometric ratios, sedimentation rates, temperature coefficients, mortality and growth rates are presented in Table 7 and Table 8 according to each algae species type selected in this work. Three types are represented; the Energy type (E), the Nitrogen type (N) and the Phosphorus type (P).

Table 7: Specific extinction coefficients, stoichiometric ratios and settling velocities of phytoplankton types defined in BLOOM..

Algal type	K_i (m^2/gC)	$annut_{N,i}$ (g/g)	$annut_{P,i}$ (g/g)	$annut_{Si,i}$ (g/g)	Chla/C (g/g)	w_{PHY} (m/d)
Cyanobacteria-E	0.4	0.225	0.0188	0.0018	0.033	0
Cyanobacteria-N	0.2875	0.125	0.0188	0.0018	0.02	0
Cyanobacteria-P	0.2875	0.15	0.015	0.0018	0.02	0
Greens-E	0.225	0.275	0.0238	0.0018	0.033	0.5
Greens-N	0.1875	0.175	0.015	0.0018	0.025	1
Greens-P	0.1875	0.2	0.0125	0.0018	0.025	1
Diatoms-E	0.27	0.21	0.018	0.66	0.04	1
Diatoms P/Si	0.1875	0.188	0.0113	0.55	0.025	1.5

Table 8: Specific rates and temperature coefficients for growth, mortality and respiration of phytoplankton types defined in BLOOM.

Algal type	$R^{PHY^0}_{growth_i}$ $(1/d)$	$R^{PHY}_{mort_i}$ $(1/d)$	$R^{PHY^0}_{resp_i}$ $(1/d)$	$\theta^{PHY^T}_{growth}$	$\theta^{PHY^T}_{mort_i}$	$\theta^{PHY^T}_{resp_i}$	TFPM
Cyanobacteria-E	0.05	0.01	0.012	3	1.08	1.072	0
Cyanobacteria-N	0.048	0.01	0.012	5	1.085	1.072	0
Cyanobacteria-P	0.048	0.01	0.012	5	1.085	1.072	0
Greens-E	0.068	0.035	0.031	0	1.08	1.072	0
Greens-N	0.068	0.045	0.031	3	1.085	1.072	0
Greens-P	0.068	0.045	0.031	3	1.085	1.072	0
Diatoms-E	0.35	0.035	0.031	1.06	1.08	1.072	1
Diatoms P/Si	0.35	0.045	0.031	1.054	1.085	1.072	1

2.7.6. Input data and initial conditions

Simulations are forced with hydrodynamic, meteorological and hydrological data. Hydrodynamic data are derived from validated Delft3D-Flow simulations and consist of temperature, vertical dispersion and velocity. Meteorological data include daily solar radiation for calculating light intensity in the water column, air temperature and wind speed for the reaeration process, previously used in hydrodynamic simulations (Tal-Amara meteorological station, section 2.2.1). Hydrological data include daily inflow and outflow rates and inflow water temperature computed from the averaged water temperature measured at the monitoring site S_R, also used in hydrodynamic simulations in order to represent the decrease in the water level during the simulation periods (section 2.2.1). Inflowing concentrations of dissolved and particulate organic matters, phytoplankton, DO and nutrients; NO_3^-, NH_4 and PO_4^{3-}, from the Litani River are also required. In 2012 and 2013, the inflow rate was not negligible (> 0.3 m^3/s) during the simulation periods (Figure 13). Available monthly values of nutrients linearly interpolated along the simulation period were used in 2012 in addition to available DO observations. In 2017 and 2018, discontinuous inflow DO observations were adopted as an approximation as well as linearly interpolated nutrients concentrations measured at site S_R in 2018.

Inflowing concentrations of silica, phytoplankton, dissolved and particulate organic matter were not considered. All hydrological data were acquired from the Litani River Authority.

The model was initialized with initial conditions profiles (vertically linearly interpolated) of *Chl-a* (converted to carbon biomass, 0.033), NO_3^- and PO_4^{3-} concentrations (Figure 21, Figure 22). Initial conditions of organic (dissolved and particulate) and inorganic matters were set to zero by default. Observations of DO concentrations at the start date of the simulation were available as initial conditions. Further, DO observations were not frequent during all the simulation periods which prevented a reliable comparison with simulations. Simulation start dates are shown in Table 4 and correspond to field campaigns.

In the initial conditions of each phytoplankton group, only the Energy-type was considered. In 2012, initial conditions were taken at the three monitoring sites S_R, S_M and S_D. Diatoms were not present on the simulation start date. Green algae occurred in very low concentrations and were attributed a uniform value for the energy phenotype as well. Cyanobacteria were the most present (Figure 17).

In 2017, initial conditions were introduced only for cyanobacteria which were dominant. Diatoms and green algae were not present at the start of the simulation (Figure 18).

Initial conditions for NO_3^- and PO_4^{3-} were available at the three monitoring sites in 2013 and 2018 at several depths. Owing to the unavailability of nutrients in 2012 (only at the subsurface) and 2017, values from 2013 (8th of July, at site S_M) were used in the 2012 simulation (Figure 21) and those of 2018 (29th of May; at sites S_R, S_M and S_D) were used in the 2017 simulation (Figure 22).

2.7.7. *Model calibration and validation*

The model ran for three years separately in 2012, 2017 and 2018. It was calibrated in 2012 and then validated in 2017 and 2018. Simulations start and end according to the dates shown in Table 4. Simulations were realized by using BLOOM parameters shown in Table 7 and Table 8. A sensitivity analysis showed both parameters to be calibrated for each phytoplankton group: the mortality rate and the growth rate. All other parameters were set to default values. The settling velocities of phytoplankton were set based on recommended values (Los, 2009).

2.8. Statistical indicators

The performance of the remote sensing algorithms was assessed by estimating the root mean squared error (*RMSE*), the mean absolute error (*MAE*) and the Pearson correlation coefficient (*r*) between observed ($T_{in\ situ}$) and satellite-derived water surface temperatures from the RTE, SC1, SC2 and MW algorithms (T_{RTE}, T_{SC1}, T_{SC2} and T_{MW}).

The hydrodynamic model performance was assessed by comparing model simulations and observations of water level, water temperature profiles at the three monitoring sites. Simulated water temperatures were interpolated at the depths of measurements. The *RMSE* (Root Mean Square Error), *MAPE* (Mean Absolute Percent Error) and *MAE* (Mean Absolute Error) were used as indicators of agreement between model simulations and observations.

The performance of the ecological model was assessed by estimating the root mean squared error (*RMSE*) and the relative root mean squared error (*RRMSE*) between observations and simulations of *Chl-a*.

$$RMSE = \sqrt{\frac{\sum_{i=1}^{n}(X-Y)^2}{n}} \tag{31}$$

$$MAPE = \frac{100}{n}\sum_{i=1}^{n}\left|\frac{X-Y}{Y}\right| \tag{32}$$

$$MAE = \frac{1}{n}\sum_{i=1}^{n}|X-Y| \tag{33}$$

$$RRMSE = \frac{RMSE}{\max(Y)-\min(Y)} \tag{34}$$

Where X and Y are vectors of respectively simulations or satellite-derived water surface temperatures and measurements with a length n.

3. Chapter 3: Field data analysis

In this chapter, data collected in 2012, 2013, 2017 and 2018 according to the methods described in chapter 2 are presented. These data consist of hydrological and meteorological data, water temperature, transparency, *PC*, *Chl-a* and nutrients concentrations. The objective of this chapter is to describe the space and time evolution of the *in situ* data that will be used for comparison with the modeling and remote sensing outcomes applied to Karaoun Reservoir.

3.1. Hydrological and meteorological conditions

Inflow and outflow rates and meteorological data collected in 2012, 2017 and 2018 are presented in Figure 13 and Figure 14 respectively. The inflow rate in 2012 was at its highest in winter where values exceeded 50 m^3/s. It decreased in late spring, summer and autumn however did not disappear completely during this period. On the other hand, 2017 is considered a dry year where the inflow rate reached its peak (31 m^3/s) in winter, was very low in early spring and became negligible from summer onwards. Precipitation was also very low as shown in Figure 14. In 2018, inflow and outflow rates were only available between June and October.

The outflow rate did not show a regular pattern in 2012, 2017 and 2018 and ranged between 0 and 40 m^3/s. The outflowing volume was used for hydropower production and irrigation in 2012 and only for hydropower production in 2017 and 2018. The outflow indicates the decrease in the water level during the simulation periods which are mostly between late spring and early autumn.
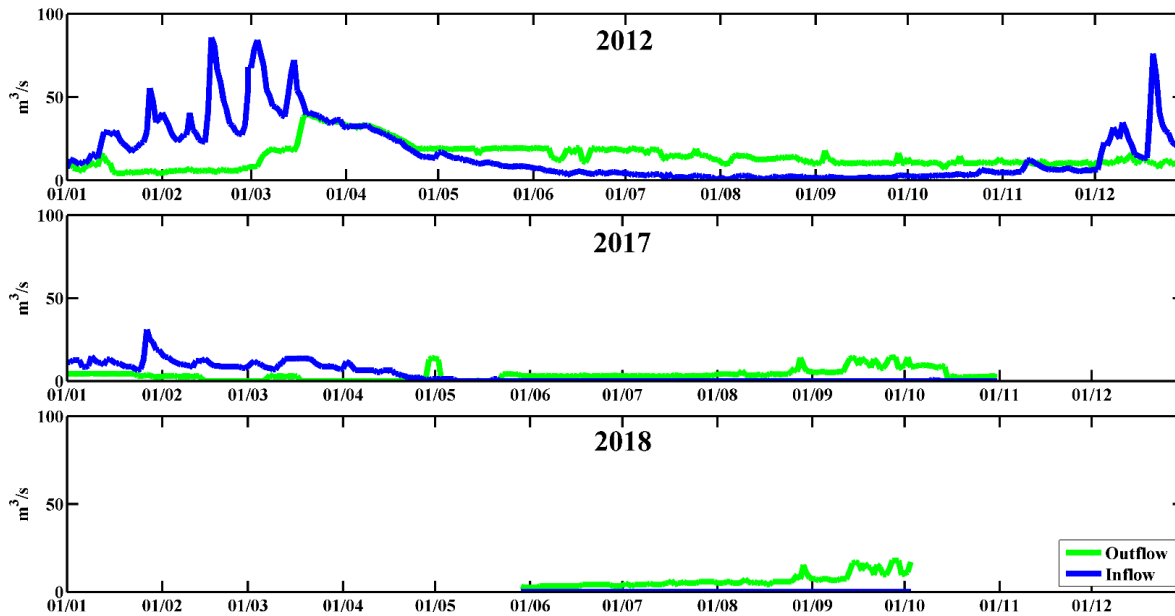
Figure 13: Daily inflow and outflow rates at Karaoun Reservoir in 2012, 2017 and 2018.
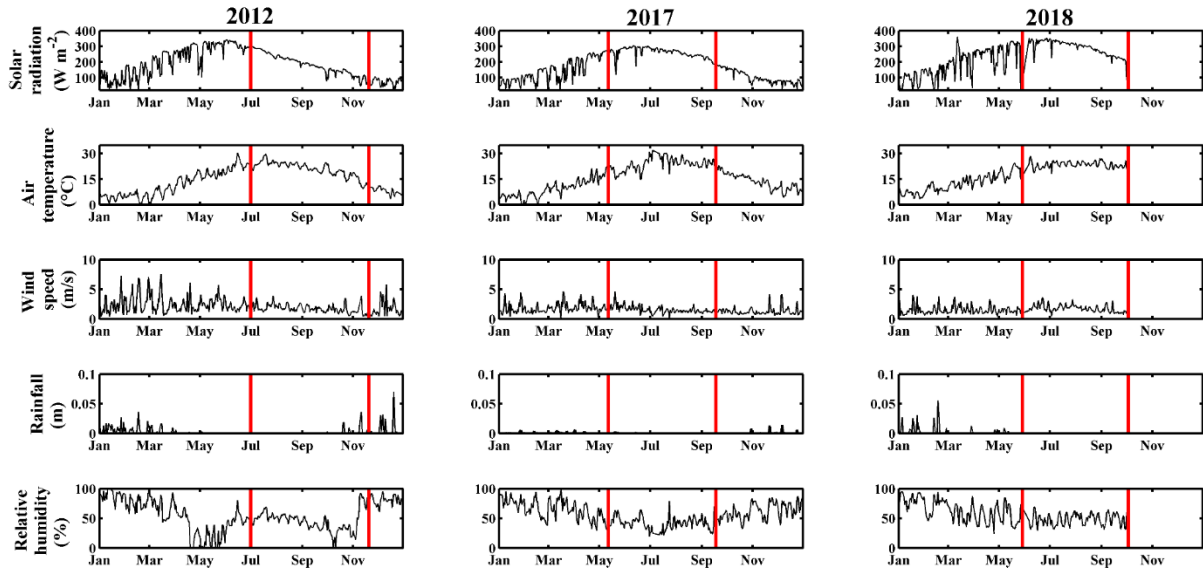
Figure 14: Daily Meteorological data used as input to the model for the 2012, 2017 and 2018 periods: shortwave solar radiation (W m^{-2}), air temperature (˚C), wind speed (m s^{-1}), rainfall (m) and relative humidity (%). The red bars represent the simulation periods.
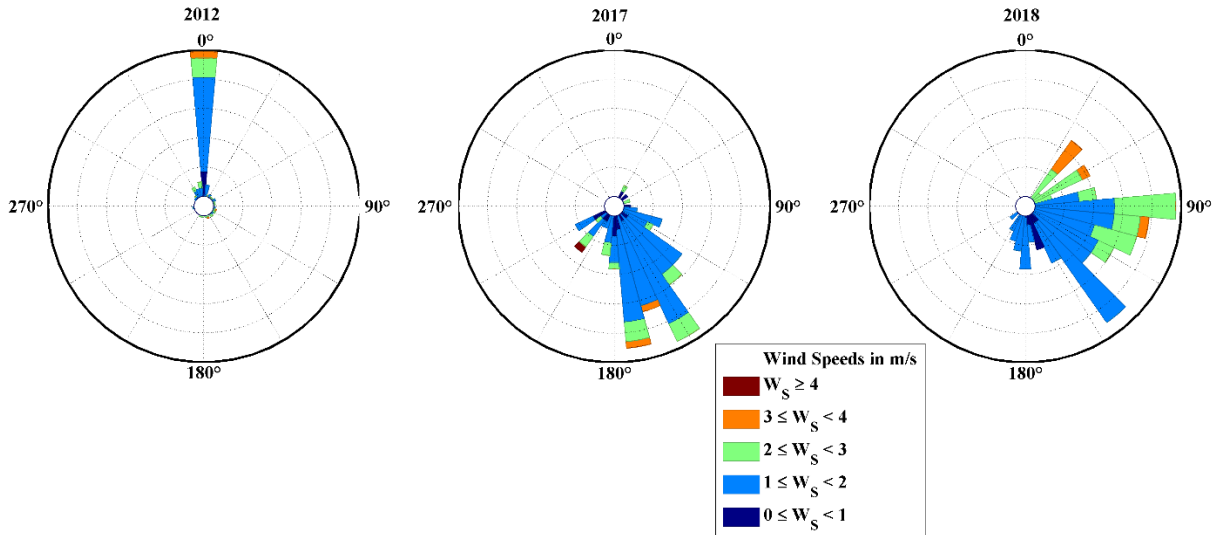

Figure 15: Wind direction and speed in 201, 2017 and 2018 during the simulation periods.

3.2. Water temperature and thermal stratification

Water temperature measurements in 2012, 2017 and 2018 at different depths are shown in Figure 16. In 2012 measurements were available at site S_D at 1, 4, 7, 10, 13 and 16 m depths. In 2017, water temperature was recorded at S_R and S_M at the subsurface (0.2 m), 5, 10 and 15 m depths. At S_D, temperature was recorded at the subsurface, 10, 13 and 16 m depths. Water temperature measurements were collected in 2018 at site S_M at the same depths as in 2017. The loss of thermistor chains disabled the possibility to acquire consistent data at the three monitoring sites.

During all the studied periods, thermal stratification was established and overall persisted till September. In 2012, and owing to the availability of data for a long period, the diminish in thermal stratification can be seen from September onwards where the water column becomes fully mixed, temperature decreases and becomes uniformly distributed along the entire water column.

Considerable water temperature differences occurred between epilimnetic and hypolimnetic waters and among the different years. At site S_D water temperature spanned between 16 and 27 °C in 2012 and 12 and 28 °C in 2017. At site S_M, it ranged between 13 and 28 °C in 2017 and 15 and 29 °C in 2018.
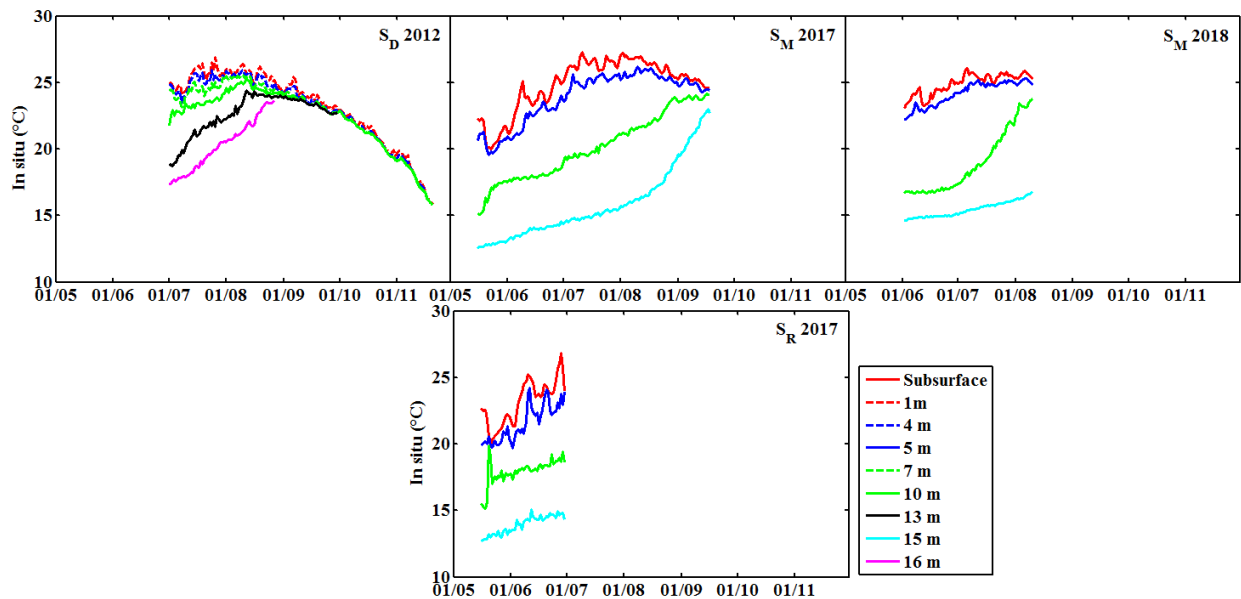
Figure 16: Water temperature measurements at different depths in 2012, 2017 and 2018 at the three monitoring sites.

3.3. Phytoplankton composition

The phytoplankton composition at Karaoun Reservoir varied considerably between 2012 and 2013 on the one hand, and between 2017 and 2018 on the other hand. Figure 17 and Figure 18 represent the distribution of phytoplankton groups and cyanobacteria species in 2012 (between July and November), 2013 (between May and August), 2017 (between May and September) and 2018 (between June and August). Four phytoplankton groups were monitored during these periods;

cyanobacteria, green algae (or chlorophyta), diatoms (or bacillariophyta) and dinoflagellates (or dinophyta).

Between July and November of 2012 and May and August of 2013, cyanobacteria, green algae and dinoflagellates co-existed and varied in abundance according to the environmental conditions. Overall, diatoms occurred in low biovolumes in spring, summer and autumn of 2012. Diatoms were not detected during the studied period in 2013. Cyanobacteria species, *Microcystis aeruginosa* and *Chrysosporum ovalisporum* dominated in summer and early autumn when the water column was stratified. Green algae dominated in spring and dinoflagellates dominated in late autumn.

The phytoplankton composition in 2012 and 2013 differed greatly from that in 2017 and 2018. Between May and September of 2017 and during thermal stratification conditions, the reservoir was dominated by cyanobacteria, mainly *Microcystis* species except on the 31st of June when green algae dominated. Diatoms and dinoflagellates were not detected in 2017 on the dates where sampling was conducted. The phytoplankton community between May and August of 2018 was also mainly composed of cyanobacteria species with no occurrence of other phytoplankton groups over the dates during which field campaigns were conducted under thermal stratification conditions.
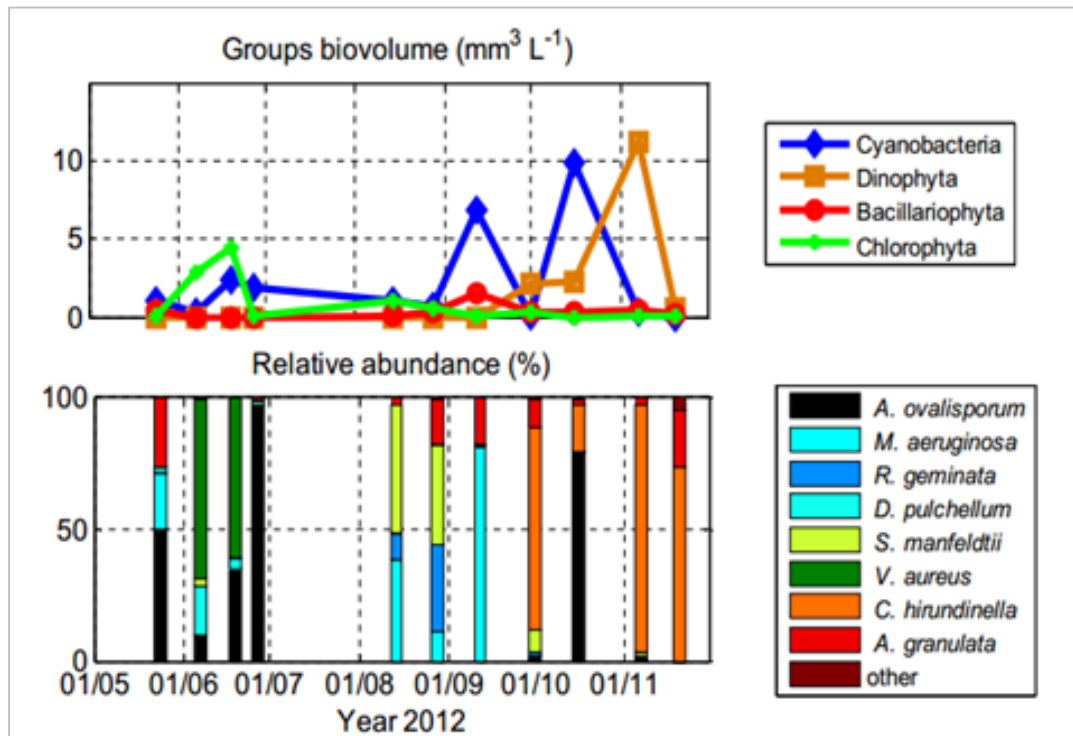

Figure 17: Phytoplankton composition in 2012 at site S_M in the middle of the reservoir. From (Fadel et al., 2014).
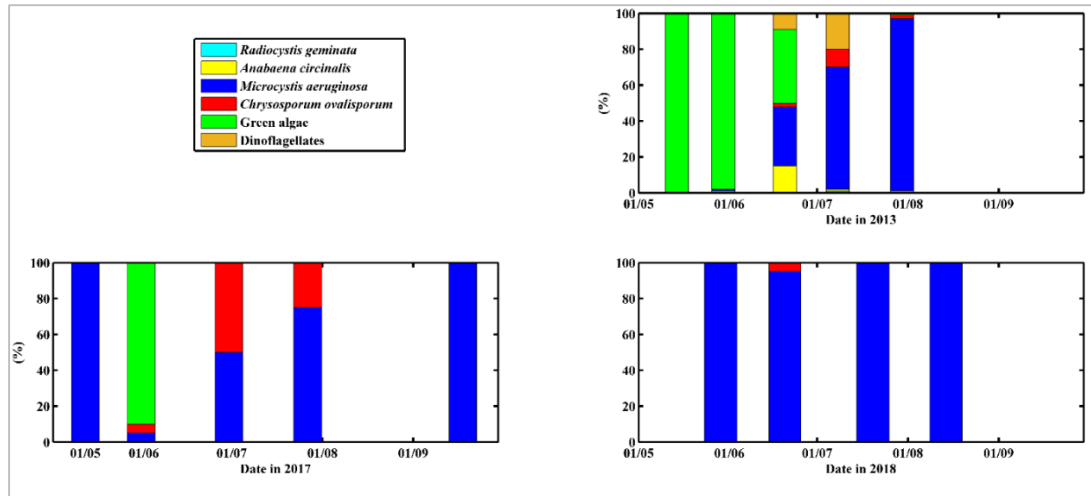
Figure 18: Phytoplankton composition in 2013, 2017 and 2018 at site S_M in the middle of the reservoir.

3.4. *PC* and *Chl-a*

Concentrations of *PC* were measured at Karaoun Reservoir in 2012, 2013, 2017 and 2018 over the three monitoring sites (S_R, S_M and S_D) and at different depths (Figure 19). These concentrations varied greatly over depth and between the months of each year. Overall, concentrations ranged between 1 and 200 µg/L with highest values occurring in summer between 0.2 and 5 m depth. Concentrations increased between July and September of 2012 and then decreased in October and November. In May of 2013 and 2017, *PC* was found in low concentrations which then started to increase between June and August to ultimately decrease in September. In June and July of 2018, concentrations remained high and then decreased in August. Among the concentrations measured at the three monitoring sites; S_R, S_M and S_D, the highest values were recorded at site S_D in 2013, at site S_M in 2017 and at site S_R in 2018.

Chl-a concentrations measured over the three monitoring sites at different depths at Karaoun Reservoir in 2018 are shown in Figure 20 on dates where field campaigns were conducted. *Chl-a* concentrations overall ranged between 1.5 and 210 µg/L in 2018 between May and August. These concentrations increased with time and highest values occurred between the subsurface and 5 m depth. Lowest concentrations were detected at 10 m depth. Further, high concentrations were mainly recorded at site S_R near the Litani River inlet while at sites S_M and S_D an almost similar range of values can be observed.
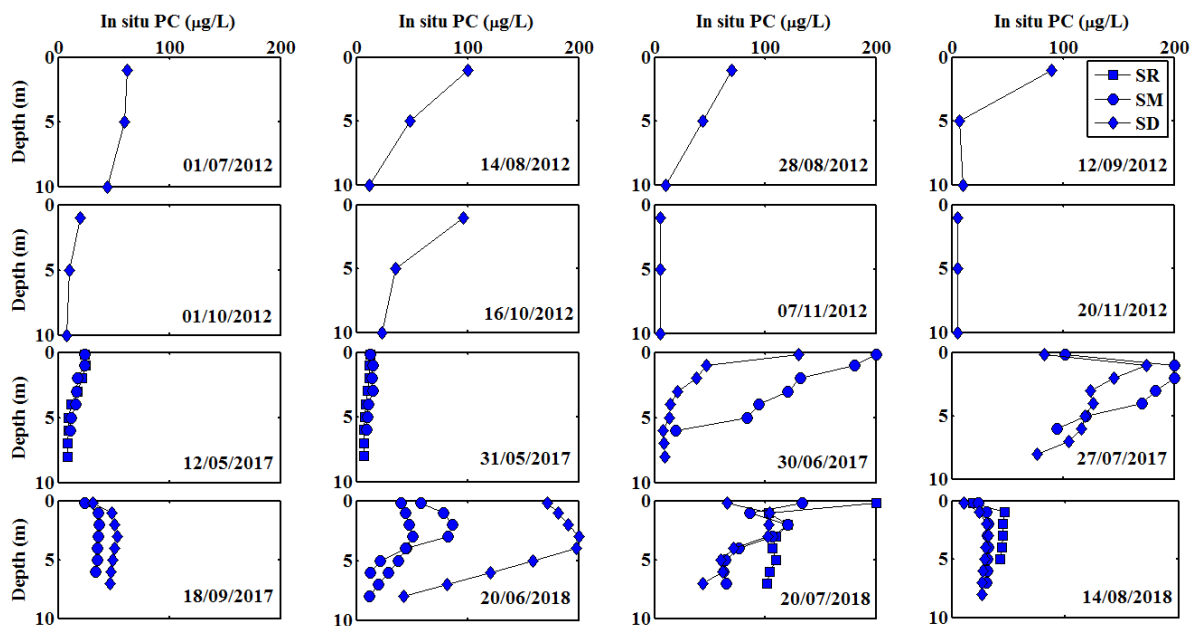
Figure 19: *PC* concentrations measured at Karaoun Reservoir in 2012, 2017 and 2018.
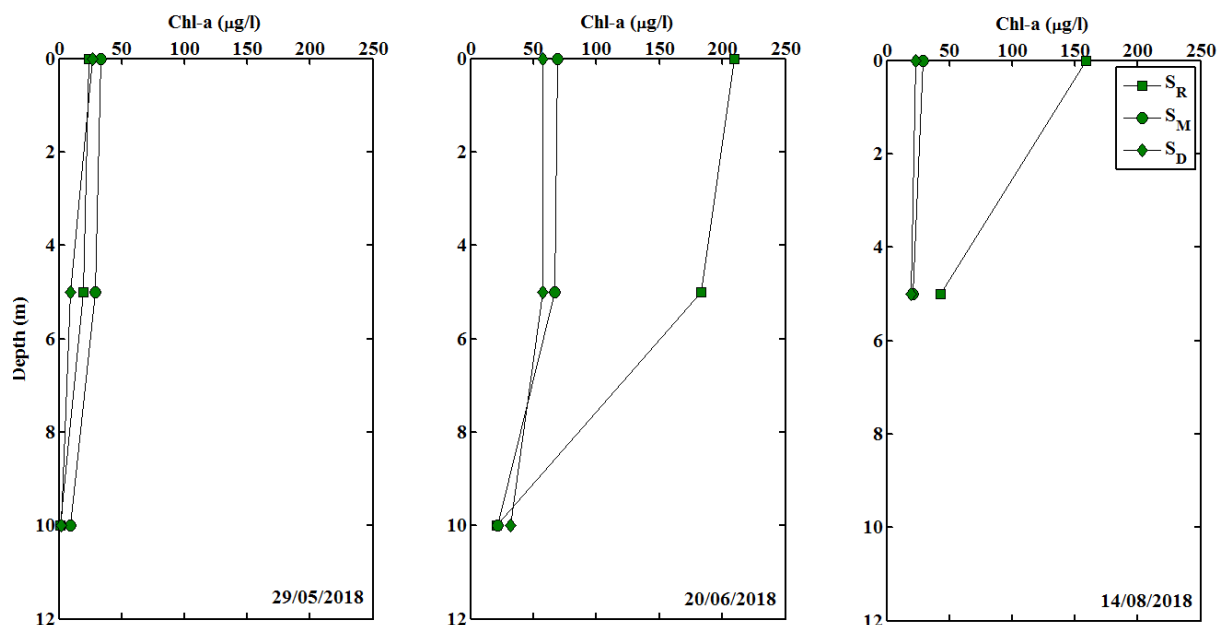
Figure 20: Measured *Chl-a* concentrations in 2018 at the three monitoring sites.

3.5. Nutrients

The concentrations of NO_3^- and PO_4^{3-} were measured over the three monitoring sites (S_R, S_M and S_D) at different depths at Karaoun Reservoir in 2013 (Figure 21) and 2018 (Figure 22). In 2013, NO_3^- concentrations ranged between 0.01 and 0.11 mgN/L. In 2018, concentrations were higher and ranged between 0.01 and 4 mgN/L in 2018. In both years, NO_3^- concentrations were low at the

water subsurface and increased gradually with depth to reach maximal values in the hypolimnion in 2013 and at 10 m depth in 2018.

The concentrations of PO_4^{3-} ranged between 0 (14th of May at site S_M between 0.2 and 10 m depth) and 0.21 mgP/L (on the 8th of June at site S_M at 30 m depth) in 2013. In 2018, concentrations were higher and varied between 0.001 (on the 20th of June at site S_D at 0.2 m depth) and 0.33 mgP/L (on the 29th of May at site S_D at 10 m depth). Similar to NO_3^- concentrations, PO_4^{3-} maximal values were recorded in the hypolimnion in 2013 and at 10 m depth in 2018.
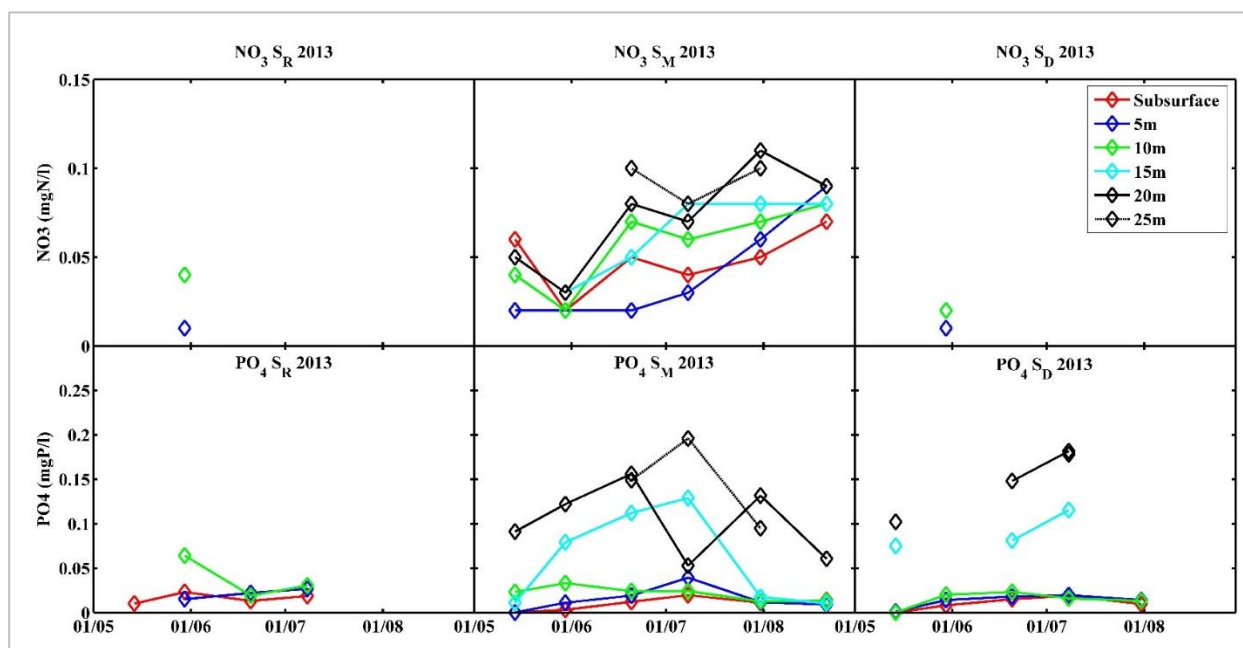
Figure 21: Measured nitrate and orthophosphate concentrations in 2013 at the three observation sites.
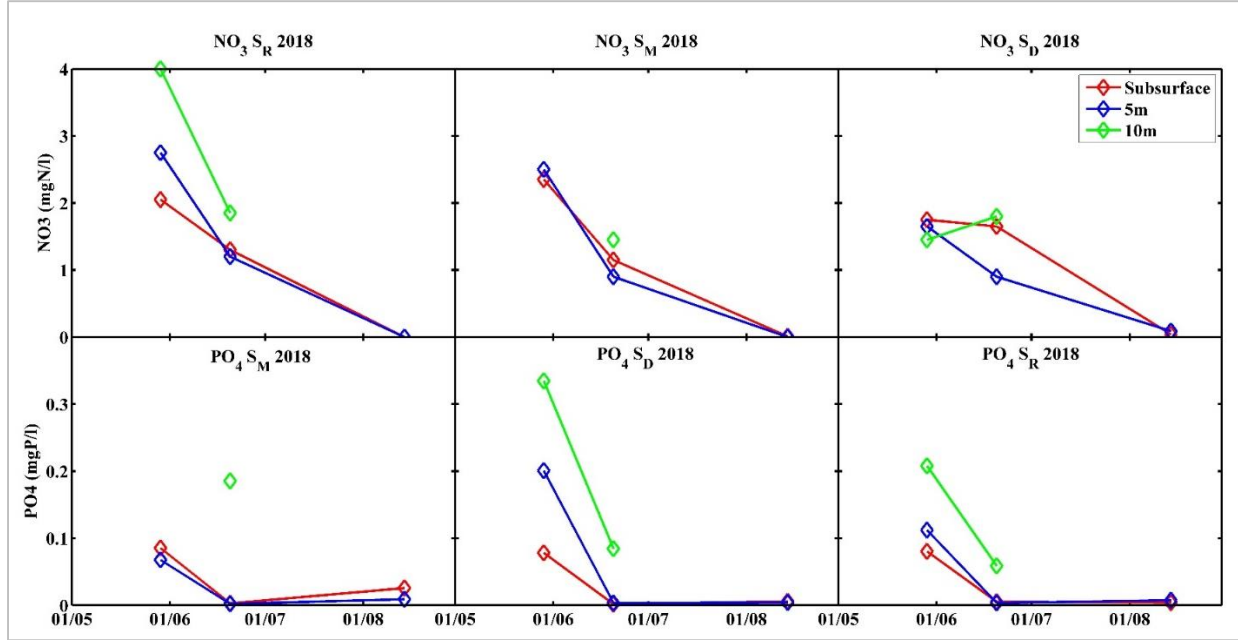
Figure 22: Measured nitrate and orthophosphate concentrations in 2018 at the three observation sites.

3.6. Conclusions

In this chapter, the in-lake data collected during sampling campaigns at Karaoun Reservoir were presented. *In situ* measurements were found in different concentrations across the reservoir between the three monitoring sites. Monitoring the differences in water surface temperature and *Chl-a* concentrations, shown in measurements between the three monitoring sites, can be achieved through remote sensing tools. Satellite images can provide a spatial and temporal representation of surface temperature and *Chl-a* heterogeneities. Extracting water surface temperature and *Chl-a* data from satellite images is also an advantage. Owing to the spatial heterogeneities found in measurements, the choice of a 3D model is valid. Satellite images could serve for the validation of the hydrodynamic-ecological model performance in reproducing the same horizontal distribution of the parameters of interest.

4. Chapter 4: Lake surface temperature retrieval from Landsat-8 and retrospective analysis

In this chapter, a presentation and a discussion of the results of water surface temperature estimation at Karaoun Reservoir using Landsat 8 TIRS data from 2016 and 2017 using previously calibrated algorithms are provided. The adopted methodology and the description of the algorithms are provided in section 2.3. The performances of the Radiative Transfer Equation (RTE), the Single Channel algorithm (SC1) and its improved version (SC2) and the Mono-Window algorithm (MW) are compared and discussed. Further, the retrospective analysis of water surface temperature is analyzed and compared to similar studies.

This chapter was published in the Journal of Applied Remote sensing.

Reference: Sharaf, N., Fadel, A., Bresciani, M., Giardino, C., Lemaire, B.J., Slim, K., Faour, G. and Vinçon-Leite, B., 2019. Lake surface temperature retrieval from Landsat-8 and retrospective analysis in Karaoun Reservoir, Lebanon. *Journal of Applied Remote Sensing*, 13(4), p.044505.

4.1. Algorithms performance

In order to validate surface temperature retrieval, observed water surface temperatures were compared to estimates by the RTE, SC1, SC2 and the MW algorithms. The results are summarized in Figure 23. The values of the statistical indicators suggest a good agreement between measurements and estimations of surface temperatures. Very high correlations were obtained with the four approaches (Table 9). With $r = 0.97$ for T_{SC1} and 0.96 for T_{SC2}, the SC1 and SC2 methods showed the highest correlations and least errors. The SC1 and SC2 algorithms yielded *RMSE*s of 0.73 and 0.89 K and *MAE*s of 0.71 and 0.88 K respectively. The RTE also performed well however with a bias as seen on its *MAE* of 1.6 K and a *RMSE* of 0.94 K. The MW algorithm displayed the weakest results with a *RMSE* and a *MAE* of 1.23 and 1.01 K respectively.

Further, the *RMSE* values observed in each approach agree with values found in similar validation studies (Lamaro et al., 2013; Simon & Danis, 2014) over reservoirs. For the SC1 algorithm for instance, Jiménez-Muñoz et al. (2014), whose estimations were validated with simulated data selected over land, obtained *RMSE*s around 1.5 K only when the water vapor content is lower than 3 g cm^{-2}. In this study, *RMSE* is 0.73 K but the water vapor content remained in the range where the SC1 algorithm performs best. For a more humid atmosphere, *RMSE*s could reach up to 5 K when using the SC1 algorithm (Jiménez-Muñoz et al., 2014).

Among the four approches, the SC1 algorithm gave the highest correlations and lowest *RMSE* and *MAE* in this study. Based on these results and as long as the water vapor content is in the recommended range, the SC1 algorithm is the preferable method for estimating surface temperature from TIRS Band 10 at Karaoun Reservoir. Unlike the RTE and the MW algorithm, it minimizes the input of atmospheric parameters and thus the errors are mostly restricted to the accuracy of the water vapor content.

Figure 24 shows the difference between *in situ* water surface temperatures and estimates from the SC1 and SC2 algorithms plotted versus the water vapor content. The water vapor content ranges from 1 to 3 g cm^{-2}. The difference between $T_{in\ situ}$ and T_{SC1} exhibits no trend with the water vapor content ($p = 0.10$). The range of differences exceeds the -1 K – 1 K interval (standard deviation SD is 0.84 K). This range is consistent with literature results (Cristóbal et al., 2018). Whereas García-Santos et al. (2018) observed an increase in the errors with the water vapor content, the lack of trend here can be attributed to its small range, with few points at high values.

The differences are slightly higher for the SC2 algorithm with a standard deviation of 1.07 K and some differences above 2 K. Cristóbal et al. (2018) reported better estimations and less bias with the SC2 algorithm: their errors tended to be within the -1 K – 1 K range. However, they also reported that the performance of the SC2 algorithm and hence the expected errors can differ between different types of study sites. For example, they found that the SC2 algorithm performed better over vegetation than snow which can be due to emissivity. These findings call for additional validation studies over inland waterbodies where, in comparison to land, the performance of such algorithms was seldom assessed.
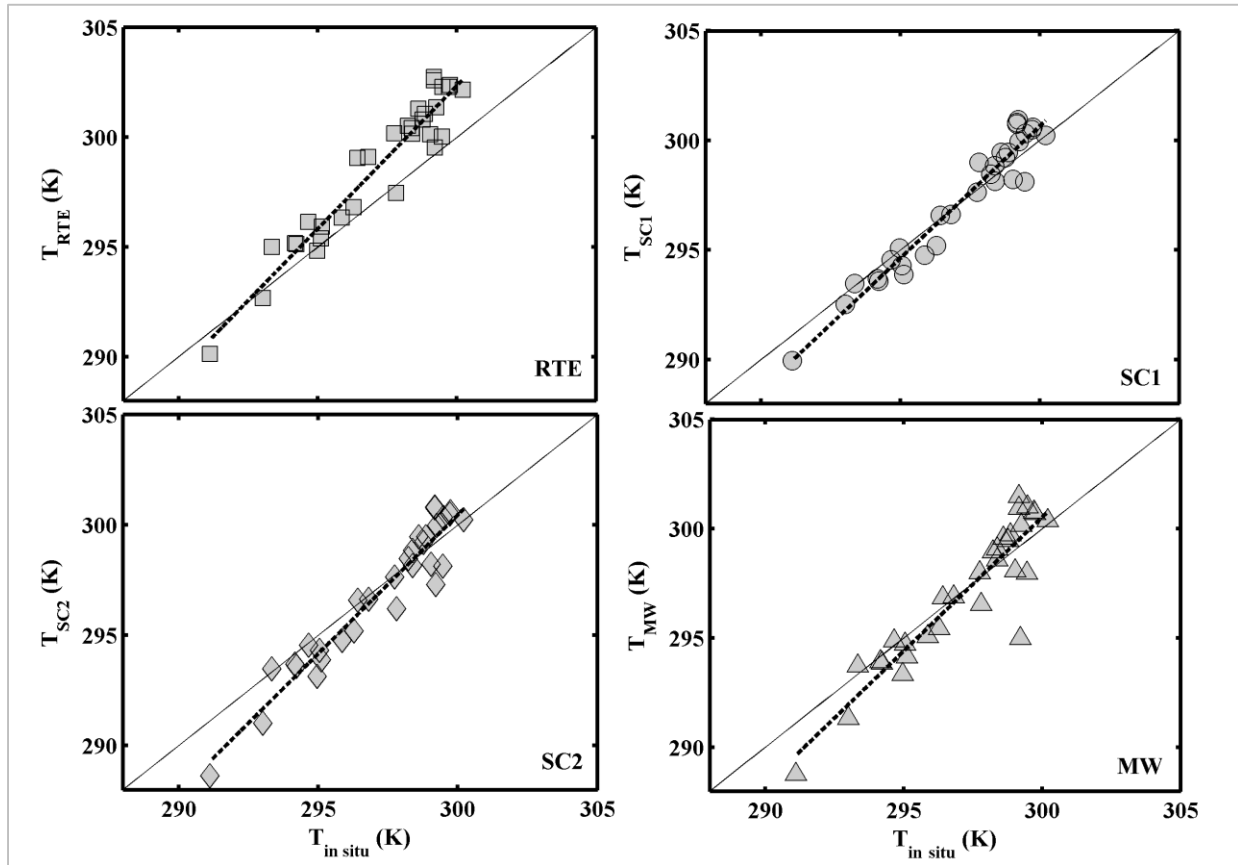

Figure 23: Temperature measurements ($T_{in\ situ}$) in 2016 and 2017 versus corrected Landsat 8 TIRS Band 10 data (T_{RTE}, T_{SC1}, T_{SC2} and T_{MW}) respectively from the RTE, the SC1, the SC2 and the MW algorithms ($n = 31$) with the following equations: $y_{RTE} = 1.31x - 88.9$, $y_{SC1} = 1.2x - 60.6$, $y_{SC2} = 1.26x - 77.11$, $y_{MW} = 1.23x - 67.1$.

Table 9: Pearson correlation coefficient *r*, Root Mean Squared Error *RMSE* (K) and Mean Absolute Error *MAE* (K), between field measurements ($T_{in\ situ}$) and estimations from the RTE (T_{RTE}), the SC1; SC2 algorithms (T_{SC1} and T_{SC2}) and the MW algorithm (T_{MW}).

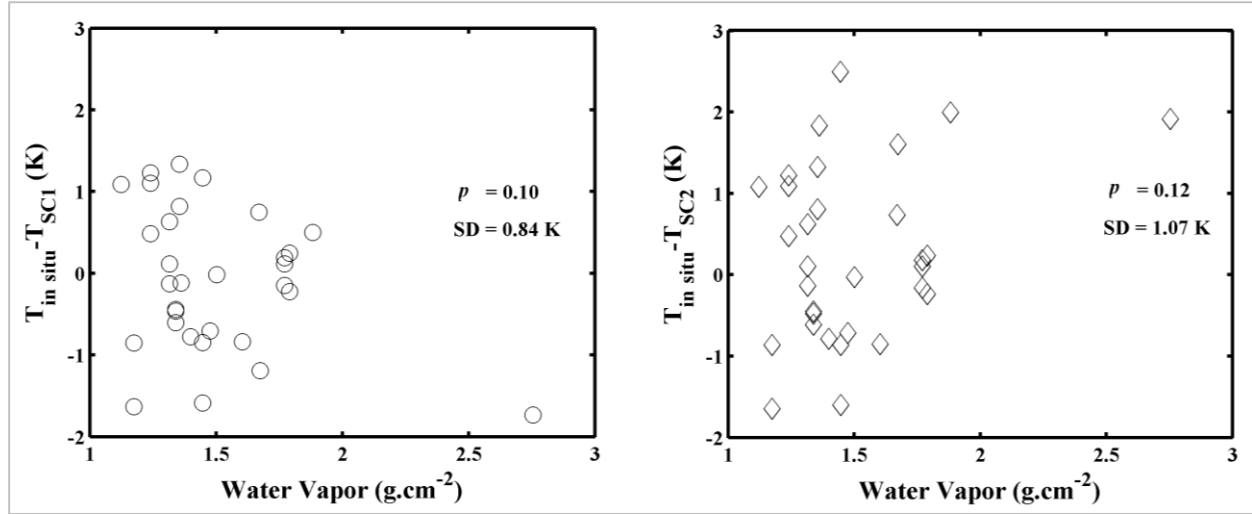|	*r*	*RMSE* **(K)**	*MAE* **(K)**
T_{RTE}	0.95	0.94	1.6
T_{SC1}	0.97	0.73	0.71
T_{SC2}	0.96	0.89	0.88
T_{MW}	0.92	1.23	1.01

Figure 24: Difference of *in situ* and surface temperatures in 2016 and 2017 as a function of the water vapor content, *n = 31*.

A difference of a few degrees can be observed between satellite derived skin temperatures and *in situ* bulk water temperatures (Becker & Daw, 2005; Huang et al., 2017). Most often, skin temperatures are cooler than bulk temperatures. This is called the cool skin effect (Crosman & Horel, 2009) although other sources of mismatch might explain this difference (e.g. the thermal emission by adjacent targets).

Validating satellite-derived surface temperatures is quite a challenge as atmospheric conditions can greatly influence the accuracy of the process, while the timing and the depth at which water surface temperature is measured *in situ* might not be directly comparable to satellite estimations. The main error sources in surface temperature retrieval associated with the SC1 algorithm arise from atmospheric effects and surface emissivity uncertainties. This algorithm requires only water vapor content and surface emissivity. Unfortunatly, these variables have never been measured at Karaoun Reservoir. The fact that these variables are obtained through modelling or approximations makes it, to a certain degree, difficult to obtain minimal discrepancies between remote sensing estimations and ground observations. As for *in situ* surface temperatures, they were recorded simultanuously with the Landsat 8 overpasses for all dates, thus avoiding another source of

uncertainty. Measurements of *in situ* bulk temperatures were recorded at 50 and 20 cm below the surface, whereas satellite-derived temperatures are provided at the top millimeter of the water surface layer. Differences between the measurement depth of lake *in situ* and satellite surface temperature estimations are neglected, since measurements have been shown to be representative of satellite-derived surface temperatures, at least during morning overpasses (11:10 am) (Schneider & Mauser, 1996).

4.2. Historical analysis of water surface temperature

Using the SC1 algorithm, water surface temperature was retrieved from Band 6 and Band 10 of the Landsat TM and TIRS respectively between 1984-2015 and in 2018 using 153 cloud free images. Water temperature was averaged over the reservoir surface. Between 1984 and 2018, remote sensing estimations did not indicate a significant warming trend with a very high *p* value of 0.9 for the whole data series. During that period, surface temperature ranged between 290 and 304 K with the latter, highest temperature, being recorded in August of 2001. According to each month of the year, the highest temperatures were found in the following years; 2006 for May, 1990 for June, 2013 for July, 2001 for August, 1985 for September and 1999 for October (Figure 25). Moreover, there is no significant trend in the surface temperatures sorted by month in the year.
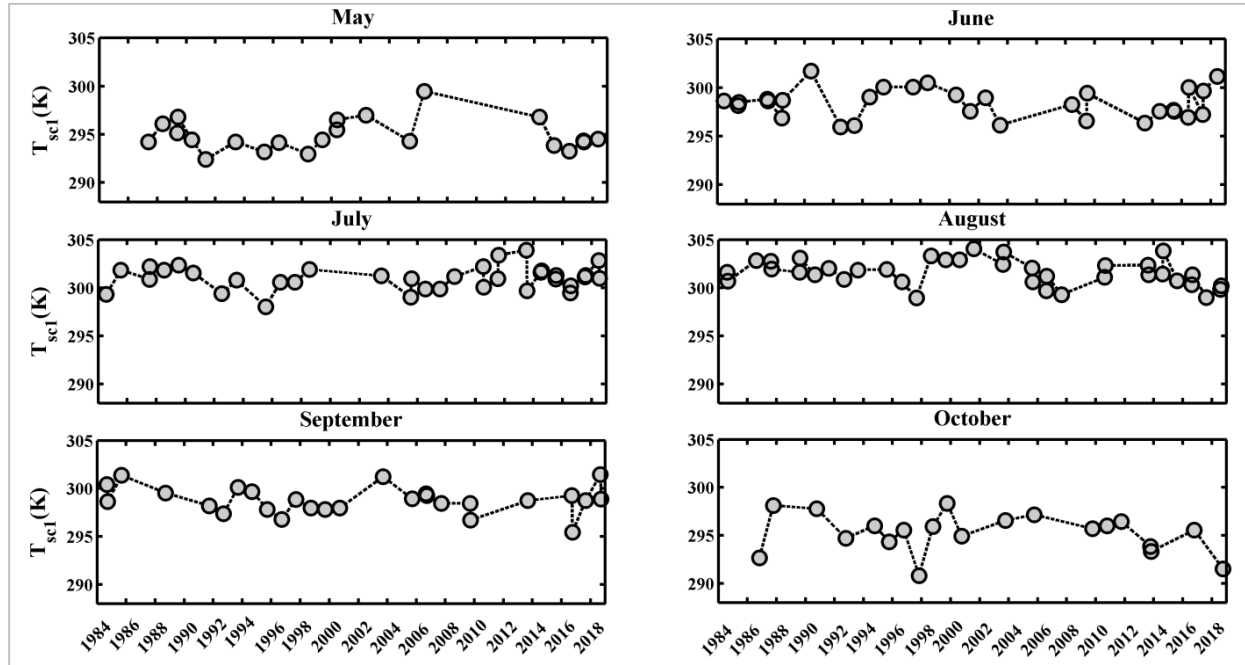
Figure 25: Surface-averaged water temperature (T_{SC1}) between 1984 and 2018 derived from Landsat 4, 5 and 8.

Deutsch & Alameddine (2019) conducted a retrospective study of water surface temperature over Karaoun Reservoir between 1984 and 2015 and did not find a significant warming trend except in August. They initially applied the SC1 algorithm to the period 2000-2015. However instead of using water vapor content to calculate the atmospheric functions and thus avoid the use of several

atmospheric parameters, they adopted τ, L_u and L_d from NCEP data as input to the algorithm. They also found that bewteen 2000 and 2015 brightness temperatures derived from Landsat sensors were in better correlation with *in situ* measurements of surface temperature than with the atmospherically corrected estimates. This further led to their use of brightness temperature and *in situ* measurements to develop a linear regression model and derive data prior to 2000, in order to ultimately analyze the suface temperature trend between 1984 and 2015. The use of three atmospheric parameters (τ, L_u and L_d) as input to the SC1 algorithm and brightness temperature data instead of atmospherically corrected surface temperatures could add uncertainty in surface temperature retrieval (García-Santos et al., 2018). With reference to the historical analysis of surface temperature at Karaoun Reservoir, this can also explain the difference between the findings of Deutsch & Alameddine (2019) and this work in which a warming trend of surface temperature was not discernable between 1984 and 2018 after applying the SC1 algorithm in its original form, namely with water vapor data and emissivity as only inputs.

Surface temperatures of inland waterbodies have been used as indicators of climate change (O'Reilly et al., 2015). Yet such studies are still limited, due to the lack in long-term measurements, and focus on waterbodies greater than 500 km^2 (Schneider & Hook, 2010), thus neglecting small to medium sized lakes and reservoirs.

Some of the climate-induced changes to lake physical properties are manifested by higher water surface temperatures, the earlier onset and longer periods of thermal stratification and overall greater lake stability (Fadel et al., 2019; Jeppesen et al., 2009; Stainsby et al., 2011; Vinçon-Leite et al., 2014). These manifestations have been largely attributed to meteorological forcing and morphometry. Although it is commonly considered and shown that lake and reservoir water temperature will warm in synchrony with increasing air temperatures (Williamson et al., 2009), the latter is not always reflected in long-term temperature trends in reservoirs (Moreno-Ostos et al., 2008). The thermal dynamics differ between lakes and reservoirs. Reservoirs experience large fluctuations in the water level, often irregular over the years due to operational constraints, and thus thermal dynamics are expected to be more variable in contrast to many lakes where the water volume does not change significantly and the seasonal heat dynamics dominates. Therefore, the fact that the conditions at Karaoun Reservoir are not seasonally reproducible might have disabled the possibility to detect a warming trend of surface temperature although the influence of other climatic factors should not be excluded.

Studies dealing with warming trends of lake and reservoir surface temperature in the Middle East are scarce except for Lake Kinneret, Israel. The analysis of the surface temperature record (1984 – 2018) of Karaoun Reservoir contrasts the trend found at Lake Kinneret which revealed a warming (~ 0.036°C yr^{-1}) of lake summer surface temperature between 1969 and 2015 (Blunden & Arndt, 2016). However, the increase in water temperature at Lake Kinneret was mainly

attributed to anthropogenic activities such as the reduction in the water level while climate change had a minor influence (Ostrovsky et al., 2013).

Water surface temperature is a key parameter for determining ecological processes in lakes and reservoirs as it influences biological processes such as the primary productivity. In lake Dianchi, China, surface water temperature was found to be the main cause of algal bloom development (Yang et al., 2018). At Karaoun Reservoir blooms of toxic species of cyanobacteria have occurred annually since 2009. Between 1984 and 2007, a recent study making use of a remote sensing algorithm to derive concentrations of the *PC* pigment demonstrated the occurrence of cyanobacteria at Karaoun Reservoir (Sharaf et al., 2019a). Concentrations were found to be significantly high (> 50 μg/L) with a peak of *PC* concentration occurring in May of 2006 thus coinciding with the highest temperature recorded in May between 1984 and 2018 as shown in this work.

Acquiring a long term record of water quality parameters is valuable especially in Middle Eastern areas where lakes and reservoirs are poorly monitored. The record of water surface temperature found in this work is an additional source of data which can complement *in situ* observations and interpolate temporal gaps. Water surface temperature data can also have implications for reservoir management through environmental applications. It reflects the impact of climate change, stratification and mixing. Further it can also be used to understand the hydrological cycle and verify hydrodynamic models.

The results obtained in this chapter will serve for generating water surface temperature maps from Landsat 8 validated surface temperature data in 2017. These maps will be further compared to those generated from the 3D hydrodynamic model in the following chapter 5 in order to assess the ability of the latter to reproduce the distribution of water surface temperature.

5. Chapter 5: Thermal regime of reservoirs: A satellite and 3D modeling approach

The aim of this work is to assess whether satellite imagery combined with 3D modelling can provide sufficient information for understanding the thermal regime of poorly monitored reservoirs. For doing so, the performance of the 3D model was first assessed and the simulated temperature validated by comparison to satellite data, on a reservoir in a semi-arid region, Karaoun reservoir, Lebanon.

The performance of the 3D model Delft3D-Flow to simulate the thermal regime was first investigated with *in situ* measurements. In parallel, water surface temperatures were retrieved from Band 10 of the thermal infrared sensor onboard Landsat 8 and adjusted with *in situ* measurements. Further, the spatial distribution and time evolution of surface temperature observed by the satellite and simulated by the model were compared. The description and configuration of the Delft3D-Flow model and the adjustment of corrected Landsat 8 thermal images are presented in section 2.5.2.

This chapter was published in the Inland Waters Journal.

Reference: Sharaf, N., Lemaire, B.J., Fadel, A., Slim, K., and Vinçon-Leite, B., 2021. Assessing the thermal regime of poorly monitored reservoirs with a combined satellite and three-dimensional modeling approach. *Inland Waters*, [doi:10.1080/20442041.2021.1913937].

This section presents the model validation in two steps. A first sub-section focuses on the performance of the model for simulating the evolution of both the water level and the vertical temperature profile. A second sub-section details the results of the correction of satellite temperatures and the comparison of surface temperature heterogeneities in model simulations and in satellite maps.

5.1. Validation of the hydrodynamic model with field measurements

The performance of the Delft3D-Flow model was validated by comparing measurements and simulations of the water level and of the water temperature profile at the three monitoring sites.

5.1.1. *Water level*

Time series of measured and simulated water levels in 2012 and 2017 are shown in Figure 26. The study periods, from 1 July 2012 to 21 November 2012 and from 12 May 2017 to 18 September 2017, are marked by very low inflow rates from the Litani River, especially in 2017, and by considerable drawdowns in the water level, 15 m in 2012 and 8 m in 2017 (Figure 13). The comparison between model results and measurements of water level (Figure 26) shows that the model reproduced very well the general drawdown in the water level at the time of the study, with a MAE and a RMSE smaller than 0.2 and 0.3 m respectively, corresponding to less than 2% (MAPE) of the water depth (Table 10).
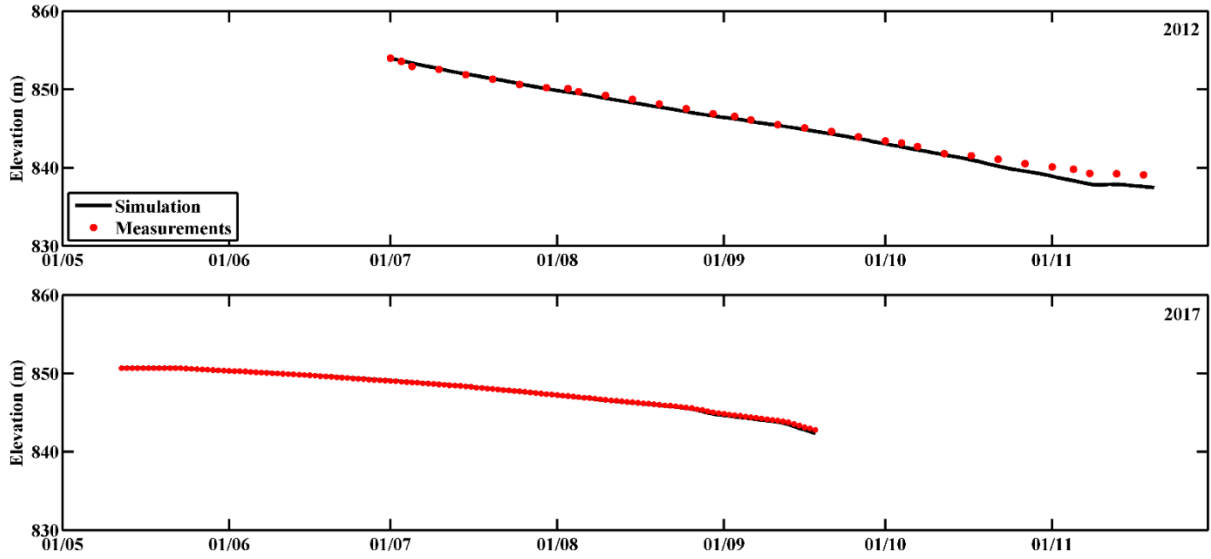
Figure 26: Daily averaged model results and measurements of the water level in 2012 and 2017. Date format is day / month.

Table 10: Simulation performance indicators for the water level in 2012 and 2017.

	Water level	
	2012 (n = 33)	**2017 (n = 130)**
RMSE (m)	0.2	0.1
MAPE (%)	1.7	0.3
MAE (m)	0.2	0.1

5.1.2. *Water temperature and thermal stratification*

Simulations of water temperature in 2012 and 2017 were undertaken under thermally stratified conditions, except in October and November of 2012 when the reservoir was mixed. Figure 27 represents simulated and measured water temperature contours for sites S_D in 2012, and for S_R and S_M in 2017. The corresponding difference between simulated and measured water temperatures is shown in Figure 28. A comparison in space and time is only possible at site S_M in 2017, with measurements covering the simulation period and depths down to 15 m. The Delft3D-Flow model predicted well daily vertical profiles of water temperature, the establishment of thermal stratification, partial and full mixing with small discrepancies.

In July 2017 , the model overestimated temperature in surface layers by up to 4°C in early July but MAE is 0.5°C over the whole simulation period (Table 11). At site S_D in July 2012, the overestimation occurred both at the surface and at the thermocline. For both years, the MAE and the RMSE do not exceed 2ºC at all depths at the three monitoring sites (Table 11). The relative errors (MAPE) of epilimnion temperature do not exceed 5%.

The thermal stratification was established between June and September of 2012 and 2017, a warm epilimnion formed at the surface. Thermal stratification persisted till the end of September with a thermocline established between 5 and 15 m. The maximum temperature difference between the subsurface and the top of the hypolimnion was of 10°C in 2012 and 16°C in 2017. The model represented well this behavior, including the maximum temperature difference, 11.9°C in 2012 and 14.7°C in 2017.

Based on these results, the model is considered to have a satisfactory performance and simulated surface temperatures can be further compared to satellite images.

Table 11: Simulation performance indicators for the water temperature at the different depths at the three monitoring sites. The indicators were calculated with hourly values over to the periods shown in the table.

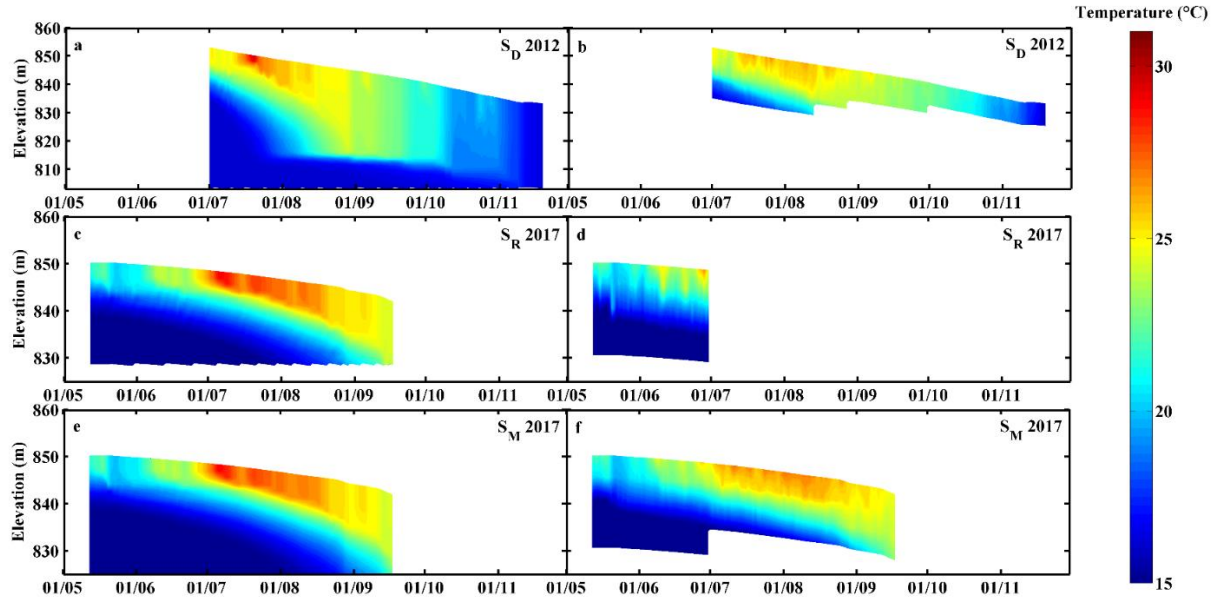|		2012					
	Period	01/07 - 21/11 ($n = 3433$)					01/07 – 27/08 ($n = 1369$)
S_D	**Depth (m)**	**1**	**4**	**7**	**10**	**13**	**16**
	RMSE (°C)	0.9	0.9	0.6	0.5	1.0	1.9
	MAPE (%)	2.5	2.2	1.8	1.8	3.7	7.5
	MAE (°C)	0.6	0.5	0.4	0.4	0.9	1.7
		2017					
	Period	12/05 – 30/06 ($n = 1177$)					
S_R	**Depth (m)**	**0.2**	**5**	**10**	**15**		
	RMSE (°C)	0.7	0.7	1.2	0.9		
	MAPE (%)	2.3	2.2	5.0	5.1		
	MAE (°C)	0.6	0.5	1.0	0.7		
	Period	12/05 – 18/09 ($n = 3097$)					
S_M	**Depth (m)**	**0.2**	**5**	**10**	**15**		
	RMSE (°C)	0.8	0.5	0.6	1.2		
	MAPE (%)	1.9	1.5	2.5	5.0		
	MAE (°C)	0.5	0.3	0.6	1.1		
S_D	**Depth (m)**	**0.2**					
	RMSE (°C)	1.1					
	MAPE (%)	2.8					
	MAE (°C)	0.7					

Figure 27: : Daily averaged simulated (a, c, e) and measured (b, d, f) water temperature at sites S_D in 2012 and S_R and S_M in 2017. Measurements at fixed depths were linearly interpolated. The jump in the maximum depth of measurements corresponds to each time the deeper sensors were removed when they approached the sediment (b and f). Date format is day / month.
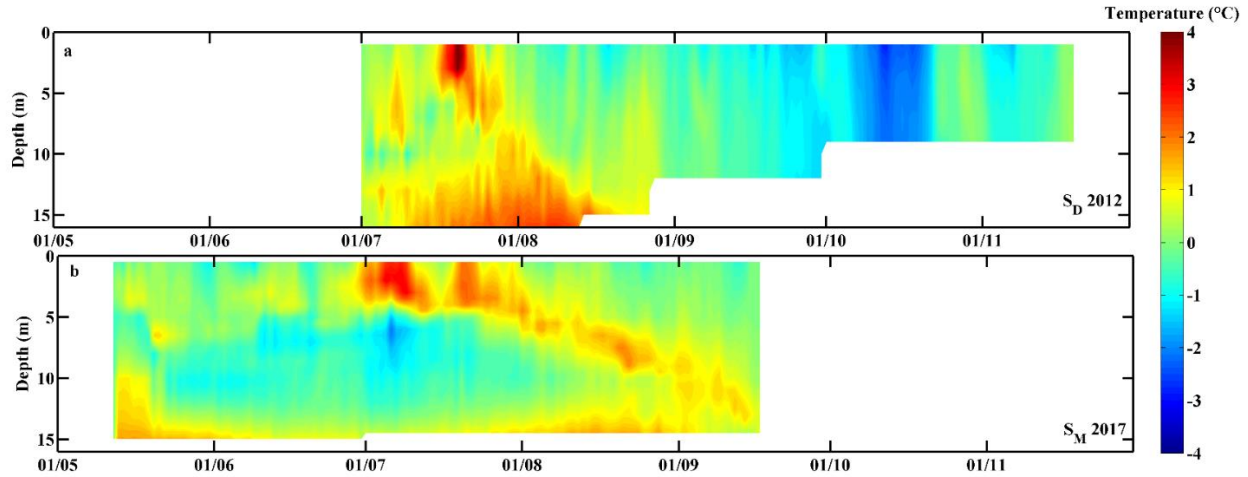

Figure 28: Differences between simulated and measured temperatures at sites S_D in 2012 (a), and S_M in 2017 (b). Date format is day / month.

5.2. Validation of the hydrodynamic model with satellite images

5.2.1. *Efficiency of the correction of satellite skin temperature with measured sub-surface temperature*

After atmospheric correction, satellite surface temperatures were compared to measured temperatures at 0.2 m depth at the three monitoring sites and on eight dates (Figure 29). The values of the statistical indicators indicate a good performance of the atmospheric correction algorithm with r = 0.97 and RMSE = 0.6°C (n = 21). The content of the water vapor content remained in the

87

range where the algorithm performs best, below 3 g.cm^{-2}. The following linear regression equation was derived between satellite and *in situ* sub-surface temperatures.
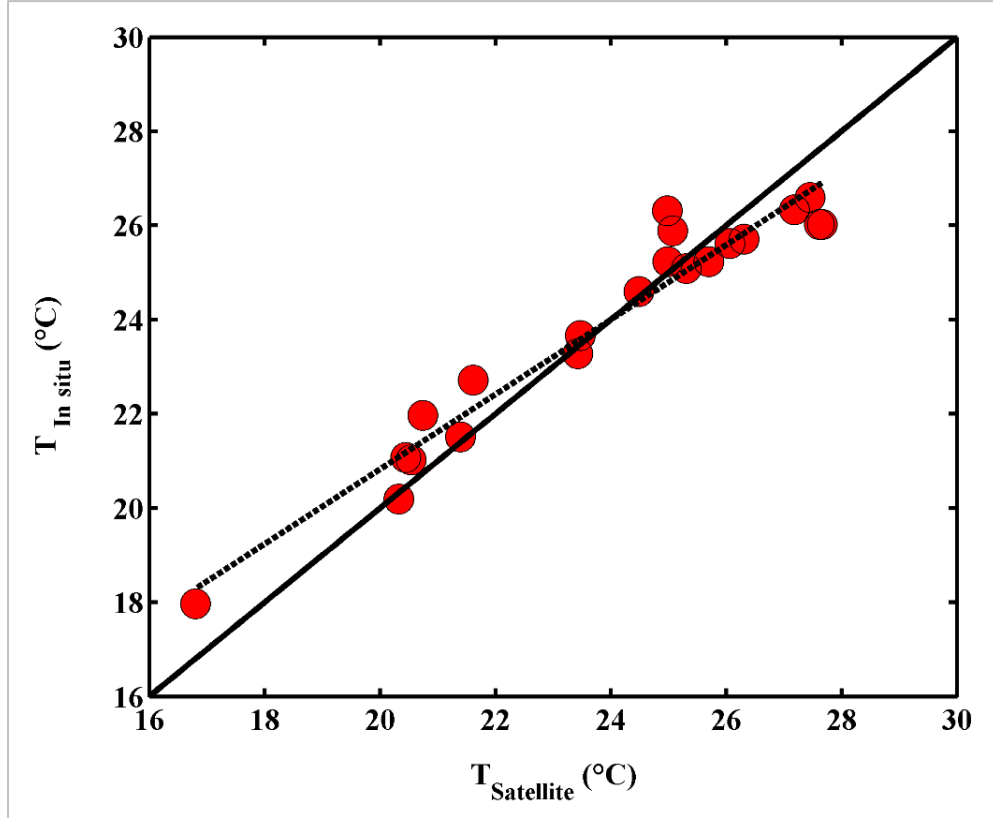
$$T_{In\ situ} = 0.793\ T_{Satellite} + 4.95 \qquad\qquad 35$$

Figure 29: Subsurface temperature measurements at the three monitoring sites ($\boldsymbol{T_{In\ situ}}$) versus Landsat 8 TIRS data after atmospheric correction with the single channel algorithm ($\boldsymbol{T_{Satellite}}$) in 2017 ($n = 21$). The dashed line represents the linear regression (Eq. 35).

After the correction of skin satellite temperatures with this linear regression, they were used as a proxy of surface bulk temperatures for comparison with the hydrodynamic model. The temporal evolution of these corrected satellite temperatures overall fits well with measured temperatures as shown in Figure 30a-c. Considerable discrepancies between satellite and measurements only occurred on 16/08/2017, by around 2°C.
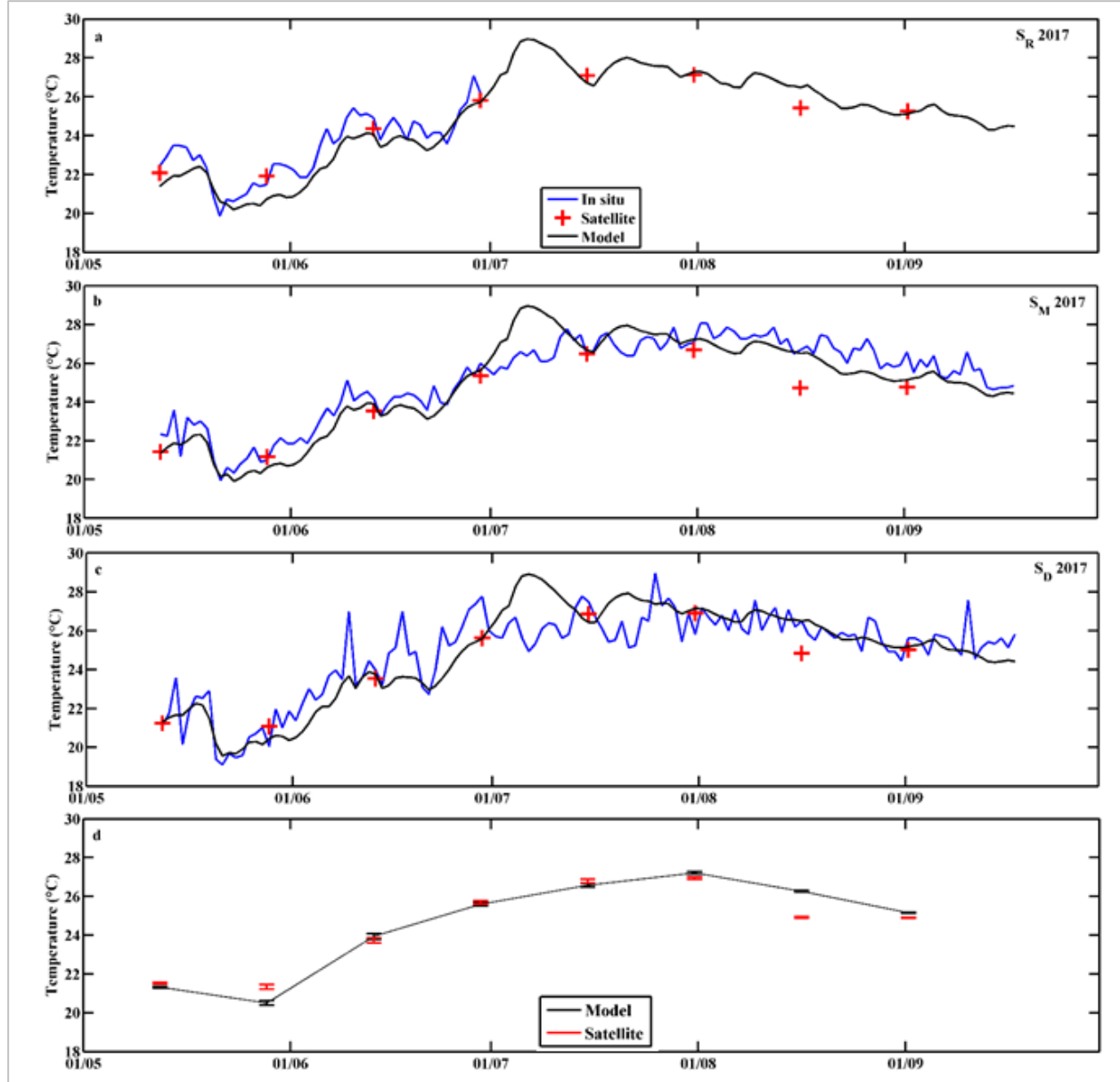
Figure 30: Surface temperature derived from Landsat 8, *in situ* measurements and the Delft3D-Flow model for sites S_R (Figure 30a), S_M (b) and S_D (c) on dates of Landsat 8 overpasses in 2017 at Karaoun Reservoir. d: means and standard deviations (SD) of model simulations and of satellite temperatures, after atmospheric correction and adjustment with measurements. Date format is day / month.

5.2.2. *Analysis of temperature at the reservoir surface in satellite and model maps*

Surface temperature maps were derived from corrected satellite data and from model simulations in 2017 on dates of Landsat 8 overpasses (Figure 31, Figure 32). The surface mean and the standard deviation of temperature on model and satellite maps for each overpass are also shown in Figure 30d. Satellite maps showed the expected seasonal variations in water temperature. Surface temperature increased gradually along the summer season with highest values occurring in July

(Figure 31 and Figure 30d). The same evolution was also observed in the maps of simulated surface temperatures (Figure 32 and Figure 30d).

In order to analyze the surface temperature patterns in 2017, anomaly maps were plotted based, for each map, on the differences of each pixel temperature with the surface average as temperature reference (Figure 33). For each satellite overpass, the anomaly maps are presented for model simulations and for corrected satellite temperature. Satellite maps show small spatial heterogeneities, close to the sensor resolution.The standard deviation of temperature is narrower in the model than in the satellite images, typically by a third (Figure 30d). Warm waters are mostly located in the littoral zones. An East-West gradient appears on 12/05, 13/06 and 31/07, a South-North one on 28/05, 15/07 and 16/08, and warmer littoral zones around the lake on 29/06 and 01/09/2017. Regarding model maps, they exhibit a South-North gradient from 28/05 to 31/07. A slight West-East gradient may be seen on 13/06, and from 31/07 to 01/09, in a direction opposite to that on satellite maps for the two former dates.
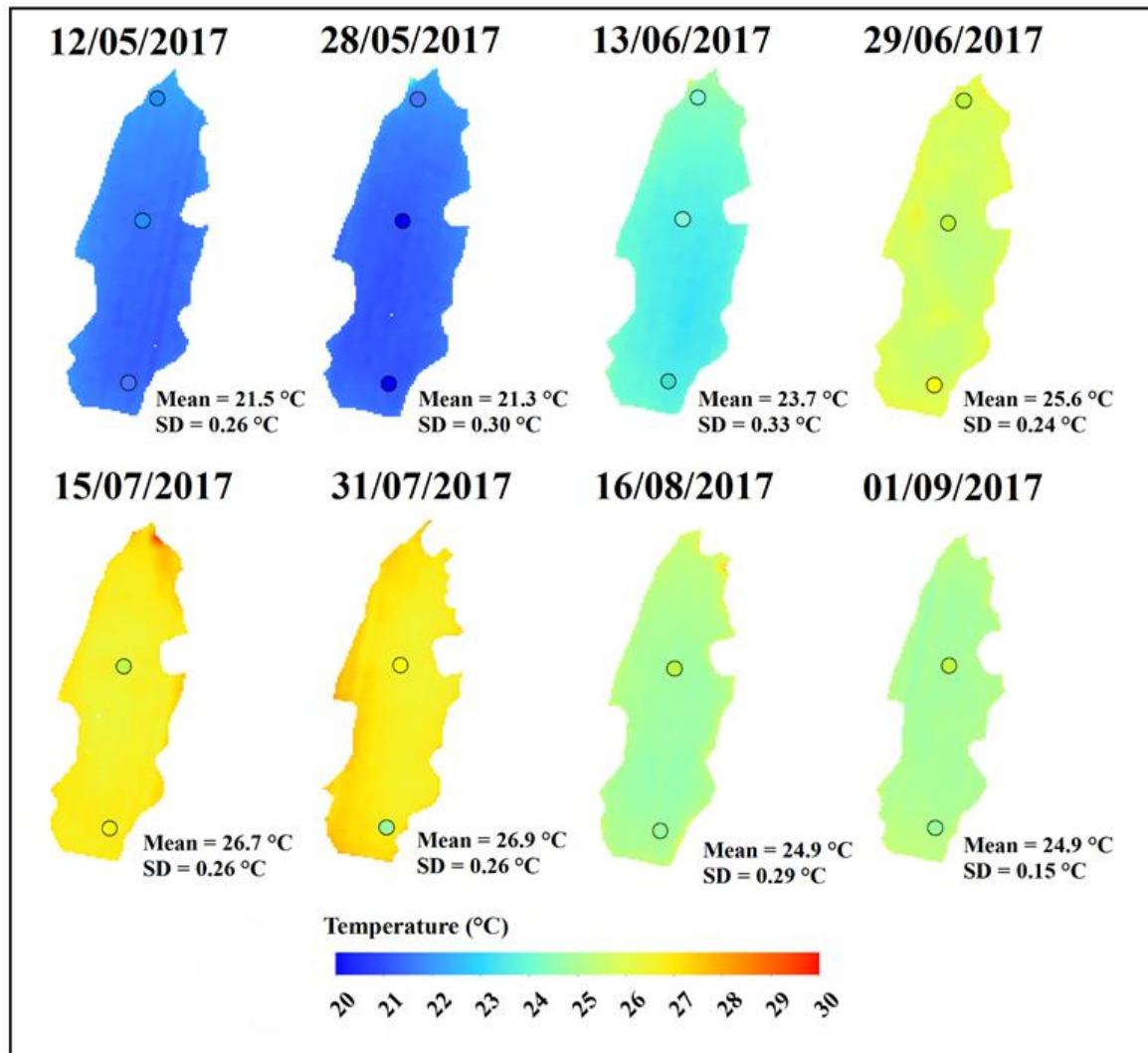
Figure 31: : Landsat 8 maps of water surface temperature in 2017, after atmospheric correction and adjustment with bulk measurements. Markers correspond to *in situ* subsurface measurements at sites S_R, S_M and S_D, with the same color scale as for satellite temperatures. The mean and standard deviation (SD) of surface temperature at the reservoir are indicated for each map.
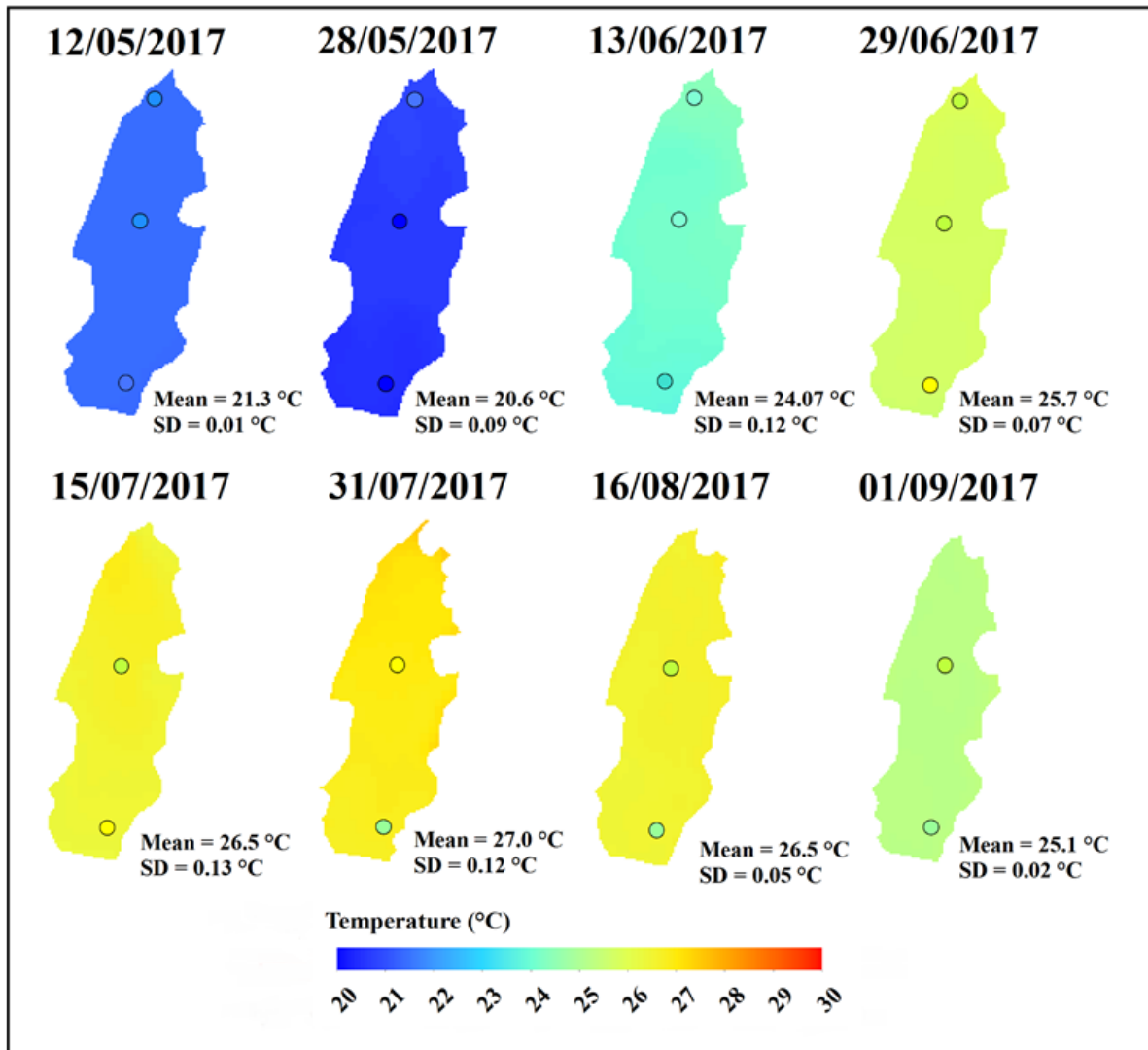
Figure 32: Water surface temperature maps generated from model simulations in 2017 on dates of Landsat 8 overpasses. The mean and standard deviation (SD) of surface temperature at the reservoir are indicated for each map.
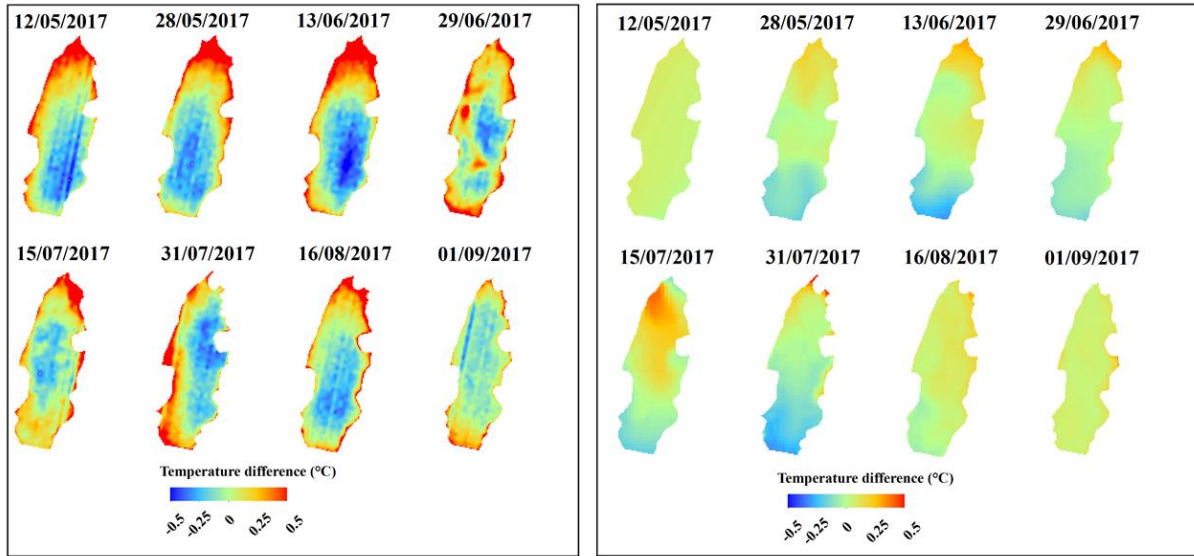
Figure 33: Anomaly maps between temperatures and the average value on each date for simulated (right) and corrected satellite surface temperature (atmospheric correction and adjustment with bulk measurements, left) in 2017.

5.3. Discussion

Hydrodynamic modelling has been seldom applied to reservoirs with considerable water level fluctuations between the wet and dry seasons in semi-arid climates (Ma et al. 2008). In this section the performance of the hydrodynamic model, the agreement between satellite and measured temperatures and the temperature spatial distribution in model and satellite maps are discussed.

5.3.1. Model simulations and in situ measurements

Water level fluctuations

At Karaoun Reservoir, the Delft3D-Flow model simulated the water level drawdown from July 01 to November 21 2012 and from May 12 to September 18 2017. The RMSEs were of 0.2 m for a 15 m decrease in 2012 (*n* = 33) and 0.1 m for an 8 m decrease in 2017 (*n* = 130), i.e. below 2% absolute error. The discrepancy during fall 2012 can be attributed to the more imprecise bathymetry in the lower part of the reservoir. Applying the 1D vertical model DYRESM to Karaoun Reservoir, a RMSE around 0.5 m for a level variation of 25 m (2% error) was obtained for the entire years 2010, 2011 and 2012 (Fadel et al., 2017). Applying another 1DV model, the General Lake Model (GLM) to Serra Azul Reservoir in Brazil from 2011 to 2016, a RMSE of 0.74 m (*n* = 1997) for a level variation of 22 m (3% error) was obtained (Soares et al., 2019). This demonstrates that the Delft3D-Flow model represents very well the large water level drawdown in reservoirs, here in a Mediterranean climate context.

Large fluctuations in the water level strongly influence the thermal regime of reservoirs. These include changes in mixing and stratification (Soares et al., 2019), and consequently in the water quality in reservoirs (Wang et al., 2012). Deep withdrawals at Sejnan Reservoir (Tunisia)

weakened the thermal stratification, increased the thickness of the metalimnion and intensified the hypoxia (Zouabi-Aloui et al., 2015). A decrease in the water level by 11 m between July and October at Arancio reservoir (Italy, maximum depth of 30 m) caused the elimination of the thermocline in mid-summer (Naselli-Flores & Barone, 2003). Therefore, obtaining a good model representation of the water level is crucial to capture an accurate thermal behavior of reservoirs.

Water temperature and thermal stratification

The 3D hydrodynamic model successfully reproduced the thermal regime exhibited by high frequency measurements (30 min) at Karaoun Reservoir. The model was able to capture the strong thermal stratification in summer, a period of great interest since it features intense blooms of cyanobacteria. During this period in 2012 and 2017, wind speeds were low and did not exceed 5 $m.s^{-1}$ (Figure 14) thus allowing the persistence of the thermal stratification. As withdrawals occur at the reservoir bottom (49 m depth) they did not erode the thermal stratification. Temperatures were overestimated in the epilimnion for 2012 and 2017 (Figure 28), as was already observed for 2012 with the 1D model DYRESM (Fadel et al., 2017). Overall, the model simulated well water temperature at different depths during these stratified conditions. Over the whole vertical profile, simulated temperatures are more horizontally homogeneous than measurements (Figure 27c-f). More precisely, the measured variability of subsurface temperature is higher at site S_D than at site S_M and S_R, whereas it is more spatially homogeneous in the model (Figure 30a-c). Part of this variability can be explained by the low accuracy of the temperature sensors used in 2017 (around 0.5°C). But the most probable reason comes from the uniform meteorological forcing from a distant weather station (40 km). An alternative would be to use a weather reanalysis like the ERA interim dataset of the European Centre for Medium-Range Weather Forecasts, but its resolution (80 km with a 12 h time step) is not sufficient as opposed, for example, to COSMO-1 reanalysis (1.1 km and hourly) used for Lake Geneva by Baracchini et al. (2020). The model temperature overestimation in July, in surface layers (Figure 30a-c) may be due to temporary meteorological differences between the reservoir and the distant weather station.

Even if the horizontal surface temperature heterogeneity is not fully represented, the errors over the vertical profiles, at each measurement sites remain rather low. RMSEs ranged between 0.5 and 1.1°C in the epilimnion (0.2 – 7 m) and between 0.5 and 1.9°C in the metalimnion (10 – 16 m). These values are comparable to the results of other 3D hydrodynamic models, e.g., 0.6 to 3.9°C for surface temperatures and 0.9 to 5.3°C for bottom temperatures in Alqueva reservoir, Portugal, with the RMA10 model (Lindim et al., 2011).

The largest temperature deviations at the surface and at the thermocline (Figure 28) are very comparable to the other results with the same model, in Lake Constance (Wahl & Peeters, 2014) and in Nam Theun Reservoir, Laos (Chanudet et al. 2012). Delft3D-Flow is therefore considered to perform well at Karaoun Reservoir with comparable discrepancies.

5.3.2. Landsat 8 water surface temperature

At Karaoun Reservoir, satellite surface temperatures after atmospheric correction with the single-channel algorithm (Jiménez-Muñoz et al., 2014) match with measurements (Figure 31). This shows that the algorithm is reliable for deriving surface temperature over freshwater systems. The exceptional underestimation by around 2°C on August 16 2017 may come from an inaccurate water content which affected the atmospheric correction. The values of the statistical indicators are comparable with those found in other studies. In Karaoun Reservoir, the RMSE of 0.6°C (n = 21) is considered acceptable once compared with 1.2°C (n = 27) found for Embalse del Rio Tercero reservoir, Argentina (Lamaro et al., 2013) and with 1.7°C (n = 14) found for Bimont and Bariousses Reservoirs, France (Simon et al., 2014). The single-channel algorithm provides valuable additional data when *in situ* measurements are not available, especially in regions where data are scarce.

Among the several error sources in surface temperature retrieval, the main one comes from the difference between bulk and skin temperature (Prats et al., 2018). At Karaoun Reservoir, bulk temperature was measured at 20 cm below the surface. In the literature, the bulk temperatures are usually measured over depths ranging from a few centimeters to several meters, depending upon the depth of the surface mixed layer (Schmidt et al., 2018). At least during morning overpasses, bulk water temperatures can be considered representative of skin water temperatures (Schneider & Mauser,1996; Huang et al., 2017). Nevertheless, in order to obtain a proxy of bulk temperatures, skin temperatures were adjusted with bulk measurements with a linear regression, for a more representative comparison with model results.

Using a 3D hydrodynamic model, remote sensing temperature can be assimilated with *in situ* measured vertical profiles and hence used as initial conditions for the entire reservoir domain. However, this approach is only reported in few studies and its effect on the performance of the model is seldom addressed. On the Eagle Creek Reservoir, USA, Landsat surface temperature data and *in situ* measurements were assimilated as initial conditions into a 3D hydrodynamic model (EFDC) from August to October 2008 (Babbar-Sebens et al., 2013). After adjusting skin temperatures according to Javaheri et al. (2016) before their assimilation to the EFDC model, the errors were reduced by 91% between adjusted skin temperatures and model surface temperatures (from 5.6 to 0.51°C) and by 27% for water column temperatures (from 1.95 to 1.42°C). Assimilation of satellite data into hydrodynamic models, previously calibrated with bulk measured temperature, significantly improves the simulation results, principally in the surface layer.

5.3.3. Spatial distribution of surface temperature

Maps of model and satellite temperatures at Karaoun Reservoir were produced and compared. The horizontal distribution of satellite temperatures was shown to be partly reproduced by the model. Both model and satellite maps displayed relatively low horizontal heterogeneities, typically lower than 1°C and more pronounced in satellite maps. The model qualitatively reproduced most of the temperature gradients from South to North, but not the gradients from East to West. It could not reproduce the often warm waters close to the dam.

Lower heterogeneity in simulated temperature maps than in satellite maps were already observed by Allan et al. (2016) who compared 3D ELCOM simulations to Landsat 7 images on Lake Rotoehu in New Zealand. The authors interpreted the differences with the quality of the meteorological forcing, especially air temperature and wind speed and direction. In Karaoun Reservoir located in a relatively narrow valley, the low simulated heterogeneities probably originate also from the uniform meteorological forcing, from the distant weather station.

6. Chapter 6: 3D ecological modeling at Karaoun Reservoir

In this chapter, the results obtained with the 2012, 2017 and 2018 simulations of phytoplankton biomass in terms of *Chl-a* concentration and nutrients concentrations (NO_3^- and PO_4^{3-}) are presented and discussed. The adopted methodology and the description of the ecological model are provided in section 2.7. Model simulations are analyzed and compared to *in situ* measurements. Results about remote sensing of transparency and *Chl-a* in 2017 and 2018 are also provided and discussed. Further the performance of the model is assessed. Remote sensing and model maps of *Chl-a* concentrations are qualitatively compared.

6.1. Remote sensing of *Chl-a* and transparency

6.1.1. Transparency

In order to obtain the approximate depth at which satellite *Chl-a* values are being delivered, transparency (Secchi depth) values were derived from remote sensing data by developing an empirical band ratio algorithm from Sentinel-2 data. In order to obtain the best performing algorithm, an empirical approach was adopted between atmospherically corrected reflectance values of MSI bands and transparency measurements acquired in 2017 and 2018 over dates of Sentinel-2 overpass. Amongst several band combinations, for the calibration subset ($n = 7$), the best band ratio found in good correlation with measurements was that of Band 8 (B8, NIR) over Band 1 (B1, coastal aerosol) (Table 3) with $R^2 = 0.84$ and RMSE = 0.14 m. The resulting linear regression equation is as follow:

$$y = -1.0795 \, \frac{B8}{B1} + 1.9077 \qquad\qquad 36$$

A relatively good agreement was obtained between transparency estimations from the band ratio algorithm and measurements with a R^2 of 0.74 (Figure 34). Although the algorithm yielded acceptable results, limitations in regards to in situ data availability and thus the transparency measurement range should be taken into consideration.

This equation was further applied to generate maps of transparency in 2017 and 2018 as shown in Figure 35 and Figure 36 where mean values ranged between 0.14 and 1.5 m and 0.25 and 1.43 m respectively.
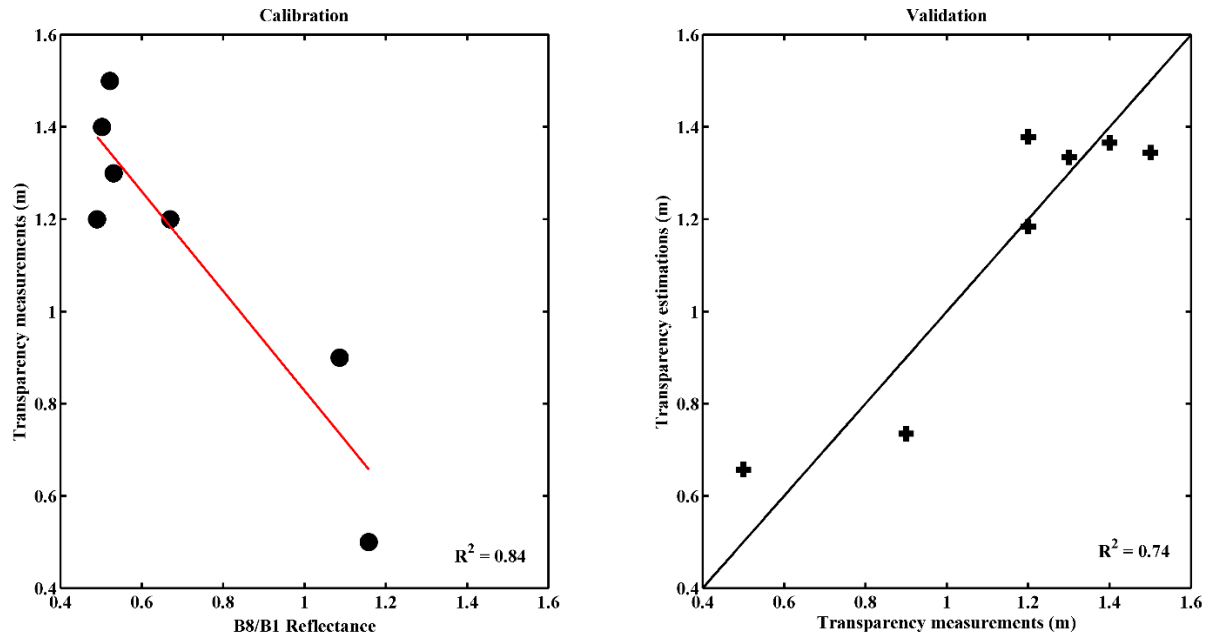
.

Figure 34: Linear relationship between transparency measurements and the reflectance of B8/B1 (left). Correlation between transparency measurements and estimations predicted from (Eq. 36) (right).
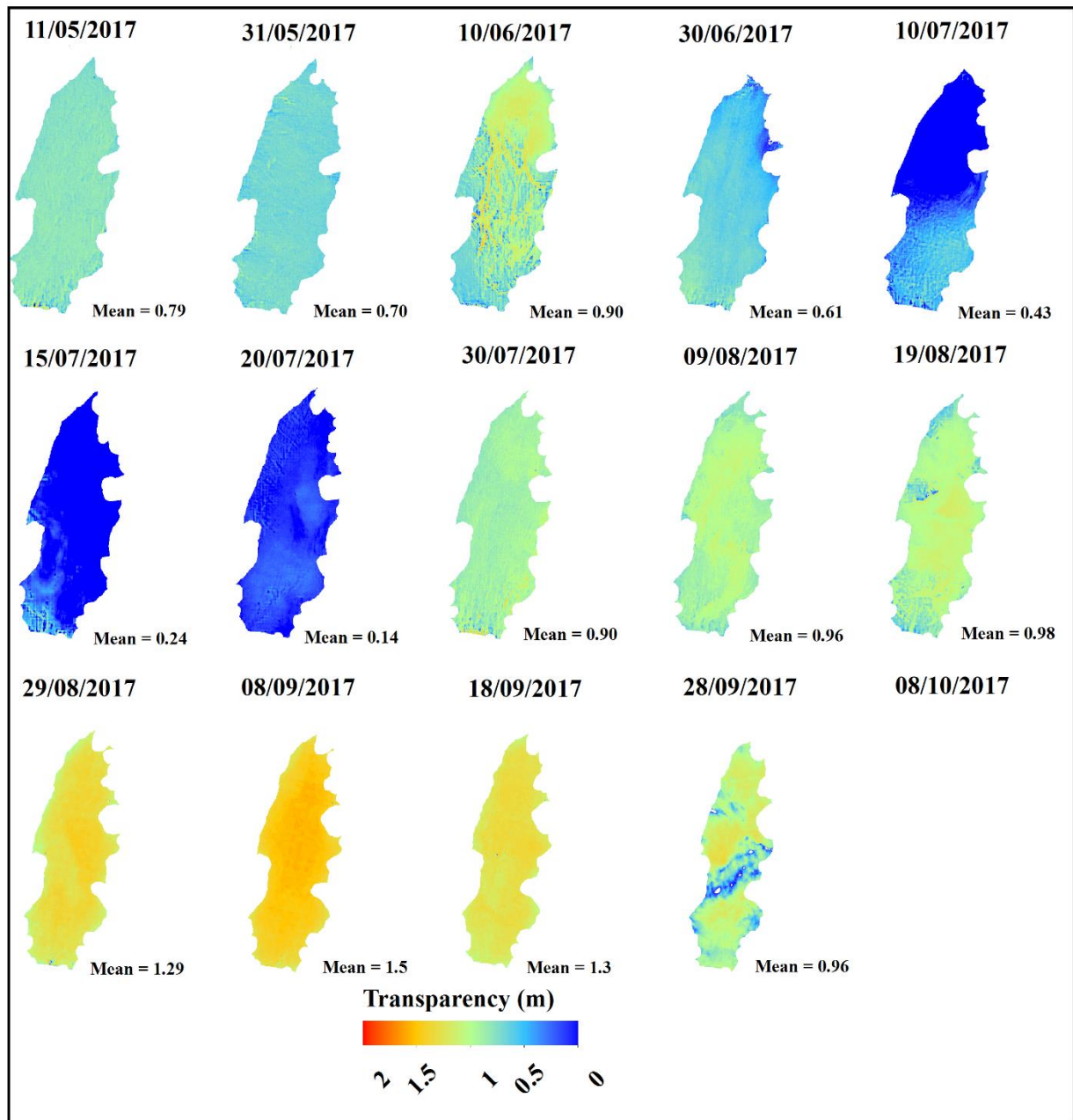
Figure 35: Sentinel-2 maps of transparency in 2017.
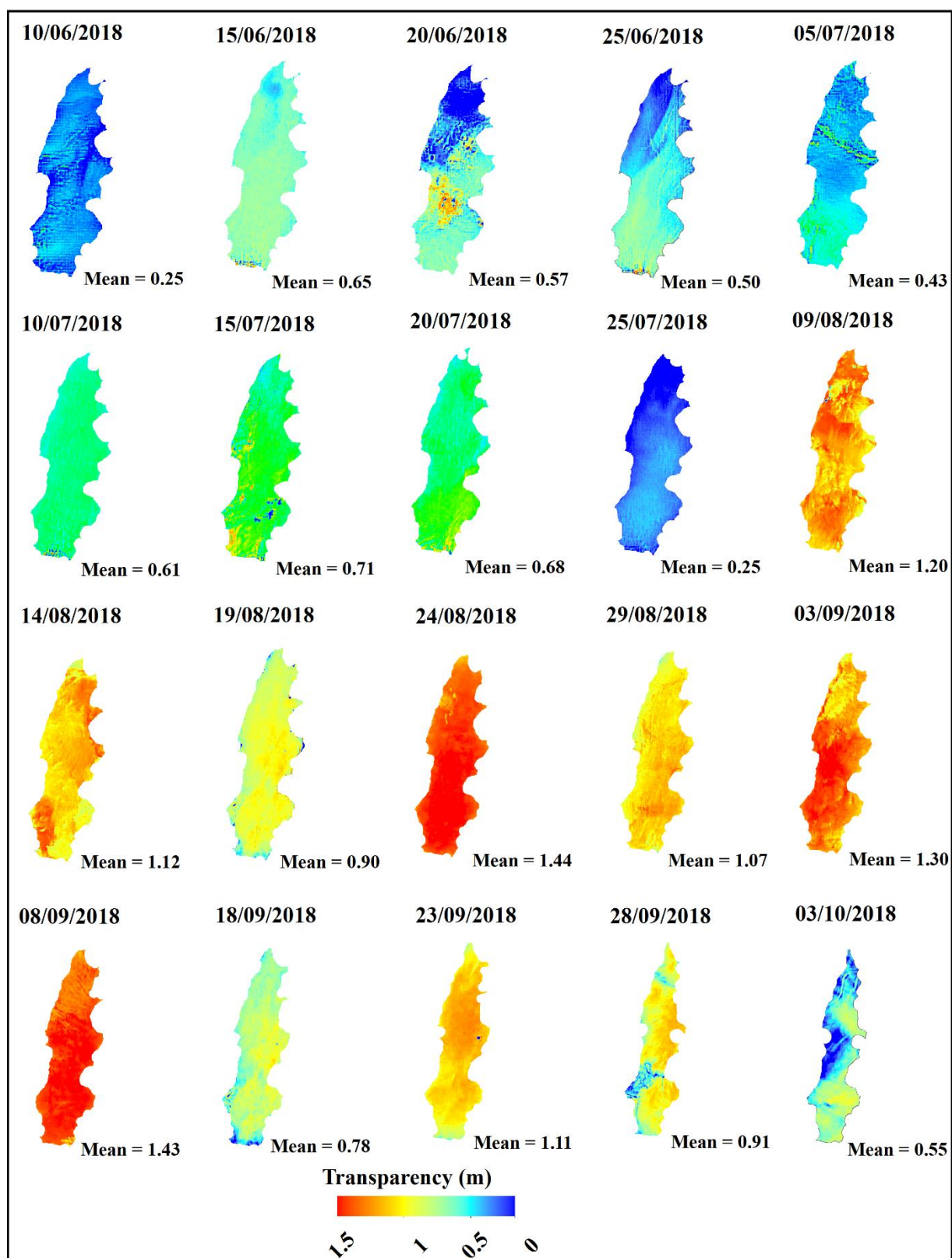
Figure 36: Sentinel-2 maps of transparency in 2018.

6.1.2. Chl-a

The distribution of *Chl-a* concentrations obtained from Sentinel-2 images in 2017 and 2018 is spatially variable as shown in Figure 37 and Figure 38 respectively. The mean values ranged between 33.66 – 149.58 mg/m^3 in 2017 and between 22.00 – 77.43 mg/m^3 in 2018.

In 2017, *Chl-a* displayed a wide range of concentrations (Figure 37) with highest values (> 200 mg/m^3) occuring on the 10th and 15th of July and on the 8th and 10th of October mostly in the Northern part of the reservoir, close to the mouth of the Litani river. In June, high *Chl-a* concentrations occurred in the Northern and Eastern parts of the reservoir. On the 9th of August and the 8th and 18th of September, *Chl-a* was highest at the opposing Northern and Southern regions. The spatial distribution on the 19th and 29th of August exhibited a similar pattern in which aggregations are mostly found on the Northern part of the reservoir as well as along the Western and central regions. On the 28th of September, high *Chl-a* concentrations are mostly found in the centre and south of Karaoun Reservoir near the dam.

In 2018, *Chl-a* concentrations were lower (< 250 mg/m^3) with highest values occuring on the 20th and 25th of June, on the 5th of July and in October. In June and July, these concentrations were mostly located in the Northern part of the reservoir whereas in October they were more distributed along the entire reservoir (Figure 38).

The comparison between Sentinel-2 *Chl-a* and transparency maps in 2017 and 2018 revealed a consistent pattern where the highest *Chl-a* concentrations coincided with the lowest transparency values and exhibited a similar spatial distribution. For instance, in 2017 on the 10th of July where the highest *Chl-a* concentrations occurred in the Northern part of the reservoir, the corresponding transparency values were the lowest in the same part of the reservoir.
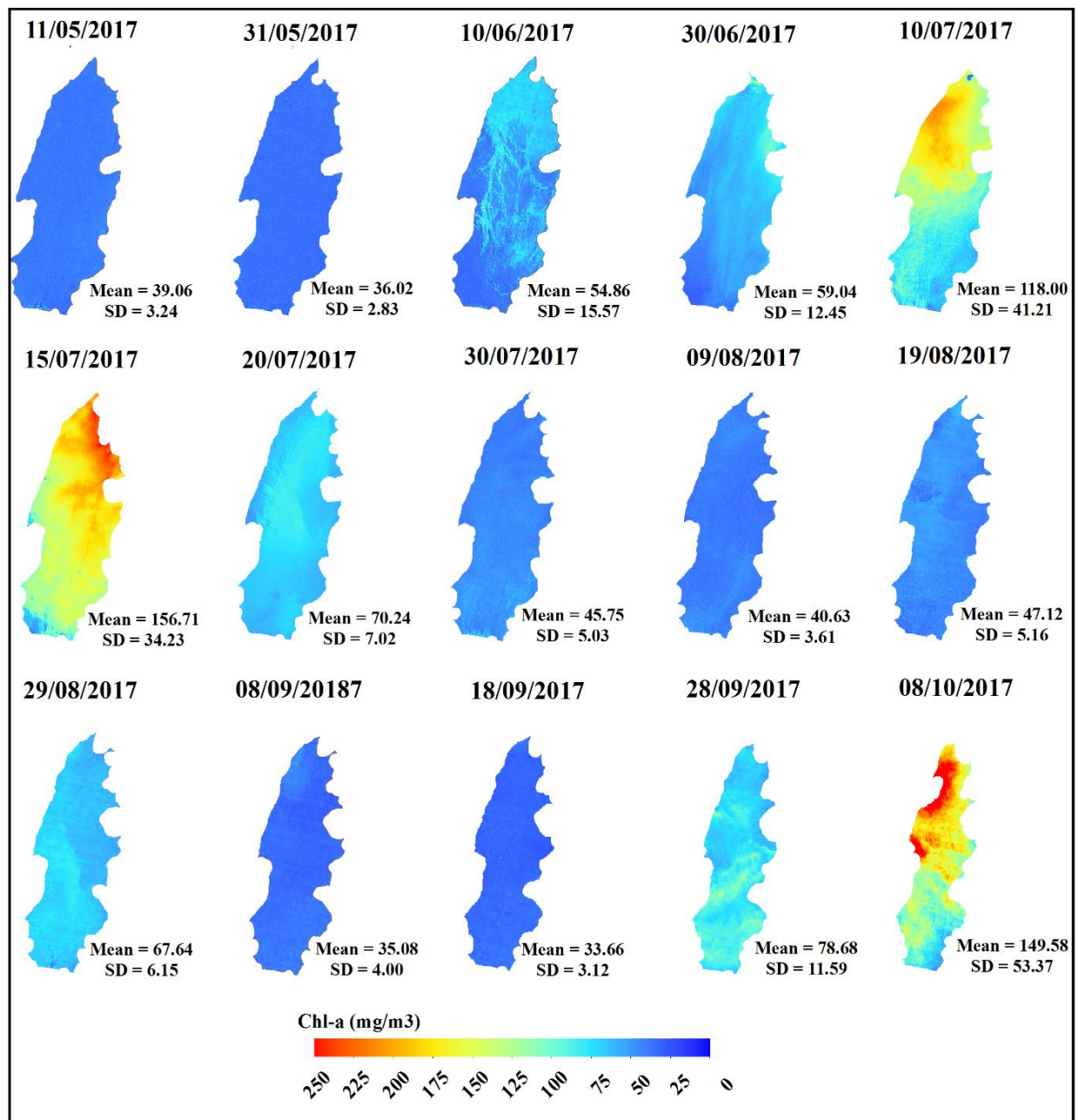
Figure 37: Sentinel-2 maps of *Chl-a* concentrations in 2017. The mean and standard deviation (SD) of *Chl-a* concentrations are indicated for each map.
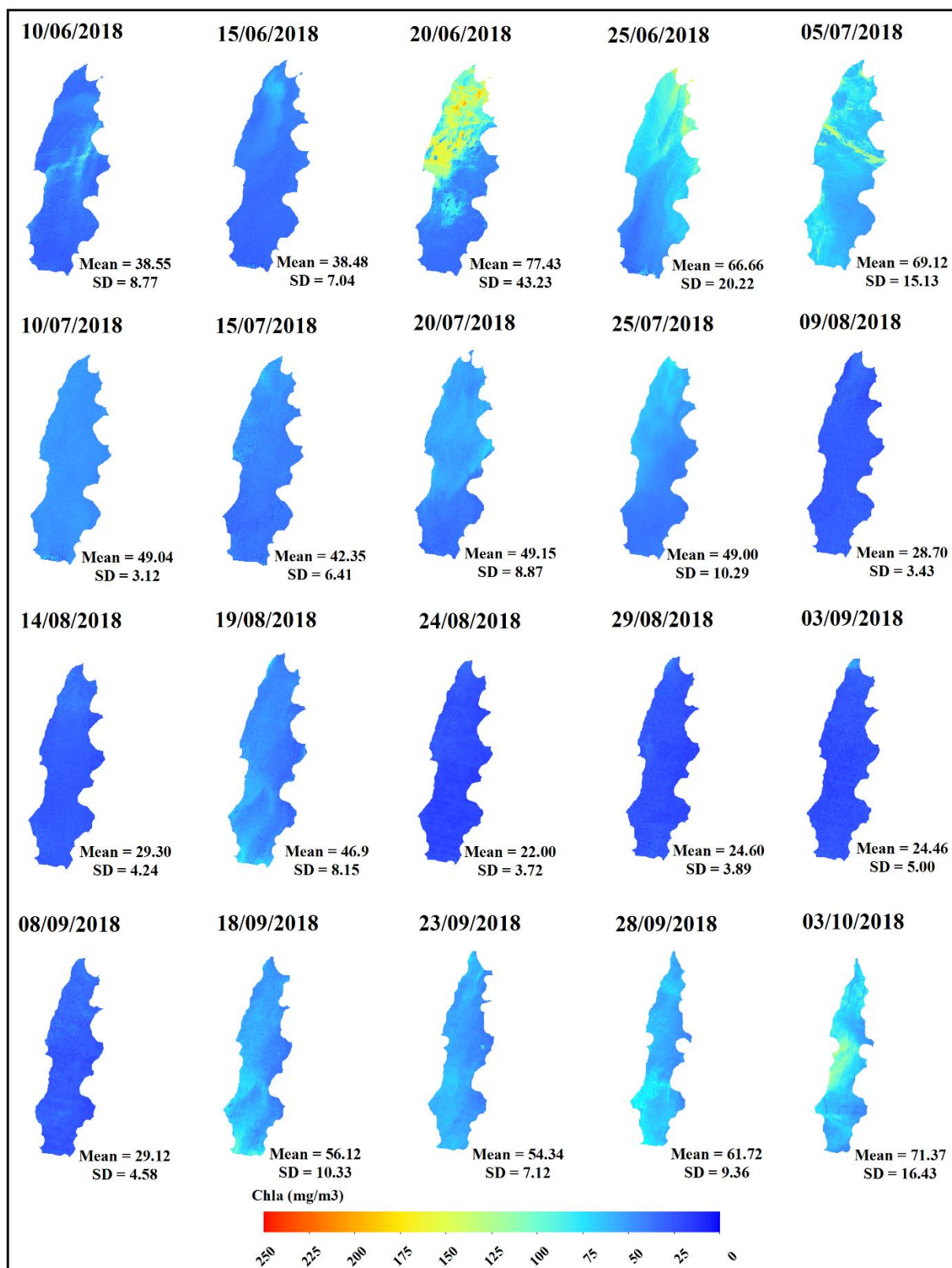
Figure 38: Sentinel-2 maps of *Chl-a* concentrations in 2018. The mean and standard deviation (SD) of *Chl-a* concentrations are indicated for each map.

6.2. Ecological modeling

Simulations indicate that the model represents well the seasonal variability of *Chl-a* over the monitoring sites. Simulations and measurements of phytoplankton biomass in terms of *Chl-a* concentration in 2012 at site S_D and in 2017 and 2018 at sites S_R, S_M and S_D represented respectively in Figures 39-41. Comparisons between measured and simulated nitrate and orthophosphate concentrations in 2018 are also shown in Figure 41.

In 2012 and at 1 m depth, simulated *Chl-a* shows a similar trend to that of measurements; concentrations increase between July and the beginning of September where the peaks are represented well (Figure 39). Concentrations then decrease from September onwards except for a peak in early October which does not correspond to measurements. Very high concentrations occur at 5 and 15 m depths where peaks exceed measurements yet a comparable evolution pattern is observed. The distribution of *Chl-a* concentrations in 2012 throughout the water column is comparable to the thermal stratification pattern (Figure 27). Between July and early September, thermal stratification is established and *Chl-a* becomes more concentrated in the epilimnion and much less in the hypolimnion. From September onwards the thermal stratification is disrupted and the water column becomes mixed. In this case, *Chl-a* distribution occurs uniformly along the water column.

In comparison to 2012, *Chl-a* concentrations are higher in 2017, exceeding 200 mg/m^3 (Figure 40 and Figure 41). In 2017, highest concentrations occur between the subsurface (0.5 m) and 2 m depth. Results show that the model was able to reproduce the increase in *Chl-a* concentrations between May and late July followed by a decrease from August onwards. A *Chl-a* peak in late June corresponding to a cyanobacteria bloom was correctly reproduced by the model at site S_M. However, simulation results present too early an onset of cyanobacteria development in late May (31st) when the model was dominated by cyanobacteria (Figure 18). Moreover, the model was not able to capture the peak of *Microcystis* in late July (27th). The distribution of *Chl-a* is also consistent with the existing thermal stratification (Figure 27) where concentrations tend to accumulate in the upper parts of the water column. Green algae were mostly present between May and June of 2017 (Figure 18). Simulation results show very low concentrations of green algae with highest values occurring in May 2017.

A similar trend to the 2017 algal development was observed in 2018 where the highest *Chl-a* concentrations observed in June, July were also shown in model simulations. The model also correctly predicted the decrease in these concentrations between August and early September, their increase between late September and early October and the higher *Chl-a* concentrations observed at site S_R in comparison to S_M and S_D.

In the model, NO_3^- and PO_4^{3-} are also well balanced with an acceptable representation of their vertical distribution. The decrease of NO_3 and PO_4^{3-} during algal development was overall well reproduced by the model in 2018 between the subsurface and 10 m. The model predicts higher NO_3^- concentrations at the three monitoring sites and lower PO_4^{3-} concentrations at S_R and S_M.

In 2018 and between the subsurface and 5 m depth, the model showed the presence of green algae with concentrations not exceeding 50 mg/m^3 which is not consistent with the microscopic identification of phytoplankton composition at least during the field campaigns (Appendix E: Ecological simulations). Diatoms and green algae do not grow during the simulations period (Appendix E: Ecological simulations) which is consistent with the available observations of phytoplankton species: the reservoir was mainly dominated by cyanobacteria (Figure 18).

In regards, to simulated DO concentrations (Figure 42), a reliable validation of the simulations was not possible due to the lack of measurements during the simulation periods. In 2017 and 2018, results show that simulated DO concentrations fluctuate with water temperature (Figure 27). The increase and decrease in concentrations is proportional to the evolution of *Chl-a* concentrations shown in Figure 40 and Figure 41.
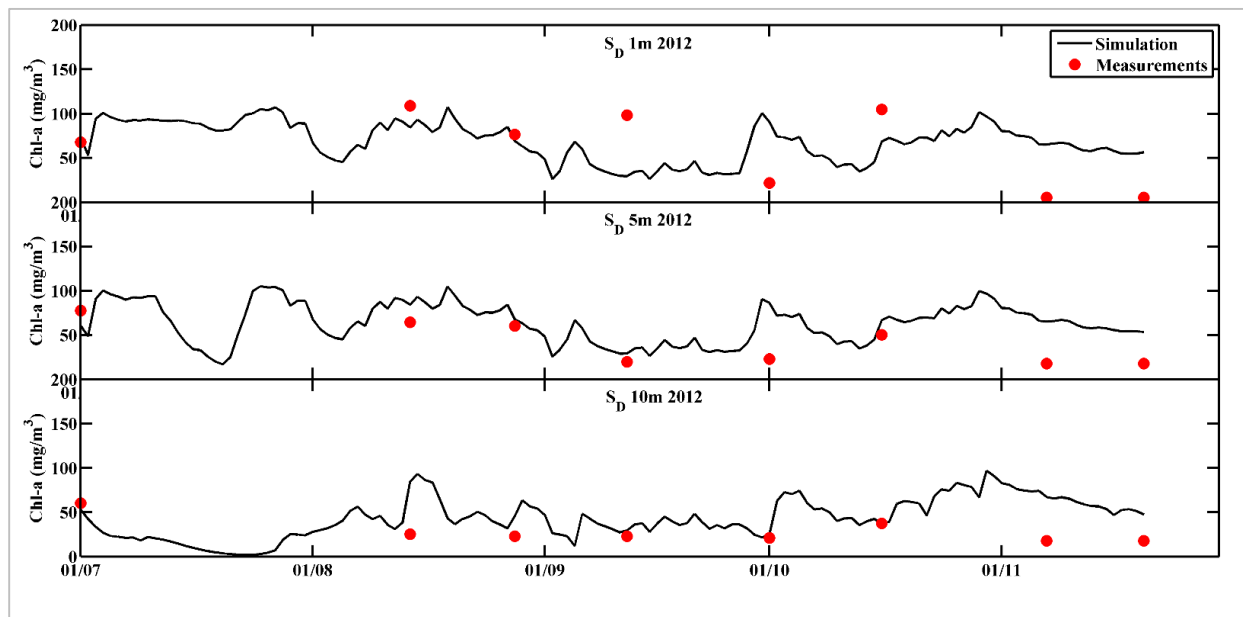
Figure 39: Simulated *Chl-a* concentrations in 2012 at site S$_D$. Red dots correspond to *in situ* measurements.
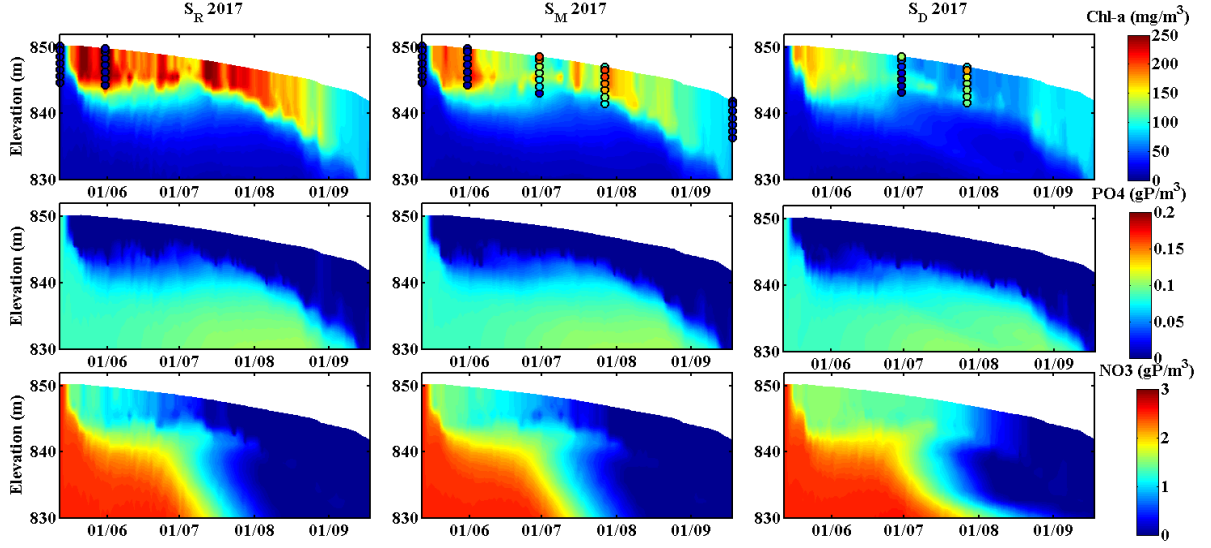
Figure 40: Simulated *Chl-a*, NO_3^- and PO_4^{3-} concentrations in 2017 at sites S_R, S_M and S_D. Markers correspond to *in situ* measurements.
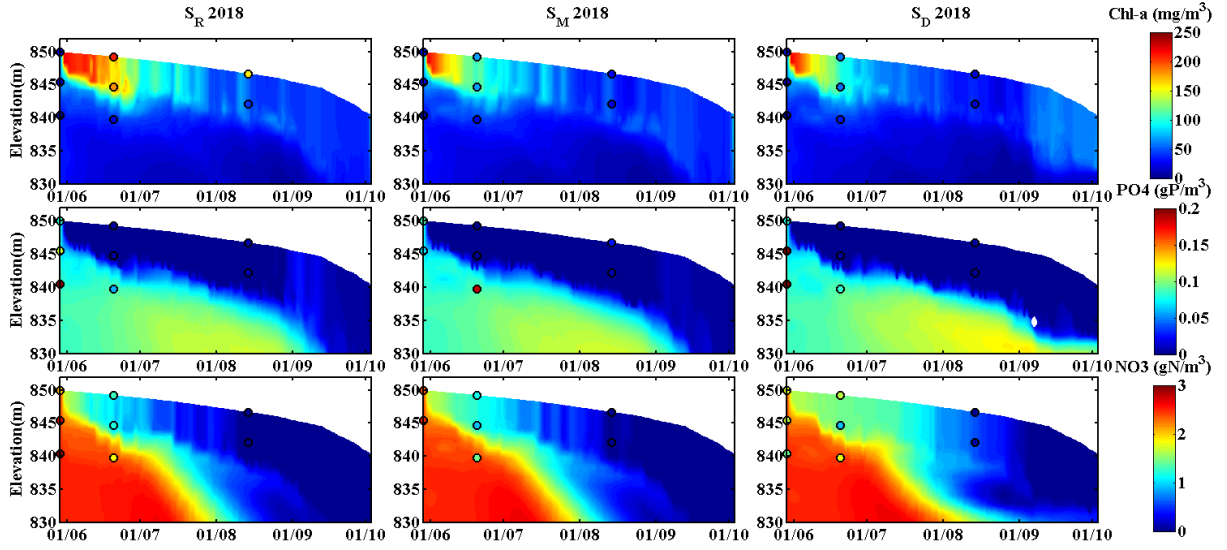

Figure 41: Simulated *Chl-a*, NO_3^- and PO_4^{3-} concentrations in 2018 at sites S_R, S_M and S_D. Markers correspond to *in situ* measurements.
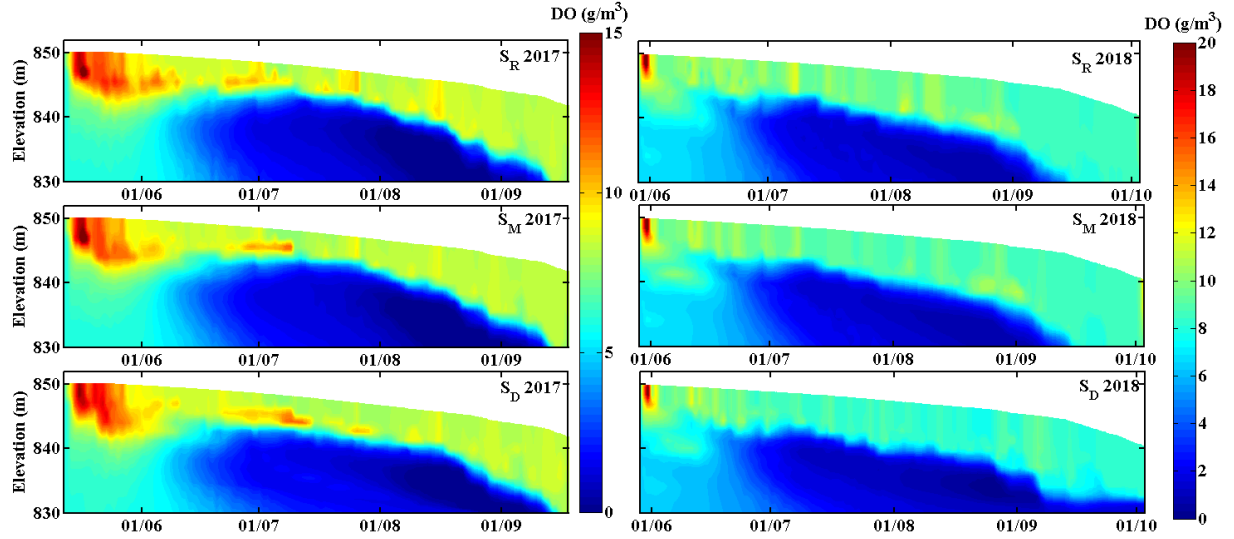
106

Figure 42: Simulated DO concentrations in 2017 and 2018 at sites S_R, S_M and S_D.

6.3. Model performance

The performance of the model was assessed qualitatively and quantitatively although in this study the latter is based on a small number of data compared to large lakes where measurements are available almost around the year.

Qualitatively, the model represented well the evolution and seasonal variation of phytoplankton biomass which was consistent with the thermal structure and composition of the phytoplankton community. The model correctly reproduced the observed phytoplankton blooms which were mainly composed of cyanobacteria and the following decrease in biomass. Although the model mostly overestimated *Chl-a* concentrations, it did represent the *Chl-a* peaks for instance in June of 2017 at site S_M, which is very important since it was mostly due to toxic cyanobacteria.

Quantitatively, the RMSE calculated between measurements and simulations of *Chl-a* concentrations in 2012 at S_D ($n = 24$) and in 2017 at S_M ($n = 28$) was acceptable and did not surpass 65 mg/m³ (Table 12). The RRMSE values also remained below 100 % with highest values occurring at deeper depths (10 m for 2012 and 5 m for 2017). Such values are considered acceptable and indicate a good performance of the model (Kaçıkoç & Beyhan, 2014, Soulignac et al., 2019). The discrepancies between observations and simulations, in particular the occasional overestimation of *Chl-a* concentrations, may be attributed to an approximate representation of the nutrient concentrations and influx from the Litani River due to the lack of measurements.

Table 12: Simulation performance indicators for *Chl-a* concentrations at the different depths at sites S$_D$ in 2012 and S$_M$ in 2017. Values from the second field campaign date in 2017 were not considered.

Depth (m)	S$_D$ 2012 (*n* = 24)			S$_M$ 2017 (*n* = 28)						
	1	5	10	0.5	1	2	3	4	5	6
RMSE (mg/m³)	46.90	32.80	30.53	54.76	36.78	41.06	66.03	64.01	47.20	44.66
RRMSE (%)	45.29	54.72	71.82	62.13	41.80	45.06	79.46	82.53	86.86	40.17

The performance of the ecological model of the Delft3D software has been rarely evaluated and it was generally applied to inland waters in particular to reservoirs. Soulignac et al. (2019) used this ecological model on Lake Geneva in order to assess its ecological status and sampling representativeness. Over four simulated years, they found that the model reproduced well the seasonal variability of *Chl-a* with RRMSE between 30 and 100 %. Nevertheless, the model failed to reproduce the dynamics and development of certain taxa. In another study, Kaçıkoç & Beyhan, (2014) used the Deflt3D model to determine the impact of pollution loads on the water quality of lake Egirdir, Turkey where the RRMSE for *Chl-a* also did not surpass 100%. However, they attributed a poor performance of the model in simulating *Chl-a* to an underrepresentation of algae groups since they had a single group in their model configuration.

6.4. Satellite and model simulations of *Chl-a* concentrations

Simulated maps of *Chl-a* concentrations in 2017 and 2018 are compared to Sentinel-2 maps on Figure 43 and Figure 44 with the mean and standard deviation shown for each overpass. The *Chl-a* differences between model simulations and satellite maps in 2017 and 2018 are presented in Figure 45 and Figure 46 respectively. In both simulated and Sentinel-2 maps, *Chl-a* exhibits spatial variability, but it is more pronounced in the former. The model overall provides an acceptable *Chl-a* concentration range. In both years, the standard deviations (SD) were narrower and the mean *Chl-a* values were mostly lower in Sentinel-2 maps.

In 2017, from May to mid-August, a strong overestimation is shown at the north of the reservoir with considerable *Chl-a* differences (Figure 45). The agreement between Sentinel-2 values and model results is better in the south of the reservoir. On two dates, the 10th and 15th of July, the highest concentrations in the north of the reservoir are close in the satellite and model maps. From the end of August to October, the lower *Chl-a* concentrations are in better agreement with satellite values.

In 2018, a strong overestimation of *Chl-a* concentration by the model appeared again at the north of the reservoir from June to July (Figure 46). In the South of the reservoir, the agreement between Sentinel-2 values and model results is more acceptable. From late August till October, the low simulated *Chl-a* concentrations are close to the satellite values with differences around 25 mg/m³.
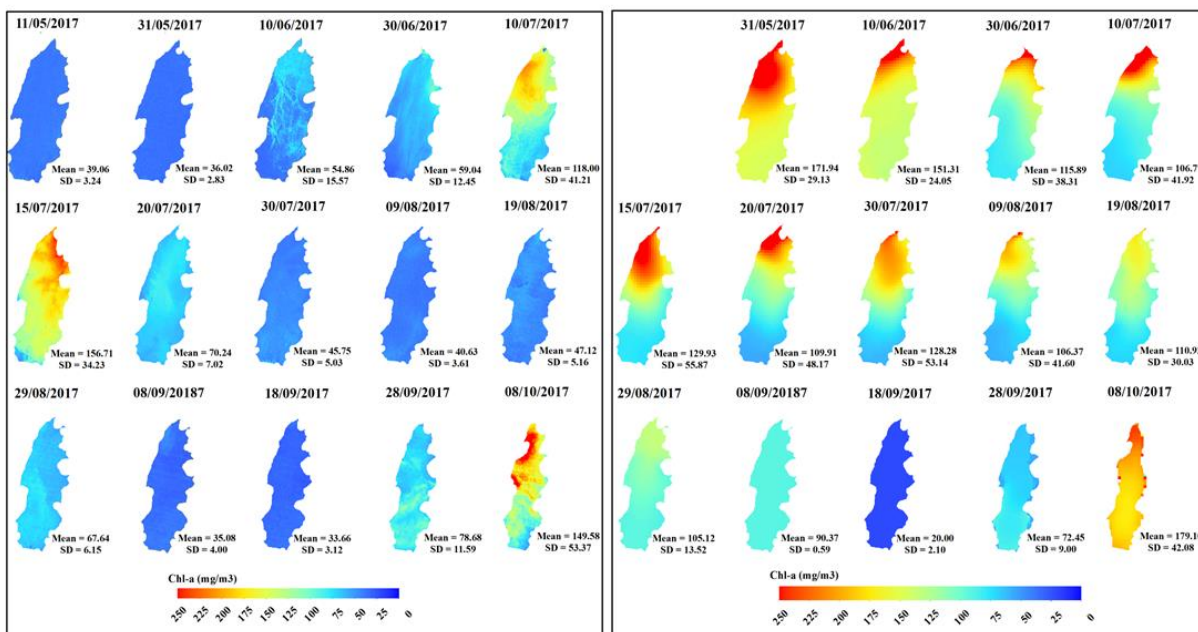
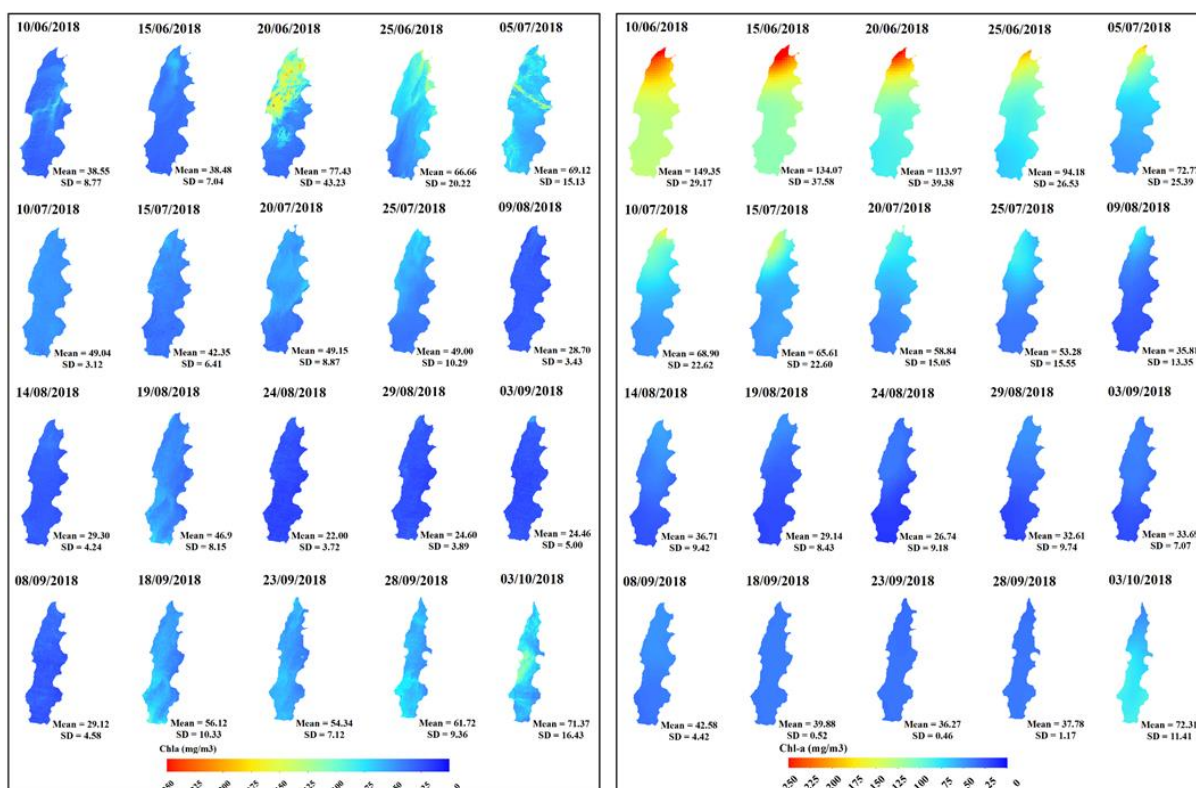**Figure 43:** Maps of Sentinel-2 (left) and simulated (right) *Chl-a* concentrations in 2017.

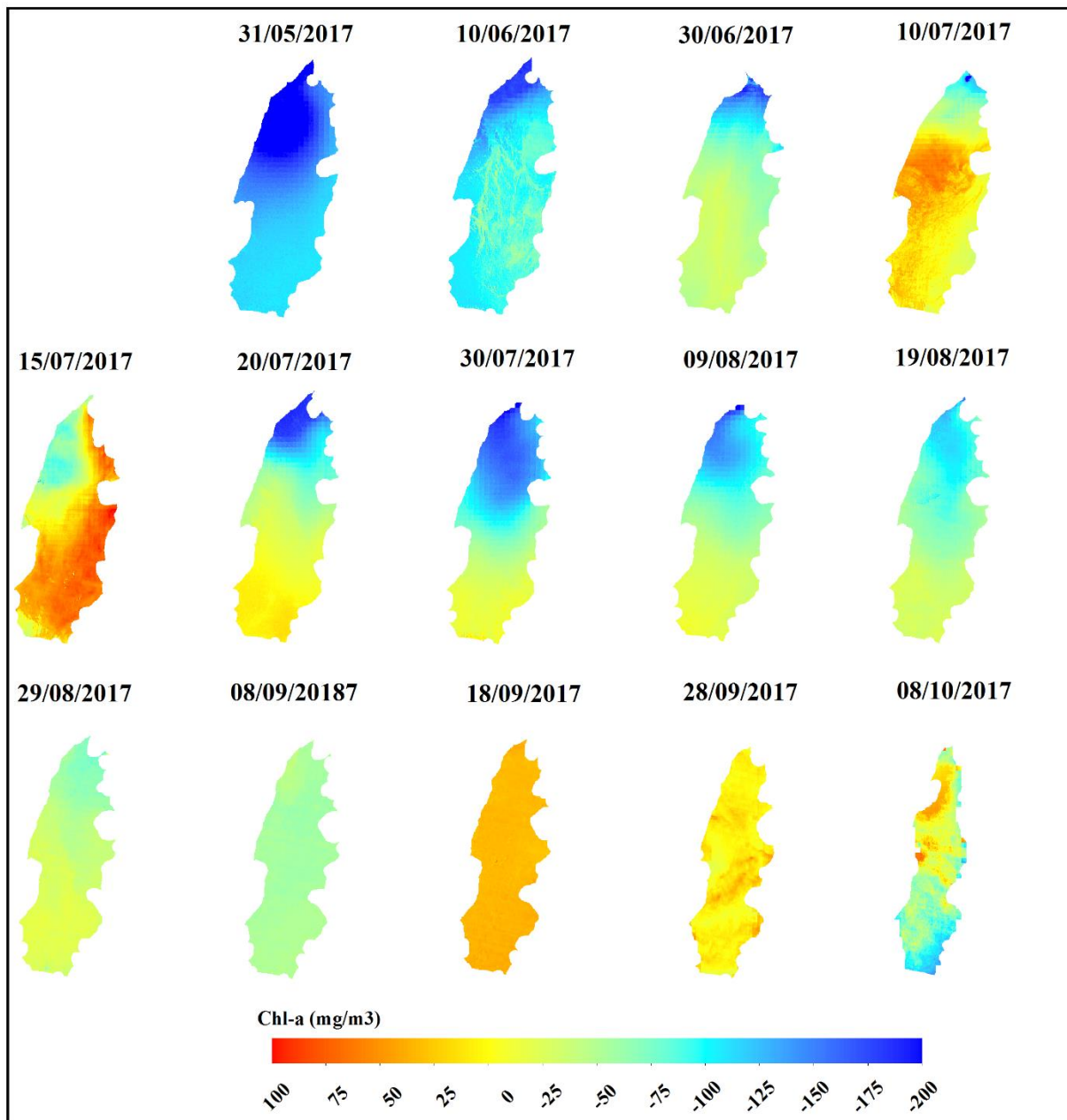**Figure 44:** Maps of Sentinel-2 (left) and simulated (right) *Chl-a* concentrations in 2018.

Figure 45: Differences between simulated and Sentinel-2 *Chl-a* concentrations in 2017.
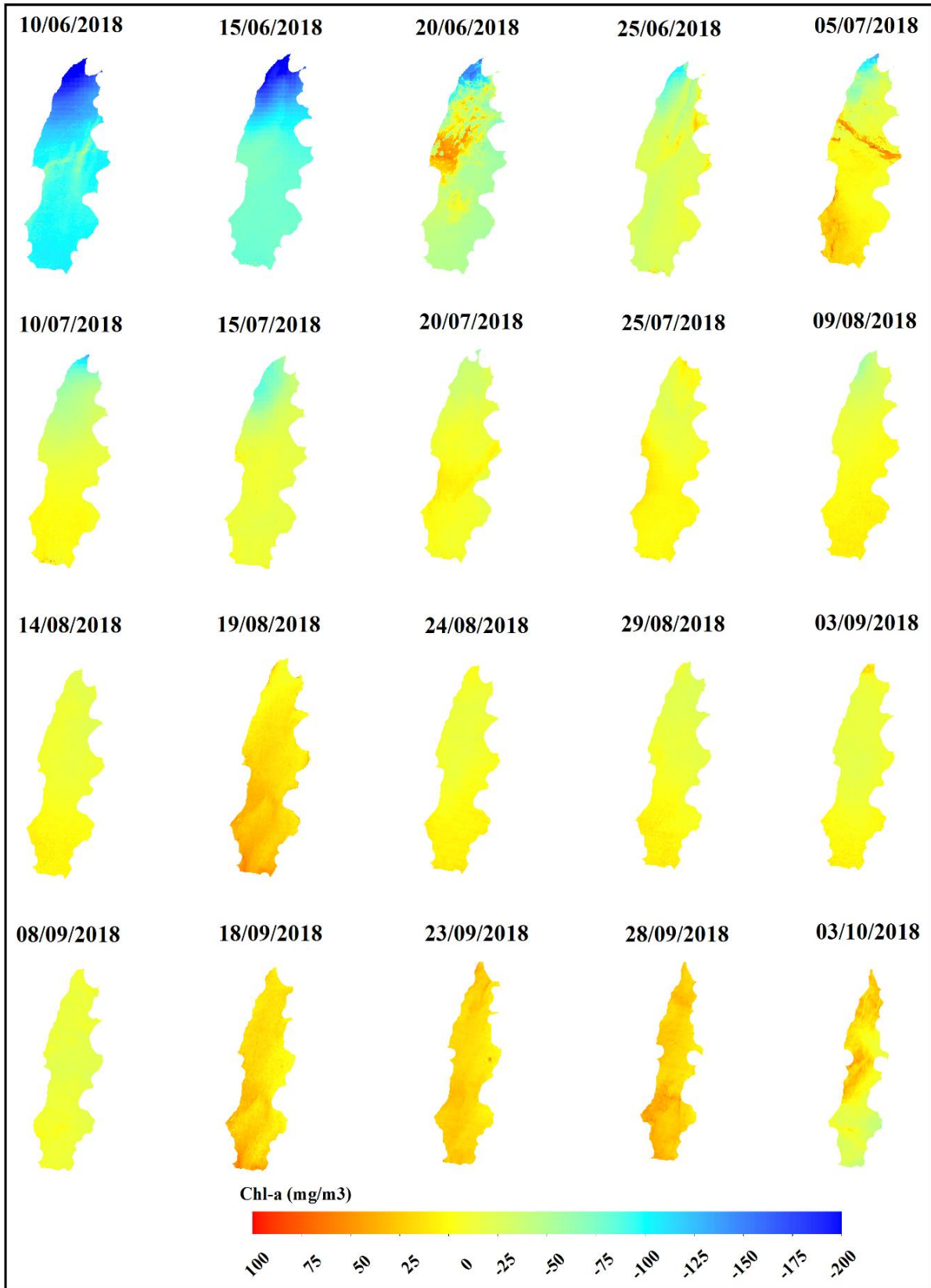
Figure 46: Differences between simulated and Sentinel-2 *Chl-a* concentrations in 2018.

6.3. Spatial distribution of *Chl-a* concentrations

Simulated and Sentinel-2 maps of *Chl-a* concentrations in 2017 and 2018 were compared. Between May and July, the horizontal distribution was found to be partly reproduced by the model with considerable overestimations in the northern part of the reservoir. During this period, the southern part of the reservoir was better represented. From July onwards, the model provided reasonable values of *Chl-a* consistent with Sentinel-2 maps over the entire reservoir. This might be due to an overestimated amount of nutrient discharged by the Litani River as well as to the approximation of nutrients concentrations in the reservoir.

The horizontal distribution of phytoplankton can be influenced by several factors (biological, physical and chemical) yet the most prevaling is the wind-induced circulation which has been demonstrated to influence the accumulation of buoyant cyanobacteria near the water surface (George & Edwards, 1976). In 2017, the prevaling daily average wind direction is mostly South-Eastern except on the 30th of June and the 29th of August where its South-Western. Wind speed values are relatively low with a maximum value of 6 m/s occuring on the 10th of June around 13:00 hours. On the other hand, the daily means of wind speed remained lower than 3.25 m/s.

Under low or moderate wind speeds (usually < 4 m/s) and consequently low turbulence, cyanobacteria, which are able to regulate their position along the water column, have been shown to prevail and to accumulate near the surface thereby causing horizontal heterogeneities (Hunter et al., 2008).

Owing to the low wind intensities at Karaoun Reservoir during the study period, turbulent mixing is limited and cyanobacteria are thus able to migrate upwards and form aggregations as shown in Figure 37 and Figure 38. The wind direction also plays an important role in determining the horizontal distribution of cyanobacteria which in general tend to accumulate in the downwind part of the reservoir (George & Heaney, 1978, Moreno-Ostos et al., 2008). The distribution of *Chl-a* seems to be in good agreement with the prevailing wind direction. For example on the 19th of August 2017, aggregations of *Chl-a* are mostly shown on the Western and Northern regions under a prevailing South-Eastern wind.

7. Conclusions and perspectives

Water surface temperature is an important parameter in limnological studies. Several algorithms have been developed to retrieve surface temperature from thermal bands of the long series of Landsat. Nevertheless, validation studies are still useful to assess the effectiveness of algorithms applied to satellite data when applied to a new case study.

In this work, water surface temperature estimated with four single channel approaches applied to data acquired by the TIRS (Band 10) onboard of the latest Landsat 8 were validated against *in situ* measurements. The results on method comparison showed a good agreement between *in situ* observations and satellite estimations for all four approaches. In particular, the SC1 algorithm provided the lowest errors in terms of *RMSE* (0.73 K) and *MAE* (0.71 K) followed by the SC2 algorithm and the RTE. The MW algorithm had the weakest performance and yielded the highest *RMSE* (1.23 K). Further, the historic retrieval of the reservoir surface temperature between from 1984 till 2018 did not reveal a warming trend.

The SC1 algorithm is the most adequate for achieving the finest match with field-based temperature observations for Karaoun Reservoir. The results indicate that the algorithm, which was formerly mostly validated on land, is also suitable for retrieving the water surface temperature of medium to small lakes and reservoirs in semi-arid regions. However additional validation studies are still needed to extent the analysis to other inland waterbodies at different latitudes and with different thermal regimes.

The results of this analysis might help to exploit Landsat images for lake surface water monitoring and hence to overcome limitations imposed by conventional measurement methods. These results can further serve for hydrodynamic modeling studies where synoptic observation of lake surface water during time might be used for initializing the model or for validating model simulations of water surface temperature.

The thermal functioning of lakes and reservoirs has a significant impact on water quality and ecological processes. In reservoirs, hydrodynamics presents specific patterns related to advection processes. In Mediterranean regions, they are amplified by the large variability of the hydrological regime, which results in high water level variation. The validation of 3D hydrodynamic models is mandatory for obtaining reliable biogeochemical simulations and a comprehensive overview of ecosystem biogeochemical processes.

In the present study, the thermal regime of Karaoun Reservoir was simulated with the Delft3D model. The model showed its ability for simulating the thermal regime of a semi-arid reservoir with a limited data set for initial conditions and hydrological and meteorological forcing. Bulk temperatures derived from Landsat images matched well with *in situ* measurements. Finally, simulated, measured and satellite temperatures are in good agreement.

Our results demonstrate the benefit of coupling *in situ*, satellite data and modelling results for an operational survey of lakes and reservoirs worldwide. For validating 3D hydrodynamic models, satellite temperatures constitute a valuable source of data complementary to punctual measurements, often spatially sparse or challenging to acquire.

The combination of *in situ* monitoring, remote sensing and modelling, currently principally applied to coastal and ocean dynamics at large space and time scales, also presents a new perspective for understanding the processes driving lake and reservoir ecosystems and the impact of climate change.

In this work, the Delft3D ecological model was calibrated in 2012 and validated in 2017 and 2018 in order to reproduce the ecological processes at Karaoun Reservoir. The model was shown to simulate well the concentrations of *Chl-a*, nitrate and orthophosphate with acceptable discrepancies for *Chl-a* in comparison to literature values (RRMSE < 100%). Although the model overestimated *Chl-a* concentrations at certain periods, it did however capture *Chl-a* peaks. Simulations delivered a good representation of the evolution and seasonal variation of phytoplankton biomass consistently with their composition and the thermal structure. The consistency of these results indicates the suitability of the model for further applications (e.g., testing climate change scenarios, management tool).

In comparison to Sentinel-2 maps, the model partly reproduced the spatial distribution of *Chl-a* concentrations, with considerable overestimations in the Northern part of Karaoun Reservoir on a few overpasses, but with a good agreement in the Southern part and for the whole reservoir in late summer.

The ecological model used in this study, in combination with the hydrodynamic model, will be further used to exploit more and better understand cyanobacteria dynamics and spatial heterogeneities observed at Karaoun Reservoir.

Covering water quality parameters, especially *Chl-a* concentrations, on large temporal and spatial scales is of great interest for scientific and management purposes of reservoirs. Such coverage can be achieved by combining *in situ* measurements, remote sensing data and model simulations. This approach is considered fruitful as it could be transferred to other study areas and also contribute to developing a data-sufficient warning system for reservoirs affected by toxic phytoplankton blooms.

Karaoun Reservoir is amongst the lakes and reservoirs in the world currently experiencing regular events of toxic cyanobacterial blooms. In this work, this was highlighted by the shift in the composition of the phytoplankton community in particular in 2017 and 2018 where the reservoir was dominated by cyanobacteria species. This, in addition to current climate change impact on the expansion of cyanobacterial blooms calls for regular water quality monitoring. In this work, three approaches were adopted, conventional monitoring, satellite remote sensing and 3D modeling. Conventional monitoring proved to be accurate however its limitations hindered the frequent

collection of *in situ* data. The latter was complemented by satellite estimations, over a large spatial scale, of water surface temperature from Landsat 8 and *Chl-a* concentrations from Sentinel-2. Mapping these water quality parameters from Landsat 8 and Sentinel-2 over medium to small size lakes and reservoirs such as in the case of Karaoun Reservoir is not common mainly due to their low spectral resolution in contrast to their high spatial resolution. This calls for additional validation studies as done in this work. Although a key source of complementary data when observations are not available, satellite data are limited in depth. In this work, 3D hydrodynamic-ecological modeling was used to extend the analysis on spatial and temporal scales in combination with *in situ* and satellite data. This combined approach proved effective in this work for providing a reliable monitoring of water quality at Karaoun Reservoir in particular given the lack of high frequency observations.

References

1. Adrian, R., O'Reilly, C.M., Zagarese, H., Baines, S.B., Hessen, D.O., Keller, W., Livingstone, D.M., Sommaruga, R., Straile, D., Van Donk, E. and Weyhenmeyer, G.A., 2009. Lakes as sentinels of climate change. *Limnology and oceanography*, 54(6part2), pp.2283-2297 [doi:10.4319/lo.2009.54.6_part_2.2283].

2. Allan, M.G., Hamilton, D.P., Trolle, D., Muraoka, K. and McBride, C., 2016. Spatial heterogeneity in geothermally-influenced lakes derived from atmospherically corrected Landsat thermal imagery and three-dimensional hydrodynamic modelling. *International journal of applied earth observation and geoinformation*, 50, pp.106-116 [doi:/10.1016/j.jag.2016.03.006].

3. Allan, M.G., 2014. *Remote sensing, numerical modelling and ground truthing for analysis of lake water quality and temperature* (Doctoral dissertation, University of Waikato).

4. Anagnostou, E., Gianni, A. and Zacharias, I., 2017. Ecological modeling and eutrophication—A review. *Natural Resource Modeling*, 30(3), p.e12130 [doi:10.1111/nrm.12130].

5. Ansper, A. and Alikas, K., 2019. Retrieval of Chlorophyll a from Sentinel-2 MSI Data for the European Union Water Framework Directive Reporting Purposes. *Remote Sensing*, 11(1), p.64 [doi:10.3390/rs11010064].

6. Arhonditsis, G.B. and Brett, M.T., 2005. Eutrophication model for Lake Washington (USA): Part I. Model description and sensitivity analysis. *Ecological modelling*, 187(2-3), pp.140-178 [doi:10.1016/j.ecolmodel.2005.01.040].

7. Asaeda, T. and Van Bon, T., 1997. Modelling the effects of macrophytes on algal blooming in eutrophic shallow lakes. *Ecological Modelling*, 104(2-3), pp.261-287 [doi:10.1016/S0304-3800(97)00129-4].

8. Baban, S.M., 1996. Trophic classification and ecosystem checking of lakes using remotely sensed information. *Hydrological sciences journal*, 41(6), pp.939-957 [doi:10.1080/02626669609491560].

9. Babbar-Sebens, M., Li, L., Song, K. and Xie, S., 2013. On the Use of Landsat-5 TM Satellite for Assimilating Water Temperature Observations in 3D Hydrodynamic Model of Small Inland Reservoir in Midwestern US. *Advances in Remote Sensing*, 2(3), pp. 214-227 [doi:10.4236/ars.2013.23024].

10. Bakker, E.S. and Hilt, S., 2016. Impact of water-level fluctuations on cyanobacterial blooms: options for management. *Aquatic ecology*, 50(3), pp.485-498 [doi:10.1007/s10452-015-9556-x].

11. Baracchini, T., Chu, P.Y., Sukys, J., Lieberherr, G., Wunderle, S., Wüest, A.J. and Bouffard, D., 2020. Data assimilation of in situ and satellite remote sensing data to 3D hydrodynamic lake models: a case study using Delft3D-FLOW v4. 03 and OpenDA v2. 4. *Geoscientific model development (GMD)*, 13(3), pp.1267-1284[doi:10.5194/gmd-13-1267-2020].

12. Barsi, J., Schott, J., Hook, S., Raqueno, N., Markham, B. and Radocinski, R., 2014. Landsat-8 thermal infrared sensor (TIRS) vicarious radiometric calibration. *Remote Sensing*, 6(11), pp.11607-11626 [doi:10.3390/rs61111607].

13. Barsi, J.A., Schott, J.R., Palluconi, F.D. and Hook, S.J., 2005, August. Validation of a web-based atmospheric correction tool for single thermal band instruments. In *Earth Observing Systems X* (Vol. 5882, p. 58820E). International Society for Optics and Photonics [doi10.1117/12.619990].

14. Barsi, J.A., Barker, J.L. and Schott, J.R., 2003, July. An atmospheric correction parameter calculator for a single thermal band earth-sensing instrument. In IGARSS 2003. 2003 *IEEE International Geoscience and Remote Sensing Symposium. Proceedings* (IEEE Cat. No. 03CH37477) (Vol. 5, pp. 3014-3016). IEEE.

15. Bartram, J. and Chorus, I., 1999. *Toxic cyanobacteria in water: a guide to their public health consequences, monitoring and management*. CRC Press.

16. Bastien, C., Cardin, R., Veilleux, É., Deblois, C., Warren, A. and Laurion, I., 2011. Performance evaluation of phycocyanin probes for the monitoring of cyanobacteria. *Journal of Environmental Monitoring*, 13(1), pp.110-118 [doi:10.1039/C0EM00366B]..

17. Becker, M.W. and Daw, A., 2005. Influence of lake morphology and clarity on water surface temperature as measured by EOS ASTER. *Remote sensing of environment*, 99(3), pp.288-294 [doi:10.1016/j.rse.2005.09.003].

18. Bindhu, V.M., Narasimhan, B. and Sudheer, K.P., 2013. Development and verification of a non-linear disaggregation method (NL-DisTrad) to downscale MODIS land surface temperature to the spatial scale of Landsat thermal data to estimate evapotranspiration. *Remote Sensing of Environment*, 135, pp.118-129 [doi:10.1016/j.rse.2013.03.023].

19. Binding, C.E., Jerome, J.H., Bukata, R.P. and Booty, W.G., 2010. Suspended particulate matter in Lake Erie derived from MODIS aquatic colour imagery. *International Journal of Remote Sensing*, 31(19), pp.5239-5255 [doi:10.1080/01431160903302973].

20. Bisquert, M., Sánchez, J.M. and Caselles, V., 2016. Evaluation of disaggregation methods for downscaling MODIS land surface temperature to Landsat spatial resolution in Barrax test site. *IEEE Journal of Selected Topics in Applied Earth Observations and Remote Sensing*, 9(4), pp.1430-1438 [doi:10.1109/JSTARS.2016.2519099].

21. Blunden, J. and Arndt, D.S., 2016. State of the climate in 2015. *Bulletin of the American Meteorological Society*, 97(8), pp.Si-S275 [doi:10.1175/2016BAMSStateoftheClimate.1].

22. Bowling, L.C., Blais, S. and Sinotte, M., 2015. Heterogeneous spatial and temporal cyanobacterial distributions in Missisquoi Bay, Lake Champlain: An analysis of a 9 year data set. *Journal of Great Lakes Research*, 41(1), pp.164-179 [doi:10.1016/j.jglr.2014.12.012].

23. Brando, V.E., Braga, F., Zaggia, L., Giardino, C., Bresciani, M., Matta, E., Bellafiore, D., Ferrarin, C., Maicu, F., Benetazzo, A. and Bonaldo, D., 2015. High-resolution satellite turbidity and sea surface temperature observations of river plume interactions during a significant flood event. *Ocean Science*, 11(6), pp.909-920 [doi:10.5194/os-11-909-2015].

24. Bresciani, M., Stroppiana, D., Odermatt, D., Morabito, G. and Giardino, C., 2011. Assessing remotely sensed chlorophyll-a for the implementation of the Water Framework Directive in European perialpine lakes. *Science of the Total Environment*, 409(17), pp.3083-3091 [doi:10.1016/j.scitotenv.2011.05.001].

25. Breunig, F.M., Pereira Filho, W., Galvao, L.S. and Wachholz, F., 2016. Assessing the long-term variability of TSS and chlorophyll in subtropical reservoirs using MODIS data. *IEEE Journal of Selected Topics in Applied Earth Observations and Remote Sensing*, 9(12), pp.5406-5412 [doi:10.1109/JSTARS.2016.2589820].

26. Brezonik, P., Menken, K.D. and Bauer, M., 2005. Landsat-based remote sensing of lake water quality characteristics, including chlorophyll and colored dissolved organic matter (CDOM). *Lake and Reservoir Management*, 21(4), pp.373-382 [doi:10.1080/07438140509354442].

27. Brient, L., Lengronne, M., Bertrand, E., Rolland, D., Sipel, A., Steinmann, D., Baudin, I., Legeas, M., Le Rouzic, B. and Bormans, M., 2008. A phycocyanin probe as a tool for monitoring cyanobacteria in freshwater bodies. *Journal of Environmental Monitoring*, 10(2), pp.248-255 [doi:10.1039/b714238b].

28. Brooks, B.W., Lazorchak, J.M., Howard, M.D., Johnson, M.V.V., Morton, S.L., Perkins, D.A., Reavie, E.D., Scott, G.I., Smith, S.A. and Steevens, J.A., 2016. Are harmful algal blooms becoming the greatest inland water quality threat to public health and aquatic ecosystems?. *Environmental toxicology and chemistry*, 35(1), pp.6-13 [https://doi.org/10.1002/etc.3220].

29. Chanudet, V., Fabre, V. and van der Kaaij, T., 2012. Application of a three-dimensional hydrodynamic model to the Nam Theun 2 Reservoir (Lao PDR). *Journal of Great Lakes Research*, 38(2), pp.260-269 [doi:10.1016/j.jglr.2012.01.008].

30. Chen, B., Huang, B. and Xu, B., 2015. Comparison of spatiotemporal fusion models: A review. *Remote Sensing,* 7(2), pp.1798-1835 [doi:10.3390/rs70201798].

31. Chen, J., Zhu, W., Tian, Y.Q., Yu, Q., Zheng, Y. and Huang, L., 2017. Remote estimation of colored dissolved organic matter and chlorophyll-a in Lake Huron using Sentinel-2 measurements. *Journal of Applied Remote Sensing*, 11(3), p.036007 [doi:10.1117/1.JRS.11.036007].

32. Cristóbal, J., Jiménez-Muñoz, J., Prakash, A., Mattar, C., Skoković, D. and Sobrino, J., 2018. An improved single-channel method to retrieve land surface temperature from the landsat-8 thermal band. *Remote Sensing*, 10(3), p.431 [doi:10.3390/rs10030431].

33. Crosman, E.T. and Horel, J.D., 2009. MODIS-derived surface temperature of the Great Salt Lake. *Remote Sensing of Environment*, 113(1), pp.73-81 [doi:10.1016/j.rse.2008.08.013].

34. Curtarelli, M.P., Ogashawara, I., Alcântara, E.H. and Stech, J.L., 2015. Coupling remote sensing bio-optical and three-dimensional hydrodynamic modeling to study the phytoplankton dynamics in a tropical hydroelectric reservoir. *Remote Sensing of Environment*, 157, pp.185-198 [doi:10.1016/j.rse.2014.06.013].

35. Curtarelli, M.P., Alcântara, E., Rennó, C.D., Assireu, A.T., Bonnet, M.P. and Stech, J.L., 2014. Modelling the surface circulation and thermal structure of a tropical reservoir using three-dimensional hydrodynamic lake model and remote-sensing data. *Water and environment journal*, 28(4), pp.516-525 [doi:10.1111/wej.12066].

36. Dall'Olmo, G., Gitelson, A.A. and Rundquist, D.C., 2003. Towards a unified approach for remote estimation of chlorophyll-a in both terrestrial vegetation and turbid productive waters. *Geophysical Research Letters*, 30(18) [doi:10.1029/2003GL018065].

37. Dee, D.P., Uppala, S.M., Simmons, A.J., Berrisford, P., Poli, P., Kobayashi, S., Andrae, U., Balmaseda, M.A., Balsamo, G., Bauer, D.P. and Bechtold, P., 2011. The ERA-Interim reanalysis: Configuration and performance of the data assimilation system. *Quarterly Journal of the royal meteorological society*,

137(656), pp.553-597 [doi:10.1002/qj.828].

38. Dekker, A.G., Vos, R.J. and Peters, S.W.M., 2001. Comparison of remote sensing data, model results and in situ data for total suspended matter (TSM) in the southern Frisian lakes. *Science of the Total Environment*, 268(1-3), pp.197-214 [doi:10.1016/S0048-9697(00)00679-3].

39. Deltares (2014) a. D-Water Quality Technical Reference Manual Version 5.01 (24 October 2014).

40. Deltares (2014) b. D-Water Quality User Manual Version 4.99 (24 October 2014).

41. Deltares. (2013). Delft3D-FLOW user manual. The Netherlands: Delft.

42. Deus, R., Brito, D., Kenov, I.A., Lima, M., Costa, V., Medeiros, A., Neves, R. and Alves, C.N., 2013. Three-dimensional model for analysis of spatial and temporal patterns of phytoplankton in Tucuruí reservoir, Pará, Brazil. *Ecological modelling*, 253, pp.28-43 [doi:10.1016/j.ecolmodel.2012.10.013].

43. Deutsch, E.S. and Alameddine, I., 2019. Hindcasting eutrophication and changes in temperature and storage volume in a semi-arid reservoir: a multi-decadal Landsat-based assessment. *Environmental monitoring and assessment*, 191(1), p.41 [doi:10.1007/s10661-018-7180-7].

44. Dörnhöfer, K. and Oppelt, N., 2016. Remote sensing for lake research and monitoring–Recent advances. *Ecological Indicators*, 64, pp.105-122 [doi:/10.1016/j.ecolind.2015.12.009].

45. Doubek, J.P. and Carey, C.C., 2017. Catchment, morphometric, and water quality characteristics differ between reservoirs and naturally formed lakes on a latitudinal gradient in the conterminous United States. *Inland Waters*, 7(2), pp.171-180 [doi:10.1080/20442041.2017.1293317].

46. Downing, J.A., 2014. Limnology and oceanography: two estranged twins reuniting by global change. *Inland Waters*, 4(2), pp.215-232 [doi:10.5268/IW-4.2.753].

47. Duan, H., Tao, M., Loiselle, S.A., Zhao, W., Cao, Z., Ma, R. and Tang, X., 2017. MODIS observations of cyanobacterial risks in a eutrophic lake: Implications for long-term safety evaluation in drinking-water source. *Water research*, 122, pp.455-470 [doi:10.1016/j.watres.2017.06.022].

48. El Hourany, R., Fadel, A., Gemayel, E., Saab, M.A.A. and Faour, G., 2017. Spatio-temporal variability of the phytoplankton biomass in the Levantine basin between 2002 and 2015 using MODIS products. *Oceanologia*, 59(2), pp.153-165 [doi:10.1016/j.oceano.2016.12.002].

49. Eraso, R., de Lourdes Galo, M., Alcântara, E., Shimabukuro, M. and Carmo, A., 2018. Locally tuned model to map the chlorophyll-a and the trophic state in Porto Primavera reservoir using MODIS/Terra images. *Modeling Earth Systems and Environment*, 4(1), pp.39-47 [doi:10.1007/s40808-018-0415-3].

50. Fadel, A., Sharaf, N., Siblini, M., Slim, K. and Kobaissi, A., 2019. A simple modelling approach to simulate the effect of different climate scenarios on toxic cyanobacterial bloom in a eutrophic reservoir. *Ecohydrology & Hydrobiology* [doi:10.1016/j.ecohyd.2019.02.005].

51. Fadel, A., Lemaire, B.J., Vinçon-Leite, B., Atoui, A., Slim, K. and Tassin, B., 2017. On the successful use of a simplified model to simulate the succession of toxic cyanobacteria in a hypereutrophic reservoir with a highly fluctuating water level. *Environmental Science and Pollution Research*, 24(26), pp.20934-20948 [doi:10.1007/s11356-017-9723-9].

52. Fadel, A., Faour, G. and Slim, K., 2016. Assessment of the trophic state and chlorophyll-a concentrations using Landsat OLI in Karaoun reservoir, Lebanon. *Lebanese Science Journal*, 17(2), p.130 [doi:10.22453/LSJ-017.2.130145].

53. Fadel, A., Atoui, A., Lemaire, B.J., Vinçon-Leite, B. and Slim, K., 2015. Environmental factors associated with phytoplankton succession in a Mediterranean reservoir with a highly fluctuating water level. *Environmental monitoring and assessment*, 187(10), p.633 [doi:10.1007/s10661-015-4852-4].

54. Fadel, A., Lemaire, B.J., Atoui, A., Vinçon-Leite, B., Amacha, N., Slim, K. and Tassin, B., 2014. First assessment of the ecological status of K araoun reservoir, Lebanon. *Lakes & Reservoirs: Research & Management*, 19(2), pp.142-157 [doi:10.1111/lre.12058].

55. Falconer, R.A., George, D.G. and Hall, P., 1991. Three-dimensional numerical modelling of wind-driven circulation in a shallow homogeneous lake. *Journal of hydrology*, 124(1-2), pp.59-79 [doi:10.1016/0022-1694(91)90006-4].

56. Federal Water Pollution Control Act (33 USC 1251 et seq.)., 2002 [https://www.epa.gov/sites/production/files/2017-08/documents/federal-water-pollution-control-act-508full.pdf].

57. Fenocchi, A., Rogora, M., Morabito, G., Marchetto, A., Sibilla, S. and Dresti, C., 2019. Applicability of a one-dimensional coupled ecological-hydrodynamic numerical model to future projections in a very deep large lake (Lake Maggiore, Northern Italy/Southern Switzerland). *Ecological modelling*, 392, pp.38-51 [doi:10.1016/j.ecolmodel.2018.11.005].

58. García-Santos, V., Cuxart, J., Martínez-Villagrasa, D., Jiménez, M. and Simó, G., 2018. Comparison of three

methods for estimating land surface temperature from landsat 8-tirs sensor data. *Remote Sensing*, 10(9), p.1450 [doi:10.3390/rs10091450].

59. George, D.G. and Heaney, S.I., 1978. Factors influencing the spatial distribution of phytoplankton in a small productive lake. *The Journal of Ecology*, pp.133-155.

60. George, D.G. and Edwards, R.W., 1976. The effect of wind on the distribution of chlorophyll a and crustacean plankton in a shallow eutrophic reservoir. *Journal of Applied Ecology*, pp.667-690.

61. Giardino, C., Bresciani, M., Stroppiana, D., Oggioni, A. and Morabito, G., 2014. Optical remote sensing of lakes: an overview on Lake Maggiore. *Journal of Limnology* [doi:10.4081/jlimnol.2014.817].

62. Giardino, C., Bresciani, M., Villa, P. and Martinelli, A., 2010. Application of remote sensing in water resource management: the case study of Lake Trasimeno, Italy. *Water resources management*, 24(14), pp.3885-3899 [doi:10.1007/s11269-010-9639-3].

63. Giardino, C., Brando, V.E., Dekker, A.G., Strömbeck, N. and Candiani, G., 2007. Assessment of water quality in Lake Garda (Italy) using Hyperion. *Remote Sensing of Environment*, 109(2), pp.183-195 [doi:10.1016/j.rse.2006.12.017].

64. Giardino, C., Pepe, M., Brivio, P.A., Ghezzi, P. and Zilioli, E., 2001. Detecting chlorophyll, Secchi disk depth and surface temperature in a sub-alpine lake using Landsat imagery. *Science of the Total Environment*, 268(1-3), pp.19-29 [doi:10.1016/S0048-9697(00)00692-6].

65. Gitelson, A.A., Dall'Olmo, G., Moses, W., Rundquist, D.C., Barrow, T., Fisher, T.R., Gurlin, D. and Holz, J., 2008. A simple semi-analytical model for remote estimation of chlorophyll-a in turbid waters: Validation. *Remote Sensing of Environment*, 112(9), pp.3582-3593 [doi:10.1016/j.rse.2008.04.015].

66. Gitelson, A.A., Vina, A., Ciganda, V., Rundquist, D.C. and Arkebauer, T.J., 2005. Remote estimation of canopy chlorophyll content in crops. *Geophysical Research Letters*, 32(8) [doi:10.1029/2005GL022688].

67. Gitelson, A.A., Gritz, Y. and Merzlyak, M.N., 2003. Relationships between leaf chlorophyll content and spectral reflectance and algorithms for non-destructive chlorophyll assessment in higher plant leaves. *Journal of plant physiology*, 160(3), pp.271-282 [doi:10.1078/0176-1617-00887].

68. Gitelson, A., 1992. The peak near 700 nm on radiance spectra of algae and water: relationships of its magnitude and position with chlorophyll concentration. *International Journal of Remote Sensing*, 13(17), pp.3367-3373 [doi:10.1080/01431169208904125].

69. Gobler, C.J., Burkholder, J.M., Davis, T.W., Harke, M.J., Johengen, T., Stow, C.A. and Van de Waal, D.B., 2016. The dual role of nitrogen supply in controlling the growth and toxicity of cyanobacterial blooms. *Harmful Algae*, 54, pp.87-97 [doi:10.1016/j.hal.2016.01.010].

70. Gomez, C., White, J.C. and Wulder, M.A., 2016. Optical remotely sensed time series data for land cover classification: A review. *ISPRS Journal of Photogrammetry and Remote Sensing*, 116, pp.55-72 [doi:10.1016/j.isprsjprs.2016.03.008].

71. Gordon, H.R. and Morel, A.Y., 2012. *Remote assessment of ocean color for interpretation of satellite visible imagery: a review* (Vol. 4). Springer Science & Business Media.

72. Gregg, W.W., Casey, N.W. and McClain, C.R., 2005. Recent trends in global ocean chlorophyll. *Geophysical Research Letters*, 32(3) [doi:10.1029/2004GL021808].

73. Grendaitė, D., Stonevičius, E., Karosienė, J., Savadova, K. and Kasperovičienė, J., 2018. Chlorophyll-a concentration retrieval in eutrophic lakes in Lithuania from Sentinel-2 data. *Geografija*, 4(1) [doi:10.6001/geol-geogr.v4i1.3720].

74. Guan, D.X., Wang, X., Xu, H., Chen, L., Li, P. and Ma, L.Q., 2018. Temporal and spatial distribution of Microcystis biomass and genotype in bloom areas of Lake Taihu. *Chemosphere*, 209, pp.730-738 [doi:10.1016/j.chemosphere.2018.06.141].

75. Ha, N.T.T., Koike, K., Nhuan, M.T., Canh, B.D., Thao, N.T.P. and Parsons, M., 2017. Landsat 8/OLI two bands ratio algorithm for chlorophyll-a concentration mapping in hypertrophic waters: An application to West Lake in Hanoi (Vietnam). *IEEE Journal of Selected Topics in Applied Earth Observations and Remote Sensing*, 10(11), pp.4919-4929.

76. Haji Gholizadeh, M., Melesse, A.M. and Reddi, L., 2016. Spaceborne and airborne sensors in water quality assessment. *International Journal of Remote Sensing*, 37(14), pp.3143-3180 [doi:/10.1080/01431161.2016.1190477].

77. Harke, M.J., Steffen, M.M., Gobler, C.J., Otten, T.G., Wilhelm, S.W., Wood, S.A. and Paerl, H.W., 2016. A review of the global ecology, genomics, and biogeography of the toxic cyanobacterium, Microcystis spp. *Harmful Algae*, 54, pp.4-20 [doi:10.1016/j.hal.2015.12.007].

78. He, X., Liu, Y.L., Conklin, A., Westrick, J., Weavers, L.K., Dionysiou, D.D., Lenhart, J.J., Mouser, P.J., Szlag, D. and Walker, H.W., 2016. Toxic cyanobacteria and drinking water: impacts, detection, and treatment. *Harmful algae*, 54, pp.174-193 [doi:10.1016/j.hal.2016.01.001].

79. Hedger, R.D., Olsen, N.R., Malthus, T.J. and Atkinson, P.M., 2002. Coupling remote sensing with computational fluid dynamics modelling to estimate lake chlorophyll-a concentration. *Remote Sensing of Environment*, 79(1), pp.116-122 [doi:10.1016/S0034-4257(01)00244-9].

80. Hestir, E.L., Brando, V.E., Bresciani, M., Giardino, C., Matta, E., Villa, P. and Dekker, A.G., 2015. Measuring freshwater aquatic ecosystems: The need for a hyperspectral global mapping satellite mission. *Remote Sensing of Environment*, 167, pp.181-195 [doi:10.1016/j.rse.2015.05.023].

81. Hodges, B. R., 2009. Hydrodynamical modeling. *Encyclopedia of Inland Waters*, G. E. Likens, ed., Elsevier, Oxford, U.K [doi:10.1016/B978-012370626-3.00088-0].

82. Horion, S., Bergamino, N., Stenuite, S., Descy, J.P., Plisnier, P.D., Loiselle, S.A. and Cornet, Y., 2010. Optimized extraction of daily bio-optical time series derived from MODIS/Aqua imagery for Lake Tanganyika, Africa. *Remote Sensing of Environment*, 114(4), pp.781-791 [doi:10.1016/j.rse.2009.11.012].

83. Huang, Y., Liu, H., Hinkel, K., Yu, B., Beck, R. and Wu, J., 2017. Analysis of thermal structure of arctic lakes at local and regional scales using in situ and multidate Landsat-8 data. *Water Resources Research*, 53(11), pp.9642-9658 [doi:10.1002/2017WR021335].

84. Huisman, J., Codd, G.A., Paerl, H.W., Ibelings, B.W., Verspagen, J.M. and Visser, P.M., 2018. Cyanobacterial blooms. *Nature Reviews Microbiology*, 16(8), p.471 [doi:10.1038/s41579-018-0040-1].

85. Hunter, P.D., Tyler, A.N., Willby, N.J. and Gilvear, D.J., 2008. The spatial dynamics of vertical migration by Microcystis aeruginosa in a eutrophic shallow lake: A case study using high spatial resolution time-series airborne remote sensing. *Limnology and Oceanography*, 53(6), pp.2391-2406 [doi:10.4319/lo.2008.53.6.2391].

86. Isaya Ndossi, M. and Avdan, U., 2016. Application of open source coding technologies in the production of land surface temperature (LST) maps from Landsat: a PyQGIS plugin. *Remote sensing*, 8(5), p.413 [doi:10.3390/rs8050413].

87. Javaheri, A., Babbar-Sebens, M. and Miller, R.N., 2016. From skin to bulk: An adjustment technique for assimilation of satellite-derived temperature observations in numerical models of small inland water bodies. *Advances in Water Resources*, 92, pp.284-298 [doi:10.1016/j.advwatres.2016.03.012].

88. Jeppesen, E., Kronvang, B., Meerhoff, M., Søndergaard, M., Hansen, K.M., Andersen, H.E., Lauridsen, T.L., Liboriussen, L., Beklioglu, M., Özen, A. and Olesen, J.E., 2009. Climate change effects on runoff, catchment phosphorus loading and lake ecological state, and potential adaptations. *Journal of Environmental Quality*, 38(5), pp.1930-1941 [doi:10.2134/jeq2008.0113].

89. Jiao, H.B., Zha, Y., Gao, J., Li, Y.M., Wei, Y.C. and Huang, J.Z., 2006. Estimation of chlorophyll-a concentration in Lake Tai, China using in situ hyperspectral data. *International Journal of Remote Sensing*, 27(19), pp.4267-4276 [doi:10.1080/01431160600702434].

90. Jiménez-Muñoz, J.C., Sobrino, J.A., Skoković, D., Mattar, C. and Cristóbal, J., 2014. Land surface temperature retrieval methods from Landsat-8 thermal infrared sensor data. *IEEE Geoscience and remote sensing letters*, 11(10), pp.1840-1843.

91. Jiménez-Muñoz, J.C., Cristóbal, J., Sobrino, J.A., Sòria, G., Ninyerola, M. and Pons, X., 2009. Revision of the single-channel algorithm for land surface temperature retrieval from Landsat thermal-infrared data. *IEEE Transactions on geoscience and remote sensing*, 47(1), pp.339-349.

92. Jiménez-Muñoz, J.C. and Sobrino, J.A., 2003. A generalized single-channel method for retrieving land surface temperature from remote sensing data. *Journal of Geophysical Research: Atmospheres*, 108(D22) [doi:10.1029/2003JD003480].

93. Jung, H.S. and Park, S.W., 2014. Multi-sensor fusion of Landsat 8 thermal infrared (TIR) and panchromatic (PAN) images. *Sensors*, 14(12), pp.24425-24440 [doi:10.3390/s141224425].

94. Kaçıkoç, M. and Beyhan, M., 2014. Hydrodynamic and water quality modeling of Lake Eğirdir. *CLEAN– Soil, Air, Water*, 42(11), pp.1573-1582 [doi:10.1002/clen.201300455].

95. Kerr, Y.H., Lagouarde, J.P. and Imbernon, J., 1992. Accurate land surface temperature retrieval from AVHRR data with use of an improved split window algorithm. *Remote Sensing of Environment*, 41(2-3), pp.197-209 [doi:10.1016/0034-4257(92)90078-X].

96. Kettle, H., Thompson, R., Anderson, N.J. and Livingstone, D.M., 2004. Empirical modeling of summer lake surface temperatures in southwest Greenland. *Limnology and Oceanography*, 49(1), pp.271-282 [doi:10.4319/lo.2004.49.1.0271].

97. Kiefer, I., Odermatt, D., Anneville, O., Wüest, A. and Bouffard, D., 2015. Application of remote sensing for

the optimization of in-situ sampling for monitoring of phytoplankton abundance in a large lake. *Science of the Total Environment*, 527, pp.493-506 [doi:10.1016/j.scitotenv.2015.05.011].

98. Komárek, J. and Anagnostidis, K., 2005. *Süßwasserflora von Mitteleuropa, bd. 19/2: Cyanoprokaryota: Oscillatoriales* (Vol. 19). Spektrum Akademischer Verlag.

99. Komárek, J., 1999. Cyanoprokaryota 1. Teil: *Chroococcales. Subwasserflora von Mitteleuropa*, 19, pp.1-548.

100. Konopka, A. and Brock, T.D., 1978. Effect of temperature on blue-green algae (cyanobacteria) in Lake Mendota. *Appl. Environ. Microbiol*., 36(4), pp.572-576.

101. Kumar, K., Mella-Herrera, R.A. and Golden, J.W., 2010. Cyanobacterial heterocysts. *Cold Spring Harbor perspectives in biology*, 2(4), p.a000315 [doi:10.1101/cshperspect.a000315).

102. Lagouarde, J.P., Bhattacharya, B.K., Crébassol, P., Gamet, P., Babu, S.S., Boulet, G., Briottet, X., Buddhiraju, K.M., Cherchali, S., Dadou, I. and Dedieu, G., 2018, July. The Indian-French Trishna Mission: Earth Observation in the Thermal Infrared with High Spatio-Temporal Resolution. In *IGARSS 2018-2018 IEEE International Geoscience and Remote Sensing Symposium* (pp. 4078-4081). IEEE [10.1109/IGARSS.2018.8518720].

103. Lamaro, A.A., Marinelarena, A., Torrusio, S.E. and Sala, S.E., 2013. Water surface temperature estimation from Landsat 7 ETM+ thermal infrared data using the generalized single-channel method: Case study of Embalse del Río Tercero (Córdoba, Argentina). *Advances in Space Research*, 51(3), pp.492-500 [doi:10.1016/j.asr.2012.09.032].

104. Lavrova, O.Y., Soloviev, D.M., Strochkov, M.A., Bocharova, T.Y. and Kashnitsky, A.V., 2016, October. River plumes investigation using Sentinel-2A MSI and Landsat-8 OLI data. In *Remote Sensing of the Ocean, Sea Ice, Coastal Waters, and Large Water Regions 2016* (Vol. 9999, p. 99990G). International Society for Optics and Photonics [doi:10.1117/12.2241312].

105. Le Moal, M., Gascuel-Odoux, C., Ménesguen, A., Souchon, Y., Étrillard, C., Levain, A., Moatar, F., Pannard, A., Souchu, P., Lefebvre, A. and Pinay, G., 2019. Eutrophication: a new wine in an old bottle?. *Science of the Total Environment,* 651, pp.1-11 [doi:10.1016/j.scitotenv.2018.09.139]

106. Leon, L.F., Smith, R.E., Hipsey, M.R., Bocaniov, S.A., Higgins, S.N., Hecky, R.E., Antenucci, J.P., Imberger, J.A. and Guildford, S.J., 2011. Application of a 3D hydrodynamic–biological model for seasonal and spatial dynamics of water quality and phytoplankton in Lake Erie. *Journal of Great Lakes Research*, 37(1), pp.41-53 [doi:10.1016/j.jglr.2010.12.007].

107. Li, J. and Roy, D., 2017. A global analysis of Sentinel-2A, Sentinel-2B and Landsat-8 data revisit intervals and implications for terrestrial monitoring. *Remote Sensing*, 9(9), p.902 [doi:10.3390/rs9090902].

108. Li, Y., Zhang, Y., Shi, K., Zhou, Y., Zhang, Y., Liu, X. and Guo, Y., 2018. Spatiotemporal dynamics of chlorophyll-a in a large reservoir as derived from Landsat 8 OLI data: understanding its driving and restrictive factors. *Environmental Science and Pollution Research*, 25(2), pp.1359-1374 [doi:10.1007/s11356-017-0536-7].

109. Li, Z., Chen, Q. and Xu, Q., 2015. Modeling algae dynamics in Meiliang Bay of Taihu Lake and parameter sensitivity analysis. *Journal of hydro-environment research*, 9(2), pp.216-225 [doi:10.1016/j.jher.2014.10.001].

110. Lindim, C., Pinho, J.L. and Vieira, J.M.P., 2011. Analysis of spatial and temporal patterns in a large reservoir using water quality and hydrodynamic modeling. *Ecological Modelling*, 222(14), pp.2485-2494 [doi:10.1016/j.ecolmodel.2010.07.019].

111. Los, F.J., 2009. *Eco-hydrodynamic modelling of primary production in coastal waters and lakes using BLOOM* (Vol. 1). Ios Press.

112.

113. Lyu, H., Li, X., Wang, Y., Jin, Q., Cao, K., Wang, Q. and Li, Y., 2015. Evaluation of chlorophyll-a retrieval algorithms based on MERIS bands for optically varying eutrophic inland lakes. *Science of the Total Environment*, 530, pp.373-382 [doi:10.1016/j.scitotenv.2015.05.115].

114. Ma, S., Kassinos, S.C., Fatta Kassinos, D. and Akylas, E., 2008. Effects of selective water withdrawal schemes on thermal stratification in Kouris Dam in Cyprus. *Lakes & Reservoirs: Research & Management*, 13(1), pp.51-61 [doi:10.1111/j.1440-1770.2007.00353.x].

115. Mancino, G., Nolè, A., Urbano, V., Amato, M. and Ferrara, A., 2009. Assessing water quality by remote sensing in small lakes: the case study of Monticchio lakes in southern Italy. *iForest-Biogeosciences and Forestry*, 2(4), p.154 [doi:10.3832/ifor0507-002].

116. Mao, J., Jiang, D. and Dai, H., 2015. Spatial–temporal hydrodynamic and algal bloom modelling analysis of a reservoir tributary embayment. *Journal of Hydro-Environment Research*, 9(2), pp.200-215 [doi:10.1016/j.jher.2014.09.005].

117. Matthews, M.W., 2017. Bio-optical modeling of phytoplankton chlorophyll-a. In *Bio-optical Modeling and Remote Sensing of Inland Waters* (pp. 157-188). Elsevier [doi:10.1016/B978-0-12-804644-9.00006-9].

118. Matthews, M.W., 2011. A current review of empirical procedures of remote sensing in inland and near-coastal transitional waters. *International Journal of Remote Sensing*, 32(21), pp.6855-6899 [doi:10.1080/01431161.2010.512947].

119. McFeeters, S.K., 1996. The use of the Normalized Difference Water Index (NDWI) in the delineation of open water features. *International journal of remote sensing*, 17(7), pp.1425-1432 [doi:10.1080/01431169608948714].

120. Medina-Cobo, M., Domínguez, J.A., Quesada, A. and De Hoyos, C., 2014. Estimation of cyanobacteria biovolume in water reservoirs by MERIS sensor. *Water research*, 63, pp.10-20 [doi:10.1016/j.watres.2014.06.001].

121. Menken, K.D., Brezonik, P.L. and Bauer, M.E., 2006. Influence of chlorophyll and colored dissolved organic matter (CDOM) on lake reflectance spectra: Implications for measuring lake properties by remote sensing. *Lake and Reservoir Management*, 22(3), pp.179-190 [doi:10.1080/07438140609353895].

122. Molkov, A.A., Fedorov, S.V., Pelevin, V.V. and Korchemkina, E.N., 2019. Regional Models for High-Resolution Retrieval of Chlorophyll a and TSM Concentrations in the Gorky Reservoir by Sentinel-2 Imagery. *Remote Sensing*, 11(10), p.1215 [doi:10.3390/rs11101215].

123. Moreno-Ostos, E., Marcé, R., Ordóñez, J., Dolz, J. and Armengol, J., 2008. Hydraulic management drives heat budgets and temperature trends in a Mediterranean reservoir. *International Review of Hydrobiology*, 93(2), pp.131-147 [doi:10.1002/iroh.200710965].

124. Moss, B., Kosten, S., Meerhoff, M., Battarbee, R.W., Jeppesen, E., Mazzeo, N., Havens, K., Lacerot, G., Liu, Z., De Meester, L. and Paerl, H., 2011. Allied attack: climate change and eutrophication. *Inland waters*, 1(2), pp.101-105 [doi:10.5268/IW-1.2.359].

125. Naselli-Flores, L. and Barone, R., 2003. Steady-state assemblages in a Mediterranean hypertrophic reservoir. The role of Microcystis ecomorphological variability in maintaining an apparent equilibrium. In *Phytoplankton and Equilibrium Concept: The Ecology of Steady-State Assemblages* (pp. 133-143). Springer, Dordrecht [doi:10.1007/978-94-017-2666-5_12].

126. Nouchi, V., Kutser, T., Wüest, A., Müller, B., Odermatt, D., Baracchini, T. and Bouffard, D., 2019. Resolving biogeochemical processes in lakes using remote sensing. *Aquatic Sciences*, 81(2), p.27 [doi:10.1007/s00027-019-0626-3].

127. Oesch, D.C., Jaquet, J.M., Hauser, A. and Wunderle, S., 2005. Lake surface water temperature retrieval using advanced very high resolution radiometer and Moderate Resolution Imaging Spectroradiometer data: Validation and feasibility study. *Journal of Geophysical Research: Oceans*, 110(C12) [doi:10.1029/2004JC002857].

128. Ogashawara, I., Mishra, D.R. and Gitelson, A.A., 2017. Remote sensing of inland waters: background and current state-of-the-art. In *Bio-optical Modeling and Remote Sensing of Inland Waters* (pp. 1-24). Elsevier [doi:10.1016/B978-0-12-804644-9.00001-X].

129. Ogashawara, I., Alcântara, E., Curtarelli, M., Adami, M., Nascimento, R., Souza, A., Stech, J. and Kampel, M., 2014. Performance analysis of MODIS 500-m spatial resolution products for estimating chlorophyll-a concentrations in oligo-to meso-trophic waters case study: Itumbiara Reservoir, Brazil. *Remote Sensing*, 6(2), pp.1634-1653 [doi:10.3390/rs6021634].

130. O'Reilly, C.M., Sharma, S., Gray, D.K., Hampton, S.E., Read, J.S., Rowley, R.J., Schneider, P., Lenters, J.D., McIntyre, P.B., Kraemer, B.M. and Weyhenmeyer, G.A., 2015. Rapid and highly variable warming of lake surface waters around the globe. *Geophysical Research Letters*, 42(24), pp.10-773 [doi:10.1002/2015GL066235].

131. Ostrovsky, I., Rimmer, A., Yacobi, Y.Z., Nishri, A., Sukenik, A., Hadas, O. and Zohary, T., 2013. Long-term changes in the Lake Kinneret ecosystem: the effects of climate change and anthropogenic factors. *Climatic change and global warming of inland waters: impacts and mitigation for ecosystems and societies*, pp.271-293.

132. Paerl, H.W., 2017. Controlling cyanobacterial harmful blooms in freshwater ecosystems. *Microbial biotechnology*, 10(5), pp.1106-1110 [doi:10.1111/1751-7915.12725].

133. Paerl, H.W. and Huisman, J., 2009. Climate change: a catalyst for global expansion of harmful cyanobacterial blooms. *Environmental microbiology reports*, 1(1), pp.27-37 [doi:10.1111/j.1758-2229.2008.00004.x].

134. Paerl, H.W. and Huisman, J., 2008. Blooms like it hot. *Science*, 320(5872), pp.57-58 [doi:10.1126/science.1155398].

135. Page, B.P., Olmanson, L.G. and Mishra, D.R., 2019. A harmonized image processing workflow using Sentinel-2/MSI and Landsat-8/OLI for mapping water clarity in optically variable lake systems. *Remote Sensing of Environment*, 231, p.111284 [doi:10.1016/j.rse.2019.111284].

136. Pahlevan, N., Chittimalli, S.K., Balasubramanian, S.V. and Vellucci, V., 2019. Sentinel-2/Landsat-8 product consistency and implications for monitoring aquatic systems. *Remote sensing of environment*, 220, pp.19-29 [doi:10.1016/j.rse.2018.10.027].

137. Palmer, S.C., Kutser, T. and Hunter, P.D., 2015. Remote sensing of inland waters: Challenges, progress and future directions. *Remote Sensing of Environment*, 157, pp. 1-8 [doi:10.1016/j.rse.2014.09.021].

138. Pareeth, S., Bresciani, M., Buzzi, F., Leoni, B., Lepori, F., Ludovisi, A., Morabito, G., Adrian, R., Neteler, M. and Salmaso, N., 2017. Warming trends of perialpine lakes from homogenised time series of historical satellite and in-situ data. *Science of the Total Environment*, 578, pp.417-426 [doi:10.1016/j.scitotenv.2016.10.199].

139. Peeters, F., Livingstone, D.M., Goudsmit, G.H., Kipfer, R. and Forster, R., 2002. Modeling 50 years of historical temperature profiles in a large central European lake. *Limnology and Oceanography*, 47(1), pp.186-197 [doi:10.4319/lo.2002.47.1.0186].

140. Philipson, P., Eriksso, K. and Stelzer, K., 2014, May. MERIS data for monitoring of small and medium sized humic Swedish lakes. In *2014 IEEE/OES Baltic International Symposium (BALTIC)* (pp. 1-4). IEEE.

141. Pinardi, M., Bresciani, M., Villa, P., Cazzaniga, I., Laini, A., Tóth, V., Fadel, A., Austoni, M., Lami, A. and Giardino, C., 2018. Spatial and temporal dynamics of primary producers in shallow lakes as seen from space: Intra-annual observations from Sentinel-2A. *Limnologica*, 72, pp.32-43 [doi:10.1016/j.limno.2018.08.002].

142. Pinardi, M., Fenocchi, A., Giardino, C., Sibilla, S., Bartoli, M. and Bresciani, M., 2015. Assessing potential algal blooms in a shallow fluvial lake by combining hydrodynamic modelling and remote-sensed images. *Water*, 7(5), pp.1921-1942 [doi:10.3390/w7051921].

143. Politi, E., Cutler, M.E. and Rowan, J.S., 2012. Using the NOAA Advanced Very High Resolution Radiometer to characterise temporal and spatial trends in water temperature of large European lakes. *Remote sensing of environment*, 126, pp.1-11 [doi:10.1016/j.rse.2012.08.004].

144. Potes, M., Costa, M.J., Da Silva, J.C.B., Silva, A.M. and Morais, M., 2011. Remote sensing of water quality parameters over Alqueva reservoir in the south of Portugal. *International Journal of Remote Sensing*, 32(12), pp.3373-3388 [doi:10.1080/01431161003747513].

145. Prats, J., Reynaud, N., Rebière, D., Peroux, T., Tormos, T. and Danis, P.A., 2018. LakeSST: Lake skin surface temperature in French inland water bodies for 1999-2016 from Landsat archives [doi:10.5194/essd-10-727-2018].

146. Pu, H., Liu, D., Qu, J.H. and Sun, D.W., 2017. Applications of imaging spectrometry in inland water quality monitoring—a review of recent developments. *Water, Air, & Soil Pollution*, 228(4), p.131 [doi:10.1007/s11270-017-3294-8].

147. Qin, Z., Karnieli, A. and Berliner, P., 2001. A mono-window algorithm for retrieving land surface temperature from Landsat TM data and its application to the Israel-Egypt border region. *International journal of remote sensing*, 22(18), pp.3719-3746 [doi:10.1080/01431160010006971].

148. Reinart, A. and Reinhold, M., 2008. Mapping surface temperature in large lakes with MODIS data. *Remote Sensing of Environment*, 112(2), pp.603-611 [doi:10.1016/j.rse.2007.05.015].

149. Reuter, D., Richardson, C., Pellerano, F., Irons, J., Allen, R., Anderson, M., Jhabvala, M., Lunsford, A., Montanaro, M., Smith, R. and Tesfaye, Z., 2015. The Thermal Infrared Sensor (TIRS) on Landsat 8: Design overview and pre-launch characterization. *Remote Sensing*, 7(1), pp.1135-1153 [doi:10.3390/rs70101135].

150. Reynolds, C.S., 2006. *The ecology of phytoplankton*. Cambridge University Press.

151. Rodríguez, Y.C., El Anjoumi, A., Gómez, J.D., Pérez, D.R. and Rico, E., 2014. Using Landsat image time series to study a small water body in Northern Spain. *Environmental monitoring and assessment*, 186(6), pp.3511-3522 [doi:10.1007/s10661-014-3634-8].

152. Romero, J.R., Antenucci, J.P. and Imberger, J., 2004. One-and three-dimensional biogeochemical simulations of two differing reservoirs. *Ecological Modelling*, 174(1-2), pp.143-160 [doi:10.1016/j.ecolmodel.2004.01.005].

153. Sandrini, G., Ji, X., Verspagen, J.M., Tann, R.P., Slot, P.C., Luimstra, V.M., Schuurmans, J.M., Matthijs, H.C. and Huisman, J., 2016. Rapid adaptation of harmful cyanobacteria to rising CO2. *Proceedings of the National Academy of Sciences*, 113(33), pp.9315-9320 [doi:10.1073/pnas.1602435113].

154. Schmidt, S.R., Gerten, D., Hintze, T., Lischeid, G., Livingstone, D.M. and Adrian, R., 2018. Temporal and spatial scales of water temperature variability as an indicator for mixing in a polymictic lake. *Inland Waters*, 8(1), pp.82-95 [doi:10.1080/20442041.2018.1429067].

155. Schneider, P. and Hook, S.J., 2010. Space observations of inland water bodies show rapid surface warming since 1985. *Geophysical Research Letters*, 37(22) [doi:10.1029/2010GL045059].

156. Schneider, K. and Mauser, W., 1996. Processing and accuracy of Landsat Thematic Mapper data for lake surface temperature measurement. *International Journal of Remote Sensing*, 17(11), pp.2027-2041 [doi:10.1080/01431169608948757].

157. Sharaf, N., Bresciani, M., Giardino, C., Faour, G., Slim, K. and Fadel, A., 2019a. Using Landsat and in situ data to map turbidity as a proxy of cyanobacteria in a hypereutrophic Mediterranean reservoir. *Ecological informatics*, 50, pp.197-206 [doi:10.1016/j.ecoinf.2019.02.001].

158. Sharaf, N., Fadel, A., Bresciani, M., Giardino, C., Lemaire, B.J., Slim, K., Faour, G. and Vinçon-Leite, B., 2019b. Lake surface temperature retrieval from Landsat-8 and retrospective analysis in Karaoun Reservoir, Lebanon. *Journal of applied remote sensing*, 13(4), p.044505 [doi:10.1117/1.JRS.13.044505].

159. Simon, R.N., Tormos, T. and Danis, P.A., 2014. Retrieving water surface temperature from archive LANDSAT thermal infrared data: Application of the mono-channel atmospheric correction algorithm over two freshwater reservoirs. *International Journal of Applied Earth Observation and Geoinformation*, 30, pp.247-250 [doi:10.1016/j.jag.2014.01.005].

160. Soares, L.M.V., Silva, T.F.D.G., Vinçon-Leite, B., Eleutério, J.C., Lima, L.C.D. and Nascimento, N.D.O., 2019. Modelling drought impacts on the hydrodynamics of a tropical water supply reservoir. *Inland Waters*, 9(4), pp.422-437 [doi:10.1080/20442041.2019.1596015] .

161. Sobrino, J.A., Jimenez-Munoz, J.C. and Paolini, L., 2004. Land surface temperature retrieval from LANDSAT TM 5. *Remote Sensing of environment*, 90(4), pp.434-440 [doi:10.1016/j.rse.2004.02.003].

162. Soulignac, F., Anneville, O., Bouffard, D., Chanudet, V., Dambrine, E., Guénand, Y., Harmel, T., Ibelings, B.W., Trevisan, D., Uittenbogaard, R. and Danis, P.A., 2019. Contribution of 3D coupled hydrodynamic-ecological modeling to assess the representativeness of a sampling protocol for lake water quality assessment. *Knowledge & Management of Aquatic Ecosystems*, (420), p.42 [doi:10.1051/kmae/2019034].

163. Soulignac, F., Danis, P.A., Bouffard, D., Chanudet, V., Dambrine, E., Guénand, Y., Harmel, T., Ibelings, B.W., Trevisan, D., Uittenbogaard, R. and Anneville, O., 2018. Using 3D modeling and remote sensing capabilities for a better understanding of spatio-temporal heterogeneities of phytoplankton abundance in large lakes. *Journal of Great Lakes Research*, 44(4), pp.756-764 [doi:10.1016/j.jglr.2018.05.008].

164. Soulignac, F., Vinçon-Leite, B., Lemaire, B.J., Martins, J.R.S., Bonhomme, C., Dubois, P., Mezemate, Y., Tchiguirinskaia, I., Schertzer, D. and Tassin, B., 2017. Performance assessment of a 3D hydrodynamic model using high temporal resolution measurements in a shallow urban lake. *Environmental Modeling & Assessment*, 22(4), pp.309-322 [doi:10.1007/s10666-017-9548-4].

165. Stainsby, E.A., Winter, J.G., Jarjanazi, H., Paterson, A.M., Evans, D.O. and Young, J.D., 2011. Changes in the thermal stability of Lake Simcoe from 1980 to 2008. *Journal of Great Lakes Research*, 37, pp.55-62 [doi:10.1016/j.jglr.2011.04.001].

166. Strong, A.E., 1974. Remote sensing of algal blooms by aircraft and satellite in Lake Erie and Utah Lake. *Remote sensing of Environment*, 3(2), pp.99-107 [doi:10.1016/0034-4257(74)90052-2].

167. Stumpf, R.P., Davis, T.W., Wynne, T.T., Graham, J.L., Loftin, K.A., Johengen, T.H., Gossiaux, D., Palladino, D. and Burtner, A., 2016. Challenges for mapping cyanotoxin patterns from remote sensing of cyanobacteria. *Harmful Algae*, 54, pp.160-173 [doi:10.1016/j.hal.2016.01.005].

168. Sun, J. and Liu, D., 2003. Geometric models for calculating cell biovolume and surface area for phytoplankton. *Journal of plankton research*, 25(11), pp.1331-1346 [doi:10.1093/plankt/fbg096].

169. Teggi, S., 2012. A technique for spatial sharpening of thermal imagery of coastal waters and of watercourses. *International journal of remote sensing*, 33(10), pp.3063-3089 [doi:10.1080/01431161.2011.627888].

170. Toffolon, M., Piccolroaz, S., Majone, B., Soja, A.M., Peeters, F., Schmid, M. and Wüest, A., 2014. Prediction of surface temperature in lakes with different morphology using air temperature. *Limnology and Oceanography*, 59(6), pp.2185-2202 [doi:10.4319/lo.2014.59.6.2185].

171. Toming, K., Kutser, T., Laas, A., Sepp, M., Paavel, B. and Nõges, T., 2016. First experiences in mapping lake water quality parameters with Sentinel-2 MSI imagery. *Remote Sensing*, 8(8), p.640 [doi:10.3390/rs8080640].

172. Tufford, D.L. and McKellar, H.N., 1999. Spatial and temporal hydrodynamic and water quality modeling analysis of a large reservoir on the South Carolina (USA) coastal plain. *Ecological modelling*, 114(2-3), pp.137-173 [doi:10.1016/S0304-3800(98)00122-7].

173. Vermote, E.F., Tanré, D., Deuze, J.L., Herman, M. and Morcette, J.J., 1997. Second simulation of the satellite signal in the solar spectrum, 6S: An overview. *IEEE transactions on geoscience and remote sensing*, 35(3), pp.675-686 [doi:10.1109/36.581987].

174. Vinçon-Leite, B. and Casenave, C., 2019. Modelling eutrophication in lake ecosystems: A review. *Science of the Total Environment*, 651, pp.2985-3001 [doi:10.1016/j.scitotenv.2018.09.320].

175. Vinçon-Leite, B., Lemaire, B.J., Khac, V.T. and Tassin, B., 2014. Long-term temperature evolution in a deep sub-alpine lake, Lake Bourget, France: how a one-dimensional model improves its trend assessment. *Hydrobiologia*, 731(1), pp.49-64 [doi:10.1007/s10750-014-1818-4].

176. Visser, P.M., Verspagen, J.M., Sandrini, G., Stal, L.J., Matthijs, H.C., Davis, T.W., Paerl, H.W. and Huisman, J., 2016. How rising CO2 and global warming may stimulate harmful cyanobacterial blooms. *Harmful Algae*, 54, pp.145-159 [doi:10.1016/j.hal.2015.12.006].

177. Wahl, B. and Peeters, F., 2014. Effect of climatic changes on stratification and deep-water renewal in Lake Constance assessed by sensitivity studies with a 3D hydrodynamic model. *Limnology and oceanography*, 59(3), pp.1035-1052 [doi:10.4319/lo.2014.59.3.1035].

178. Wang, F., Qin, Z., Song, C., Tu, L., Karnieli, A. and Zhao, S., 2015. An improved mono-window algorithm for land surface temperature retrieval from Landsat 8 thermal infrared sensor data. *Remote Sensing*, 7(4), pp.4268-4289 [doi:10.3390/rs70404268].

179. Wang, M., Shi, W. and Tang, J., 2011. Water property monitoring and assessment for China's inland Lake Taihu from MODIS-Aqua measurements. *Remote Sensing of Environment*, 115(3), pp.841-854 [doi:10.1016/j.rse.2010.11.012].

180. Wang, Q., Blackburn, G.A., Onojeghuo, A.O., Dash, J., Zhou, L., Zhang, Y. and Atkinson, P.M., 2017. Fusion of Landsat 8 OLI and Sentinel-2 MSI data. *IEEE Transactions on Geoscience and Remote Sensing*, 55(7), pp.3885-3899.

181. Wang, S., Qian, X., Han, B.P., Luo, L.C. and Hamilton, D.P., 2012. Effects of local climate and hydrological conditions on the thermal regime of a reservoir at Tropic of Cancer, in southern China. *Water research*, 46(8), pp.2591-2604 [doi:10.1016/j.watres.2012.02.014].

182. Watanabe, F., Alcantara, E., Rodrigues, T., Rotta, L., Bernardo, N. and Imai, N., 2018. Remote sensing of the chlorophyll-a based on OLI/Landsat-8 and MSI/Sentinel-2A (Barra Bonita reservoir, Brazil). *Anais da Academia Brasileira de Ciências*, 90(2), pp.1987-2000 [doi :10.1590/0001-3765201720170125].

183. Werdell, P.J., McKinna, L.I., Boss, E., Ackleson, S.G., Craig, S.E., Gregg, W.W., Lee, Z., Maritorena, S., Roesler, C.S., Rousseaux, C.S. and Stramski, D., 2018. An overview of approaches and challenges for retrieving marine inherent optical properties from ocean color remote sensing. *Progress in oceanography*, 160, pp.186-212 [doi:10.1016/j.pocean.2018.01.001].

184. Wernersson, A.S., Carere, M., Maggi, C., Tusil, P., Soldan, P., James, A., Sanchez, W., Dulio, V., Broeg, K., Reifferscheid, G. and Buchinger, S., 2015. The European technical report on aquatic effect-based monitoring tools under the water framework directive. *Environmental Sciences Europe*, 27(1), p.7 [doi:0.1186/s12302-015-0039-4].

185. Williamson, C.E., Saros, J.E., Vincent, W.F. and Smol, J.P., 2009. Lakes and reservoirs as sentinels, integrators, and regulators of climate change. *Limnology and Oceanography*, 54(6part2), pp.2273-2282 .

186. Wloczyk, C., Richter, R., Borg, E. and Neubert, W., 2006. Sea and lake surface temperature retrieval from Landsat thermal data in Northern Germany. *International Journal of Remote Sensing*, 27(12), pp.2489-2502 [doi:10.1080/01431160500300206].

187. Wynne, T. and Stumpf, R., 2015. Spatial and temporal patterns in the seasonal distribution of toxic cyanobacteria in western Lake Erie from 2002–2014. *Toxins*, 7(5), pp.1649-1663 [doi:10.3390/toxins7051649].

188. Wüest, A. and Lorke, A., 2003. Small-scale hydrodynamics in lakes. *Annual Review of fluid mechanics*, 35(1), pp.373-412 [doi:10.1146/annurev.fluid.35.101101.161220].

189. Wynne, T.T., Stumpf, R.P., Tomlinson, M.C., Schwab, D.J., Watabayashi, G.Y. and Christensen, J.D., 2011. Estimating cyanobacterial bloom transport by coupling remotely sensed imagery and a hydrodynamic model. *Ecological Applications*, 21(7), pp.2709-2721 [doi:10.1890/10-1454.1].

190. Xu, C., Zhang, J., Bi, X., Xu, Z., He, Y. and Gin, K.Y.H., 2017. Developing an integrated 3D-hydrodynamic and emerging contaminant model for assessing water quality in a Yangtze Estuary Reservoir. *Chemosphere*, 188, pp.218-230 [doi:10.1016/j.chemosphere.2017.08.121].

191. Yacobi, Y.Z., Moses, W.J., Kaganovsky, S., Sulimani, B., Leavitt, B.C. and Gitelson, A.A., 2011. NIR-red reflectance-based algorithms for chlorophyll-a estimation in mesotrophic inland and coastal waters: Lake Kinneret case study. *Water research*, 45(7), pp.2428-2436 [doi:10.1016/j.watres.2011.02.002].

192. Yang, K., Yu, Z., Luo, Y., Yang, Y., Zhao, L. and Zhou, X., 2018. Spatial and temporal variations in the relationship between lake water surface temperatures and water quality-A case study of Dianchi Lake. *Science of the total environment*, 624, pp.859-871 [doi:10.1016/j.scitotenv.2017.12.119].

193. Yang, Z., Reiter, M. and Munyei, N., 2017. Estimation of chlorophyll-a concentrations in diverse water bodies using ratio-based NIR/Red indices. *Remote Sensing Applications: Society and Environment*, 6, pp.52-58 [doi:10.1016/j.rsase.2017.04.004].

194. Yéprémian, C., Catherine, A., Bernard, C., Congestri, R., Elersek, T. and Pilkaityte, R., 2016. Chlorophyll a extraction and determination. *Handbook of Cyanobacterial Monitoring and Cyanotoxin Analysis*, pp.331-334 [doi:10.1002/9781119068761.ch34].

195. Yu, X., Guo, X. and Wu, Z., 2014. Land surface temperature retrieval from Landsat 8 TIRS—Comparison between radiative transfer equation-based method, split window algorithm and single channel method. *Remote Sensing*, 6(10), pp.9829-9852 [doi:10.3390/rs6109829].

196. Zhan, W., Chen, Y., Zhou, J., Wang, J., Liu, W., Voogt, J., Zhu, X., Quan, J. and Li, J., 2013. Disaggregation of remotely sensed land surface temperature: Literature survey, taxonomy, issues, and caveats. *Remote Sensing of Environment*, 131, pp.119-139 [doi:10.1016/j.rse.2012.12.014].

197. Zhang, Y., Lin, S., Liu, J., Qian, X. and Ge, Y., 2010. Time-series MODIS image-based retrieval and distribution analysis of total suspended matter concentrations in Lake Taihu (China). *International journal of environmental research and public health*, 7(9), pp.3545-3560 [doi:10.3390/ijerph7093545].

198. Zhou, Y., He, B., Xiao, F., Feng, Q., Kou, J. and Liu, H., 2019. Retrieving the Lake Trophic Level Index with Landsat-8 Image by Atmospheric Parameter and RBF: A Case Study of Lakes in Wuhan, China. *Remote Sensing*, 11(4), p.457 [doi:10.3390/rs11040457].

199. Zolfaghari, K. and Duguay, C., 2016. Estimation of water quality parameters in lake erie from meris using linear mixed effect models. *Remote Sensing*, 8(6), p.473 [doi:10.3390/rs8060473].

200. Zouabi-Aloui, B., Adelana, S.M. and Gueddari, M., 2015. Effects of selective withdrawal on hydrodynamics and water quality of a thermally stratified reservoir in the southern side of the Mediterranean Sea: a simulation approach. *Environmental monitoring and assessment*, 187(5), p.292 [doi:10.1007/s10661-015-4509-3].

Appendix A: Numerical coefficients of the general single channel algorithm

The atmospheric functions of TIRS Band 10 presented in (5) and included in the SC1 algorithm were calculated from a second-order polynomial fit with the following coefficients (Jiménez-Muñoz et al., 2014):

$$\begin{bmatrix} \Psi_1 \\ \Psi_2 \\ \Psi_3 \end{bmatrix} = \begin{bmatrix} 0.040 & 0.0292 & 1.02 \\ -0.383 & -1.50 & 0.20 \\ 0.00918 & 1.36 & -0.275 \end{bmatrix} \begin{bmatrix} w^2 \\ w \\ 1 \end{bmatrix} \qquad 37$$

The coefficients for the atmospheric functions of the thermal Band 6 of Landsat 4 and 5 are shown in Table 13 following the matrix notation expressed in (5).

Table 13: Coefficients of the atmospheric functions for Band 6 of Landsat 4 and Landsat 5 (Jiménez-Muñoz et al., 2009).

Platform	C_{ij}	$i = 1$	$i = 2$	$i = 3$
Landsat 4 Band 6	$j = 1$	0.0877	-0.0967	1.09
	$j = 2$	-0.703	-0.612	-0.122
	$j = 3$	-0.0252	1.51	-0.488
Landsat 5 Band 6	$j = 1$	0.106	-0.130	1.12
	$j = 2$	-0.814	-0.476	-0.291
	$j = 3$	-0.0442	1.62	-0.487

The numerical coefficients for the atmospheric functions of TIRS Band 10 shown in (7) are presented in Table 14.

Table 14: Numerical coefficients for the atmospheric functions of TIRS Band 10 listed in equation (7), (Cristóbal et al., 2018).

Coefficients	Ψ_1	Ψ_2	Ψ_3
a	4.47	-30.4	-3.76
b	-0.0000748	0.000911	-0.000141
c	0.0466	-0.573	0.0911
d	0.0232	-0.784	0.545
e	-0.0000496	0.00140	-0.000909
f	-0.0263	0.215	0.0418
g	-2.45	106	-80.0
h	0.0000492	-0.000376	-0.000104
i	-7.21	89.6	-14.7

Appendix B: *Chl-a* extraction and determination protocol

Concentrations of *Chl-a* were determined by spectrophotometry in 2018 according to (Yéprémian et al., 2016). In what follows is a description of the adopted protocols.

Sample preparation

a) Filter the water volume (defined according to the sample concentration) using a GF/C filter.

b) Place the filter in a 15 mL centrifuge tube. Cover the tube with aluminum foil to avoid photochemical degradation.

c) Freeze the sample at -20 °C to induce cell-lysis.

d) Add 10 mL of 100% ethanol and vortex the tubes.

e) Place the tubes in an ultrasonic bath with tap water and ice for 10 min.

f) Centrifuge the samples for 10 min at 4000 rpm.

Spectrophotometric readings

a) Blanck the spectrophotometer with the extraction solvent (ethanol or acetone).

b) Place the sample in a cuvette and record the absorbance at 632, 649, 665, 696 and 750 nm. In this case, absorbance values should be corrected by substracting the value recorded at 750 nm.

c) Pheophytin-a quantification

  i. For 1 mL of 100% ethanol extract, add 10 µl of 1 mol.l^{-1} HCL in the cuvette, agitate gently and wait for 2 min.
  ii. Neutralize with 10 µl of 1 mol.L^{-1} NaOH, agitate gently and wait for 2 min.
  iii. Record absorbance at 665 and 750 nm before acidification and after neutralization.

Calculations of *Chl-a* and pheophytin

a) For *Chl-a* analysis, use corrected absorbance values at 665 nm and apply the following equation to obtain concentrations:

$$chl - a \ (\mu g. l^{-1}) = \frac{11.90 \times Abs\ 665 \times Ve}{Vs \times I} \hspace{2cm} 38$$

where:
Ve: Volume of ethanol extract (mL).

b) To obtain pheophytin-corrected *Chl-a* concentrations apply the following equation:

$$chl - a_c \ (\mu g. l^{-1}) = \frac{28.44 \times (Abs\ 665b - Abs\ 665a) \times Ve}{Vs \times I} \hspace{1cm} 39$$

where:
$chl - a_c$: Pheophytin-corrected *Chl-a* concentration.

c) To obtain pheophytin concentrations, apply the following equation:

$$Pheophytin\ a \ (\mu g. l^{-1}) = \frac{20.47 \times Abs\ 665a \times Ve}{Vs \times I} \hspace{1.5cm} 40$$

Appendix C: Nitrate and phosphate analysis

Nitrate analysis by Palintest

a) Fill the Nitratest tube with sample to the 20 mL mark.

b) Add one level spoonful of Nitratset powder and one Nitratest tablet. Do not crush the tablets. add a cap to the tube. Shake the tube well for exactly one minute then allow contents to settle.

c) Filter a portion of the solution through a GF/B filter paper into a 10 mL test tube.

d) Add one Nitrocol tablet. Crush and mix to dissolve.

e) Stand for 10 minutes.

f) Operate the machine and take the test reading.

Orthophosphate analysis by colorimetric ascorbic acid

The samples used in this analysis were filtered through a 0.45 μm cellulose acetate filter. After the filtration, 0.3 mL of HCL are added to the sample which is then conserved at 4 °C.

a) Add 20 mL of the previously filtered sample in a glass tube.

b) Add 1 drop of phenolphthalein.

c) Add a drop of 5N H_2SO_4 if the sample turns red.

d) Add 5 mL of the combined reagent using a pipette. The combined reagent is prepared by mixing:
   a. H_2SO_4 (5N): 50 mL
   b. Potassium tartrate and antimony: 5 mL
   c. Ammonium molybdate: 15 mL
   d. Ascorbic acid: 30 mL

e) Close and shake vigorously.

f) Wait for reaction.

g) Read the absorbance or optical density (OD) at 880 nm between 10 and 30 minutes after the addition of the combined reagent.

Appendix D: Bathymetry construction

The water contours used for the construction of the bathymetry of Karaoun Reservoir were extracted from three Landsat images at the maximum water level and at 13.5 m and 17.44 m below the maximum water level (Figure 47). It was necessary to complete this information to describe the lowest part of the reservoir. A straight line was added, linking the river inlet on the lowest contour and the deepest point of the reservoir (60 m below the maximum level). The contours and this line were interpolated to form a full bathymetry.
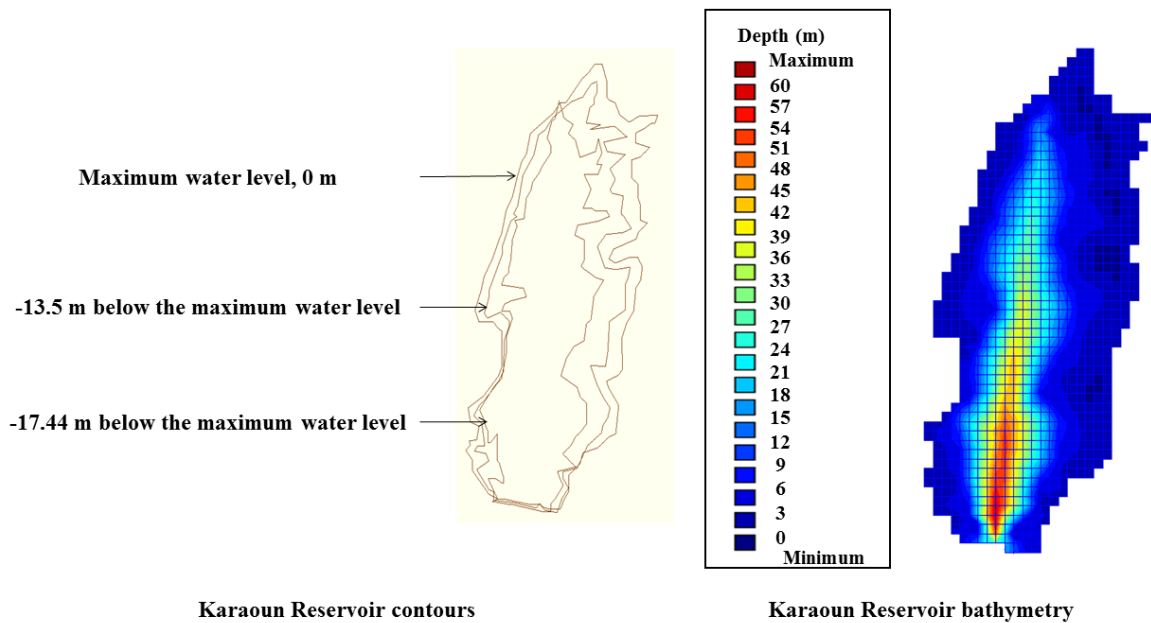

Karaoun Reservoir contours   Karaoun Reservoir bathymetry

Figure 47: Water contours and bathymetry of Karaoun Reservoir.

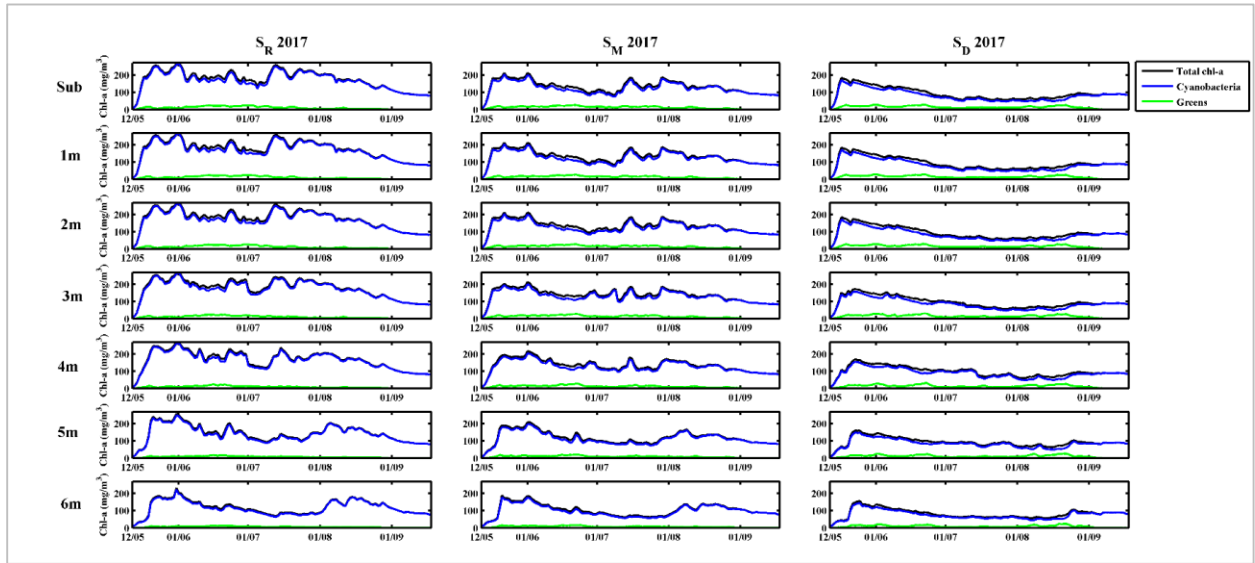# Appendix E: Ecological simulations
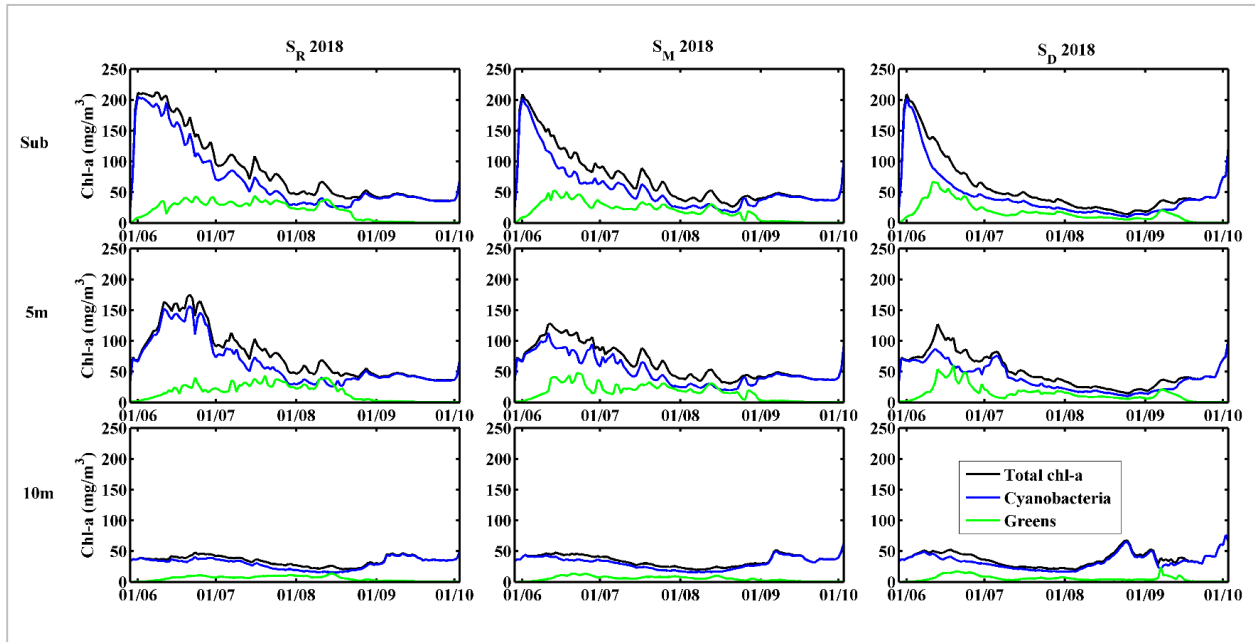

Figure 48: Simulated *Chl-a* concentrations in 2017.

Figure 49: Simulated *Chl-a* concentrations in 2018.